UNIVERSITÀ DI SIENA 1240

Dipartimento di Dipartimento di Biotecnologie, Chimica e Farmacia (DBCF).

Dottorato in Chemical and Pharmaceutical Sciences
38° Ciclo

Coordinatore/Coordinatrice: Prof.Maurizio TADDEI

Energy production and storage by electrocatalysis

Settore scientifico disciplinare: CHIM/02

Candidato/a

Carolina Castello

ICCOM-CNR

Firma digitale del/della candidato/a

Supervisore

Dott. Francesco Vizza

ICCOM-CNR

Firmato digitalmente da
CAROLINA CASTELLO
25/03/2026 20:25:54
con la Firma Digitale cheFIRMA!

Anno accademico di conseguimento del titolo di Dottore di ricerca

2025/2026

Università degli Studi di Siena

Dottorato in Chemical and Pharmaceutical Sciences

38° Ciclo

Data dell'esame finale

_____

Commissione giudicatrice

_____

_____

_____

_____

Supplenti

_____

_____

A chi non si arrende

Indice

1. Abstract

The development of efficient, cost-effective electrocatalysts is crucial for sustainable energy conversion, including hydrogen production and fuel cells. This doctoral research addresses the design, synthesis, characterization, and implementation of advanced non-noble, hybrid, and bimetallic electrocatalysts for key reactions such as hydrogen evolution (HER), hydrogen oxidation (HOR), oxygen reduction (ORR), and formate oxidation.

A self-supported MoO_{3-x}/$NiMoO_4$ powder was synthesized using NiO nanopowder as a structural template. Thermal annealing at 600°C generated sub-stoichiometric Mo oxides and enhanced surface roughness, improving active site accessibility and catalyst–membrane contact. The material exhibited high HER activity in three-electrode tests and stable operation in 5 cm² and 78.5 cm² AEM electrolyzers, demonstrating its scalability and potential for PGM-free hydrogen production.

Silver-supported metal phthalocyanines (M-Pc@Ag/C, M = Fe, Co, Ni, Cu) were developed for ORR in alkaline media. FePc@Ag/C showed the highest onset potential and current density, promoting a selective four-electron reduction to water. The combination of conductive Ag nanoparticles and active metal centers enhanced electron transfer, catalyst dispersion, and surface stability, offering a viable non-PGM alternative to platinum.

PdAu bimetallic nanoparticles were prepared via Metal Vapour Synthesis, yielding ultrasmall, ligand-free alloys with Pd-rich cores and Au-enriched surfaces. In direct formate fuel cells, PdAu/C showed higher power density, increased electrochemical surface area, and improved stability compared to Pd/C, highlighting the benefits of nanoscale alloy engineering.

Finally, Pd@Ni_4W/C catalysts for HER and HOR exhibited superior Pd mass activity (up to 463 A g^{-1}Pd) and reduced charge-transfer resistance, confirming enhanced kinetics and synergistic interactions.

Overall, this work demonstrates scalable strategies for synthesizing high-performance electrocatalysts, elucidates structure–activity–stability relationships, and provides a framework for translating lab-scale materials into device-level applications, advancing sustainable hydrogen production and energy conversion technologies.

2. Introduction

2.1 Energetic Transition

The crisis of climate change, caused by the effects of greenhouse gases, is a crucial issue that threatens the existence of life on our planet. The Earth's climate is changing rapidly, and the consequences are evident worldwide.[1] One of the main causes of climate change is the exploitation of fossil fuels as an energy source, which releases greenhouse gases such as carbon dioxide (CO_2), methane (CH_4), and nitrogen oxides (NO_x) into the atmosphere. These gases absorb heat from both the sun and the Earth, leading to an unbalance in the planet's radiative budget. This phenomenon, known as the greenhouse effect, results in a temperature increase.[2]

One of the most urgent effects of climate change is the melting of the polar ice caps, leading to rising sea levels that make coastal towns unsafe. In addition, extreme weather events such as wildfires reduce the planet's ability to cope with global warming, leading to food and water scarcity and the loss of biodiversity.[3]

Public opinion on the issue is divided. Some believe it is a natural fluctuation of the climate, while others argue that the anthropogenic contribution is

undeniable. The confirmation that the anthropogenic effect is central lies in the effects recorded is in the data: since the beginning of the Industrial Revolution in the late 18th century, temperatures have risen at an unprecedented rate—never recorded in such a short period in paleoclimatology.[4]

In recent decades, efforts have been made to mitigate the impacts of anthropogenic climate change through international agreements, such as the Paris Agreement, aimed at reducing greenhouse gas emissions and promoting sustainable development.[5] Renewable energy sources, energy efficiency measures, reforestation, and other climate mitigation strategies have been proposed as solutions of global warming.[6]

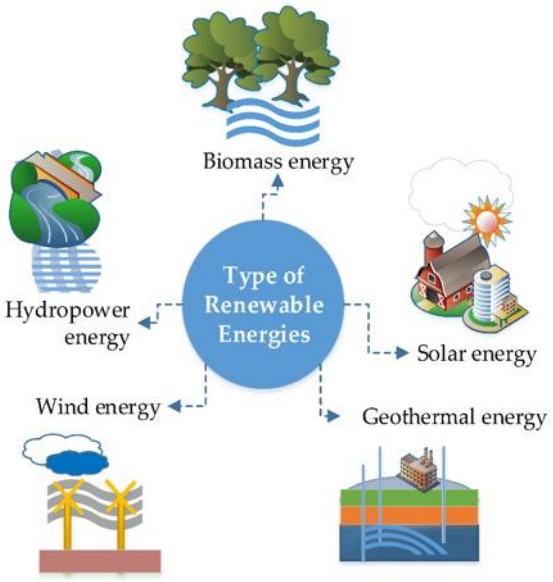

Figure 1: Renewable energies sources.

However, the conversion to a low carbon paradigm is too slow compared to the continue greenhauses emissions rising, making the challenge harder.[7]

One of the key solutions to the climate crisis is to transition to renewable energy sources that led to a circular energy system instead of the linear one our economy is based on.[8] Renewable energies are generated from naturally replenishing sources such as sunlight, wind, water, and biomass. These sources are clean and sufficient to cover a significant portion of the world's energy needs.[9] The production of renewable energy is a multi-step process that involves the natural resources and converts them into usable electricity[10]. While

renewable energies offer numerous benefits, there are also several challenges that need to be addressed for to spride them adoption and integration into the energy system[11]. Some of the main issues include:

Intermittency: one of the main challenges of renewable energies is their intermittent nature. Solar and wind energy are dependent on weather conditions, which makes them less reliable for meeting base load electricity demand.[11]

Storage and grid integration: energy storage technologies are essential for facing the intermittency of renewable. However, the cost and scalability of energy storage technologies remain a challenge. Even infrastructure needs to be adapted to the renewable energy engine.[12]

Land and resource use: the production of renewable energy sources such as solar panels and wind turbines requires significant land and resources, damaging the landscapes and biodiversity.[13]

Energy density and scalability: the low energy density of the renewable energy requests large land and infrastructure to generate the same fossil fuel amount of electricity. This is one of the main hurdle to spread worldwide this new vision.[14]

Cost and economics: the cost of renewable energies has been slashing in recent years, but it's not enough to be cost-competitive with fuels in some regions. Also, the government must commit funds to develop new technologies and infrastructure, especially given the disparity in resources and approaches between governments handling climate change.[14,15]

In this scenario, the energy vectors play a very important role in terms of intermittency, storage and scalability.[16]

They store chemical energy, that can be converted into electric energy in a different time and localization. The transition towards a sustainable energy system requires a profound transformation in energy production, distribution and utilization. In this context, energy vectors are a very promising strategy[17]. The main features an energy vector should respect are:

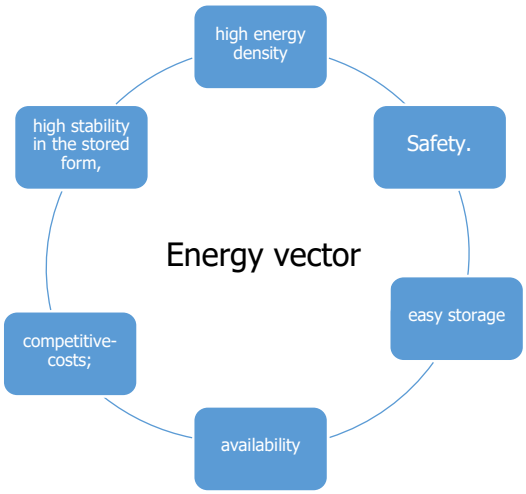

Figure 2: Energy vectore features

2.1.1. Hydrogen as energy vector

Hydrogen is one of the most interesting energy vectors and the most abundant element in the universe. Hydrogen (H_2) is colorless, odorless, and shows a very high energy density of around 120 MJ/kg—nearly three times that of gasoline (≈44 MJ/kg) or methane (≈55 MJ/kg). Because of these properties, it represents a promising alternative energy carrier for future sustainable systems[18].

Hydrogen production is classified into three main types based on the energy source and environmental impact: *grey, blue, and green*.[19] *Grey hydrogen* is produced by the oxidation of extracted methane through reforming, and it is currently the most exploited method industrially, even though it entails CO_2 emissions. *Blue hydrogen* is produced in the same way, but the CO_2 is captured, reducing its climate impact[19]. *Green hydrogen,* instead, is obtained by water electrolysis powered by renewable sources, making it the most sustainable process, although still too expensive and technologically complex for large-scale applications.[19]

Despite these challenges, the scientific community and policymakers are cooperating to achieve a "hydrogen economy" paradigm to support energy production for industrial processes and transport. However, its large-scale deployment faces significant technological, infrastructural, and safety issues, mainly related to storage and transport.[20]

Due to its high volatility and low volumetric density, hydrogen must be either compressed (at 350–700 bar) or liquefied at –253°C, both processes requiring high energy input and adapted infrastructure[21].To overcome these limitations, several storage methods have been investigated. The most common include physical storage, as compressed gas or cryogenic liquid[22], and solid-state storage[23], using materials such as metal hydrides[24], carbon-based materials, or metal–organic frameworks (MOFs)[25], which can reversibly absorb and release hydrogen[26]. In addition, chemical storage methods have been explored, such as Liquid Organic Hydrogen Carriers (LOHCs), including ammonia and organic compounds like formate[27]. These technologies could help address the main

challenges related to hydrogen storage, safety, and long-distance transport.[20]

2.1.2. Formate as energy vector

Formate is considered a promising energy carrier due to a unique combination of thermodynamic perspective, the oxidation of formate yields a reasonable energy density (approximately 1.4 kWh/kg)[26], and its electrochemical oxidation produces only CO_2 and water, making it suitable for clean energy systems[28]. Importantly, formate can be synthesized efficiently from CO_2,[29] through both electrochemical reduction and catalytic hydrogenation, enabling its use in carbon-neutral or even carbon-negative energy cycles. This makes formate not only a carrier but also a potential vector for CO_2 utilization and storage.[30]
Chemically, formate is non-volatile, non-flammable, and stable in aqueous solution, which contrasts with other liquid fuels such as methanol or ethanol that are more hazardous to store and transport [31]. Its high solubility in water facilitates its use in liquid-fed fuel cells[32], simplifying system design and minimizing phase management issues. Furthermore, formate exhibits low toxicity and corrosivity[33], which enhances the safety of fuel handling and reduces the degradation of system components over time[35].
From a systems engineering standpoint, formate allows energy to be stored in a dense, transportable, and rechargeable form, which can be regenerated using renewable electricity[36].This positions formate as an attractive candidate for chemical energy storage, grid balancing, and off-grid or portable fuel cell applications, especially when integrated with CO_2 capture and renewable energy sources.[36]

2.2 EROEI parameter

The Energy Returned on Energy Invested (EROEI) is a crucial parameter used to evaluate the net energy gain from an energy-producing process[37]. It quantifies the amount of effective energy obtained from a specific source relative to the energy required to extract, process, and deliver that energy[38].

Mathematically, it is expressed as:

$$EROEI = \frac{Energy\ obtained\ from\ the\ source}{Energy\ spent\ in\ the\ source\ production} \quad \text{Eq.1}$$

The greatest is the EROEI value the most convient is the process, where the cost are balanced by the produced energy[39]. This metric is crucial to compere different processes and technologies.

The EROEI values of the convetional, during 90th years, hydrocarbons combustion is around 100, due to easily accessible reserves and efficient extraction techniques. However, since these resources are less accessible, modern oil production typically yields EROEI values in the range of 10 to 15.[40]

The EROEI Renewable energy technologies depends on many factors such as technology evolution, location, and system design. Wind power systems reach EROEI values between 20 and 50[40]. Photovoltaic solar energy systems have been improved with EROEI values generally between 6 and 12, depending on the solar panel technologies.[41]

In contrast, some bioenergy sources, particularly first-generation biofuels, often exhibit much lower EROEI values—sometimes below 3—due to the significant energy required for cultivation, harvesting, processing, and transportation[42]. This low net energy return raises questions about their long-term sustainability and competitiveness compared to other energy carriers.[43]

Understanding and optimizing EROEI is essential for developing sustainable energy systems. A low EROEI lies that the produced energy needs to be reinvested to produce itself and a lower available amount for society[41]. Therefore, energy sources with higher EROEI are more interesting to design a new realistic energy economy.[40]

2.3 Fuel Cells

Fuel cells play an important role as technology in a new, more sustainable, world. These electrochemical devices are capable of directly converting the chemical energy of a fuel into electrical energy.[43]

The main advantage of these devices is that, unlike thermal machines which rely on the heat dissipated by combustion, their efficiency is not constrained by the thermodynamic limits imposed by the Carnot cycle.[44] By utilizing reversible processes, the chemical energy involved in the thermodynamic process is converted into electrical energy without the theoretical limits of thermodynamics, significantly enhancing the machine's efficiency. In fact, fuel cells can reach even efficiency of 50-60%, compared to the 20-30% of thermal machines.[44]

The main advantage of these devices is that, unlike conventional thermal engines, which rely on the conversion of chemical energy into heat and subsequently into mechanical work, their efficiency is not limited by the thermodynamic constraints of the Carnot cycle[46]. Instead, fuel cells directly convert the chemical energy of the reactants into electrical energy through electrochemical (reversible) reactions, thereby avoiding the intermediate heat generation step and significantly enhancing overall efficiency. As a result, fuel cells can achieve efficiencies of up to 50–60%, compared to only 20–30% typically obtained from combustion-based thermal machines.[43]

Their process is based on two electrodes — anode and cathode — separated by an electrolyte membrane that selectively transports ions.

At the anode, the fuel — hydrogen or short chain alcohols — are oxidized, releasing ions and electrons; the electrons travel through an external circuit to generate electrical current, while the ions cross the membrane to keep the electroneutrality of the system.

At the cathode, atmospheric oxygen is reduced by the electrons to form water as the only byproduct.

There are many different fuel cell technologies (Tab.1) that work in different conditions and materials, but in any case, the high efficiency is undeniable like

environment compatibility.

However, there are still practical limits, such as those related to the kinetics of chemical reactions and the internal resistances of materials.[44]

In order of this, the scientific community is focused on optimizing electrodes and membranes, improving durability and cost of catalysts.

Type	Electrolyte	Ion Transported	Operating Temp.	Fuel	Catalyst
PEMFC	Solid polymer (e.g., Nafion)	H^+ (protons)	60–80 °C	Pure H_2	Pt (anode and cathode)
AEMFC	Solid polymer (similar to PEMFC)	OH^-	60–80 °C	Pure H_2	Pt (cathode) and Pd/CeO_2 (anode)
DAFC	Solid polymer (similar to PEMFC)	H^+	50–120 °C	Methanol, Ethanol, glycerol	Pt-Ru (anode),Pt (cathode)
AFC	Aqueous KOH	OH^- (hydroxide)	60–90 °C	H_2	Ni (anode), Ag or Pt (cathode)
PAFC	Phosphoric acid	H^+	150–200 °C	H_2, reformate gas	Pt
MCFC	Molten carbonate salts (Li, K)	CO_3^{2-} (carbonate)	600–700 °C	H_2, CO, CH_4, biogas	Ni-based (anode), Li-ferrite (cathode)

Type	Electrolyte	Ion Transported	Operating Temp.	Fuel	Catalyst
SOFC (Solid Oxide FC)	Solid ceramic (e.g., YSZ)	O^{2-} (oxide ions)	650–1000 °C	H_2, CO, CH_4, hydrocarbons	Ni-based (anode), Perovskite (cathode)

Table 1: Fuel cells classification

2.3.1. H_2/O_2 Proton Exchange Membrane Fuel Cells

Proton Exchange Membrane Fuel Cells (PEMFCs) are among the most promising technologies for clean energy production from hydrogen and oxygen. The mechanism is as mentioned before for fuel cells, but the main characteristic is the membrane.

PEMFCs is equipped with polymer electrolyte membrane, which plays a fundamental role in:

- selectively conducting protons (H^+) from the anode to the cathode,
- to prevent the direct crossover of reactant gases (H_2 and O_2),
- physically separating the two half-cell reactions.[45]

The ideal membrane must have:

high proton conductivity (> 0.1 S/cm^2),

- low gas permeability,
- excellent chemical, thermal, and mechanical stability,
- good hydration retention.[46]

Currently, the benchmark material is Nafion® by DuPont, a perfluorinated copolymer with sulfonic acid groups (-SO_3H) that ensures excellent performance at low temperatures (60–90 °C) under humid conditions.[47] Nafion® represents the state of the art among commercial membranes for PEMFCs, thanks to its high proton conductivity and chemical durability[48]. However, its performance depends strongly on hydration: the membrane must remain "wet" to keep the proton conduction pathways active. For this reason,

the reactant gases are humidified before entering the cell. [49,50]

Two fundamental reactions occur within the fuel cell; At the anode the Hydrogen Oxidation Reaction HOR:

$$H_2 \rightarrow 2H^+ + 2e^- \qquad \text{Eq(2)}$$

At the cathode the Oxygen Reduction Reaction ORR:

$$½O_2 + 2H^+ + 2e^- \rightarrow H_2O \qquad \text{Eq(3)}$$

As shown in figure 2, at the ionic level the protons generated at the anode cross the membrane and reach the cathode; while at the electronic level, electrons cannot pass through the membrane and must instead travel through an external circuit, producing useful electric current.[51]

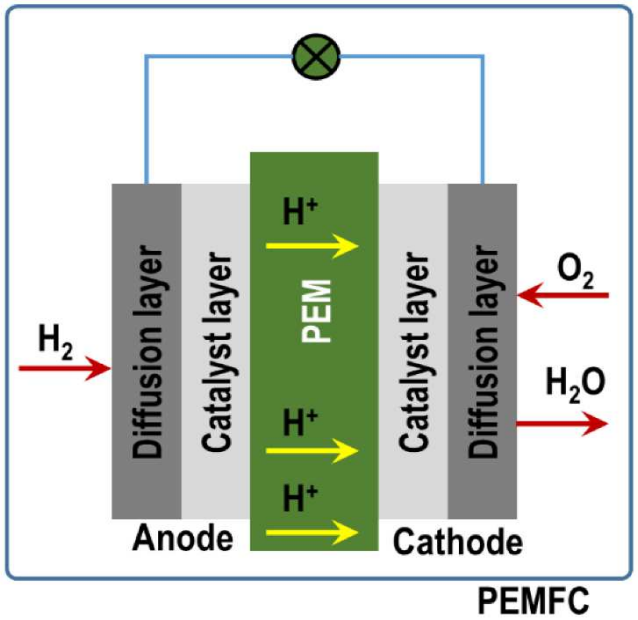

Figure 3: Proton Exchange Membrane Fuel Cells scheme

For the anodic and cathodic reactions to proceed at practical rates, efficient electrocatalysts are required. The best-known catalyst for both reactions is

nanostructured platinum (Pt), often supported on carbon. Its high surface area and exceptional electrocatalytic activity make platinum the key material for accelerating both the HOR and ORR.[52,53]

However, while HOR is a fast reaction, ORR is the rate-limiting step in PEMFCs. This is due to the complexity of the process, which involves multiple electrons, several reaction pathways (2- or 4-electron processes), and a high activation energy—even in the presence of platinum.[50]

The most desirable pathway in PEMFCs is the direct *4-electron* reduction of oxygen:

$$O_2 + 4H^+ + 4e^- \rightarrow 2H_2O \qquad \text{Eq(4)}$$

However, the ORR can also proceed via less efficient 2-electron pathways, forming hydrogen peroxide (H_2O_2):

$$O_2+2H^++2e^-\rightarrow H_2O_2 \qquad \text{Eq(5)}$$

$$H_2O_2 + 2H^+ + 2e^- \rightarrow 2H_2O \qquad \text{Eq(6)}$$

These intermediate species not only reduce the overall efficiency but can also degrade the membrane and catalyst layer, thereby demaging the structure of fuel cell. The ORR on electrodic surfaces proceeds via a series of adsorption and electron transfer steps: O_2 adsorption, O–O bond breaking (either before or after proton-electron transfers)[50], and subsequent protonation to form water. The adsorption of oxygen and the breaking of the O–O bond are particularly energy-intensive, contributing significantly to the high activation overpotential observed at the cathode.[50]

Despite platinum being the most active known catalyst for the ORR in acidic media, the reaction exhibits sluggish kinetics, with typical exchange current densities several orders of magnitude lower than those for HOR. Consequently, significant cathodic overpotentials are required to drive the reaction at practical current densities.[57]

Modern PEMFCs can achieve specific powers up to 1–2 kW per single cell in portable applications, and up to 100–200 kW in modular stacks used in vehicles

(e.g., Toyota Mirai, Hyundai Nexo).[58]

Advantages	**Disadvantages**
Zero emissions (only water vapor)	High cost of platinum catalyst and Nafion® membrane
High electrical efficiency (40–60%)	Sensitivity to fuel impurities (e.g., CO, SO_2)
Fast start-up and operation at low temperatures	Requires constant humidification of the membrane
Quiet operation (no noise or vibrations)	Limited long-term durability and stability
Modular and scalable design	Complex water and thermal management systems
Suitable for mobile, portable, and stationary use	Performance decreases under dry or cold conditions

Table 2: gain and loss of PEMFC

2.3.1.1 H_2/O_2 State of the art of PEMFC

The PEMFC are largely diffused (es.Toyota Miray since 2014) and the half-cost is caused by the necessary electrocatalysts to make the process faster.[53]

The best performance for ORR are reached by Platinum Group Metals (PGM), but they show stability problems related to agglomeration, dissolution and support corrosion.[53]For PGM electrocatalysts better activity and stability have been found for core-shell nanoparticles. The core is composed by nanoalloys of platinum and transition metals (Ni, Co etc.) modify the electronic structures by reducing the adsorption energy of intermediates.[59]

The noble-metal character of platinum endows the shell with the ability to enhance the stability and durability of the nanoalloys, preventing oxidation, dissolution, and structural degradation of the transition-metal core.[60]

The core-shell design improves the activity compared with pure platinum on carbon (Pt/C), for istance PtNi@Pt/C 1.0-1.3 W /cm^2 against the 0.7-0.9 W /cm^2 of Pt/C.[63]

However, PGM are not cost-competitive materials for that reason many efforts have been conducted to design PGM-free materials even with high performances and high stability.

The most interesting are the M-N-C with (M= Fe,Co,Zn etc...) electrocatalysts where single transition metal atoms are arranged into the nitrogen doped carbon like MN_4 sites.[54]

These materials produce 0.9-1.3 W /cm^2 at 0.9V, but the durability is just around against the 0.7-0.9 W /cm^2 of Pt/C.[65]

About the hydrogen oxidation reaction the electrocatalyst with the best performance in literature is palladium (Pd) on carbon doped with cerium oxide (CeO_2).[55]

Pd tends to grow on CeO_2 sites, creating an interphase very active for HOR, in fact the CeO_2 hydroxylation helps the ionic conductivity and the combination of hydrogen protons and hydroxide ions to produce water. Indeed, the reduction of Ce creates oxygen vacancies that make hydrogen adsorption more

favorable.[55]

2.3.2. Anion Exchange Membrane Fuel Cell

Anion Exchange Membrane Fuel Cells (AEMFCs) represent a promising and emerging alternative to PEMFCs in the field of hydrogen-based clean energy technologies. These fuel cells use an alkaline polymer electrolyte membrane that conducts hydroxide ions (OH^-) instead of protons, allowing for operation under basic conditions.56 This difference opens the door to the use of non-noble metal catalysts and offers potential cost advantages.[57]

The anion exchange membrane (AEM) serves to:

- transport hydroxide ions (OH^-) from the cathode to the anode,
- prevent the direct crossover of gaseous reactants,
- maintain the separation of the half-cell reactions.[58]

An ideal AEM should have:

high hydroxide ion conductivity (> 0.01 S/cm),

- good chemical and alkaline stability,
- mechanical robustness,
- low gas permeability,
- ability to retain water and maintain conductivity.[59]

AEMs are still under intensive research and development. While there is no definitive commercial standard like Nafion® in PEMFCs, significant progress has been made using membranes based on quaternary ammonium-functionalized polymers, such as poly(aryl piperidinium) or polybenzimidazoles with alkaline side groups.[60]

The key electrochemical reactions are reversed compared to PEMFCs due to the nature of the ionic carrier.

At the anode the Hydrogen Oxidation Reaction:

$$H_2 + 2OH^- \rightarrow 2H_2O + 2e^- \qquad \text{Eq(7)}$$

At the cathode the Oxygen Reduction Reaction:

$$½O_2 + H_2O + 2e^- \rightarrow 2OH^- \qquad \text{Eq(8)}$$

At the ionic level, hydroxide ions generated at the cathode migrate through the membrane toward the anode. At the electronic level, electrons flow through the external circuit from the anode to the cathode, producing electrical power.[61]

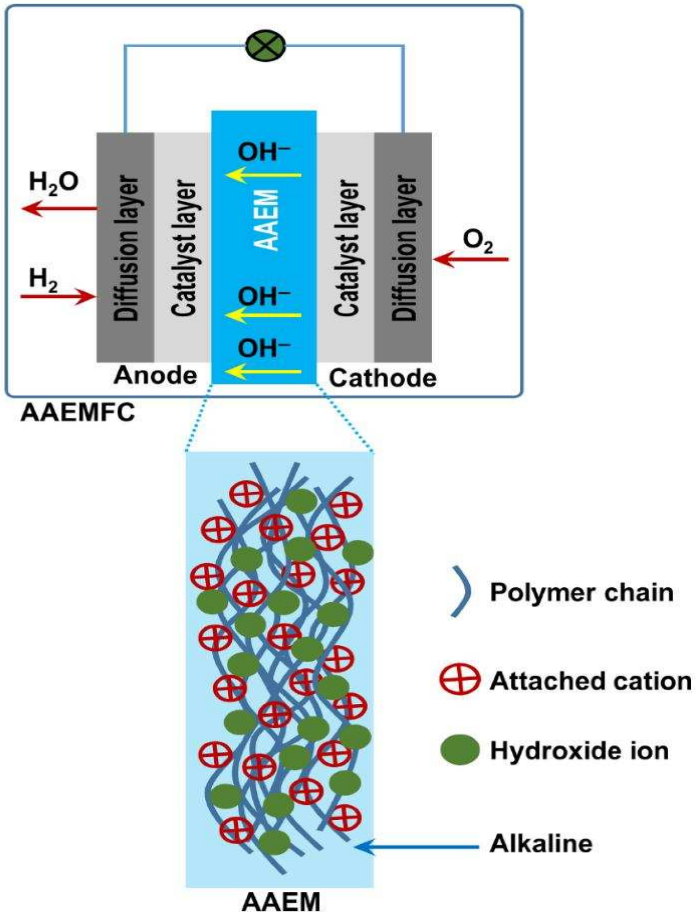

Figure 4: Anion Echange Membrane Electrolyzer scheme

One of the most attractive features of AEMFCs is the possibility to use non noble

metal catalysts, thanks to the alkaline environment. Catalysts such as Ni, Co, Fe, Mn, and Ag have shown promising activity for both HOR and ORR in alkaline media.[62] Nonetheless, Pt-based nanostructured catalysts still deliver the highest performance and are often used as benchmarks.[63]However, like PEMFCs, the ORR remains the rate-limiting step due to sluggish kinetics, even in alkaline conditions. Research continues into improving catalyst performance and developing stable, low-cost alternatives.[64]

Just like PEMFCs, AEMFC membranes require sufficient hydration to enable effective OH^- transport. Therefore, humidified gases are used, and careful water balance between electrodes

is necessary. However, water is produced at the anode side in AEMFCs (opposite to PEMFCs), which require different water management strategies and complicates the system design. [62]

Current AEMFCs have achieved peak power densities up to ~2.0 W/cm² under optimized laboratory conditions, comparable to the best PEMFCs. However, long-term durability and performance under real-world conditions remain challenges.[64]

2.3.2.1 Anion Exchange Membrane State of the Art

In recent years, research on catalysts for anion exchange membrane fuel cells (AEMFCs) has intensified, with the aim of reducing or eliminating the use of noble metals while maintaining high electrocatalytic performance and stability under alkaline conditions. Among the most promising materials for the oxygen reduction reaction (ORR) at the cathode are Fe–N–C catalysts[68], which, thanks to a hierarchically porous architecture, high graphitization d_2 with oxygen vacancies have shown significant improvements, reaching peak power outputs up to ~520 $mW \cdot cm^{-2}$ and excellent operational stability[66]. In particular, nickel–tungsten (Ni–W) alloys have attracted considerable attention for their remarkable electrocatalytic synergy: for instance, the NiW_4[67] alloy has demonstrated superior HOR activity compared to commercial Pt/C in alkaline electrolyte, attributed to the electronic modulation of Ni active sites by

tungsten, which optimizes the adsorption energies of H* and OH*, enhances the Volmer-Heyrovsky mechanism, and suppresses the formation of passivating surface species[68]. Furthermore agree, and nitrogen doping, have achieved power densities exceeding 2 $W \cdot cm^{-2}$ in H_2/O_2 configurations and over 1 $W \cdot cm^{-2}$ in H_2/air, with durability surpassing 150 hours.[69] On the anodic side, where the hydrogen oxidation reaction (HOR) is particularly sluggish in alkaline media, nickel-based catalysts supported on conductive or oxide-modified materials (e.g., Ni/graphene -N, Ni/CeO, the inclusion of tungsten increases the oxidative stability of nickel at high potentials[70], extending catalyst lifetime; ternary alloys such as $Ni_{5.2}WCu_{2.2}$ have further improved CO tolerance[71], maintaining stable activity for over 20 hours.[71] As for silver, it represents a viable low-cost alternative to platinum for the ORR due to its favorable electrocatalytic behavior in alkaline media and its relatively low cost. Ag/C catalysts with well-dispersed nanoparticles (5–9 nm) have achieved peak power densities of up to ~356 $mW \cdot cm^{-2}$ at 80 °C[72], while advanced strategies such as atomic layer deposition (ALD) on multi-walled carbon nanotube (MWCNT) supports have further enhanced specific activity and dispersion[74]. However, silver still suffers from limited long-term stability, mainly due to its tendency to oxidize and dissolve under realistic operating conditions, and its electrocatalytic activity remains lower than that of state-of-the-art Fe–N–C systems[75] and Ni–W alloys. In conclusion, while Fe–N–C catalysts remain the most efficient and stable for the ORR in AEMFCs and silver represents a feasible low-cost cathodic material, recent advances in Ni–W alloys highlight excellent prospects for the anode[68], combining high HOR activity, enhanced stability over pure Ni, and improved tolerance to contaminants, making them one of the most promising solutions for future high-performance, cost-effective AEMFC systems[77].

Advantages	Disadvantages
Use of non-precious metal catalysts (e.g., Ni, Fe, Co)	Lower membrane chemical stability in alkaline conditions
Lower overall system cost potential	Shorter lifetime and durability than PEMFCs
High efficiency and clean operation	Complex water management (water generated at the anode)
Reduced sensitivity to CO poisoning	Sensitive to CO_2 (carbonate formation in the membrane)
Compatibility with a variety of fuels (e.g., ammonia, alcohols)	Still at research and pre-commercial stage

Table 4: Gain and Loss of the AEMFC

2.4 Direct Formiate Fuel Cell

In recent years, Direct Formate Fuel Cells (DFFC) have attracted growing attention as an alternative technology for the direct conversion of chemical energy into electricity, using formate ($HCOO^-$) as a liquid energy carrier. In alkaline media, typically based on electrolytes such as KOH or NaOH, formate represents the active and stable redox form of the formic acid/formate couple. The anodic reaction under these conditions involves the oxidation of formate according to the following equation:

$$HCOO^- + 2OH^- \rightarrow CO_2 + H_2O + 2e \qquad \text{Eq(9)}$$

While the cathodic reaction involves the reduction of molecular oxygen to hydroxide ions:

$$O_2 + 2H_2O + 4e^- \rightarrow 4OH^- \qquad \text{Eq(10)}$$

This alkaline configuration offers several advantages, both from an electrocatalytic and operational standpoint. Firstly, the kinetics of the anodic oxidation of formate are significantly enhanced in basic conditions, due to the higher availability of OH^- ions, which facilitate deprotonation and reduce the overpotential required to initiate the reaction. Additionally, the alkaline environment enables the use of non-noble metal catalysts, such as nickel, copper, or cobalt, unlike acidic systems that require platinum- or palladium-based catalysts, which are more expensive and susceptible to CO poisoning.

Another key advantage lies in the safety and practicality of using formate compared to formic acid. In alkaline solution, formic acid is fully deprotonated and therefore chemically absent in its molecular form. This is beneficial not only for reactivity but also in terms of handling, storage, and transportation, as formate is non-volatile, less toxic, and less corrosive than formic acid, which poses challenges due to its pungency, volatility, and environmental and occupational hazards. Moreover, formate can be sustainable produced via the electrochemical reduction of CO_2, making it an ideal candidate for closed-loop

energy systems and low-carbon emission cycles.[29]

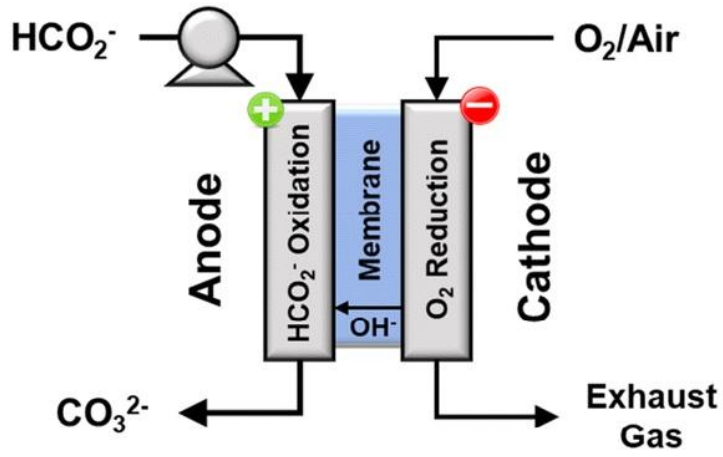

Figure 5: Direct formate fuel cell scheme

Finally, direct formate fuel cells exhibit greater operational stability over time compared to their methanol- or formic-acid-based counterparts, due to the reduced formation of reactive by-products, lower electrode fouling, and the chemically neutral behavior of the fuel in terms of vapor pressure and corrosivity. As a result, alkaline DFFC systems represent a highly promising platform for sustainable power generation in both portable and stationary applications, and for integration into energy architectures focused on the valorization of CO_2 as a resource rather than as waste. [30]

2.5 Electrolysis

An electrolyzer is an electrochemical device capable of breaking down water into its fundamental elements, hydrogen and oxygen, through a process called electrolysis. This happens by applying a direct electric current and forcing water molecules to split: hydrogen is produced at the cathode, while oxygen is generated at the anode. In an acidic environment, the reaction at the cathode is the reduction of hydrogen ions:

$$2H^+ + 2e^- \rightarrow H_2 \qquad \text{Eq(11)}$$

The water is oxidized in oxygen and the electrons:

$$2H_2O \rightarrow O_2 + 4H^+ + 4e^- \qquad \text{Eq(12)}$$

In alkaline environments, at the cathode, water gains electrons producing hydrogen and hydroxide:

$$2H_2O + 2e^- \rightarrow H_2 + 2OH^- \qquad \text{Eq(13)}$$

and at the anode, hydroxide ions are oxidized generating oxygen:

$$4OH^- \rightarrow O_2 + 2H_2O + 4e^- \qquad \text{Eq(14)}$$

The overall reaction in both cases is:

$$2H_2O \rightarrow 2H_2 + O_2 \qquad \text{Eq(15)}$$

One of the most important aspects of electrolyzers is their ability to produce high-purity hydrogen, which is useful in many industrial, energy, and sustainable mobility applications. The purity level of hydrogen can exceed 99.999%, especially when the system is well-designed and powered with deionized water. This technology is particularly appealing for decarbonization strategies because it enables the production of green hydrogen, obtained without CO_2 emissions, unlike traditional methods based on fossil fuels.[33]

To ensure that electrolysis reactions occur efficiently, the use of electrocatalysts is

essential. These materials accelerate the reactions at the anode and cathode. The most common catalysts for the hydrogen evolution reaction (HER) include platinum, which is extremely efficient but expensive. For the oxygen evolution reaction (OER), iridium or ruthenium oxides are often used, also very effective but rare and costly. To reduce cost, nickel-based catalysts, often alloyed with iron or molybdenum, are used especially in alkaline electrolyzers[34,35]. There are also alternative and more affordable materials, such as carbides, phosphides, or nitrides of transition metals, which are emerging as viable options. Additionally, carbon-based materials doped with heteroatoms like nitrogen, sulfur, or phosphorus offer promising catalytic performance thanks to modifications in their surface electronic structure[36].

2.5.1. Proton Exchange Membrane Electrolyzers

Proton Exchange Membrane (PEM) electrolyzers operate through electrochemical water splitting across a solid polymer electrolyte. Water is fed to the anode, where it undergoes oxidation in the Oxygen Evolution Reaction (OER):

$$H_2O \rightarrow ½\ O_2 + 2H^+ + 2e^- \qquad \text{Eq(16)}$$

Protons produced at the anode migrate through the polymer membrane to the cathode, where they are reduced to hydrogen via the Hydrogen Evolution Reaction (HER):

$$2H^+ + 2e^- \rightarrow H_2 \qquad \text{Eq(17)}$$

The total process is:

$$H_2O \rightarrow H_2 + ½\ O_2 \qquad \text{Eq(18)}$$

These devices typically operate at cell voltages between 1.8 and 2.2 V, achieving current densities of 1–3 A/cm², and produce hydrogen with >99.999% purity.

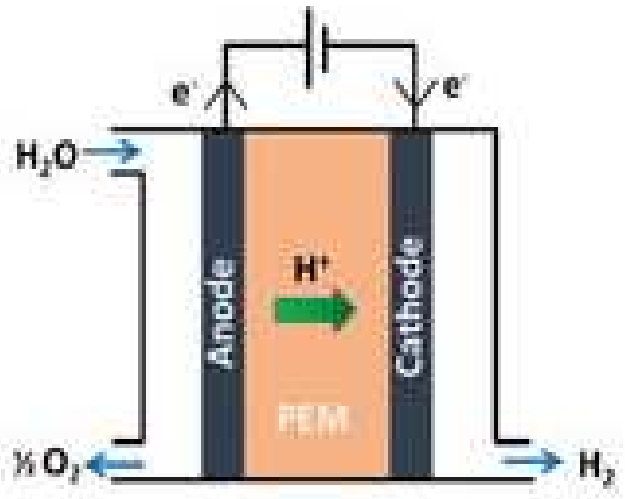

Figure 6: PEM electrolysis scheme

2.5.1.1 Proton Exchange Membrane Electrolyzers State of the Art

The efficiency and operational durability of PEM electrolyzers critically depend on the choice of electrocatalyst materials, particularly for the anodic and cathodic reactions in acidic environments. For the Oxygen Evolution Reaction (OER), the most widely used materials are based on iridium oxides (IrO_2), considered the industrial standard due to their combination of activity and stability under harsh operating conditions. Typically, Ir-based electrocatalysts exhibit an overpotential of approximately 300–350 mV at 10 mA/cm², with stability allowing prolonged operation up to 1000 hours at temperatures between 60 and 80 °C[40]. To reduce Ir content, strategies such as synthesizing mixed oxides like Ir-SnO_2 or Ir-Ta_2O_5 have been adopted, which maintain similar activity while reducing the noble metal load by up to 50%, still keeping an overpotential below 400 mV at 10 mA/cm².[41,42] The use of conductive supports such as antimony-doped tin oxide (ATO) has also been shown to improve dispersion and stability, reducing activity loss after extended cycling.[42] For the Hydrogen Evolution Reaction (HER), platinum (Pt) remains the most effective catalyst, with overpotentials below 30 mV at 10 mA/cm² under acidic conditions, and durability proven beyond 5000 hours of continuous operation. To reduce costs, Pt-M alloys (M = Ni, Co) allow for lower Pt loading while

maintaining overpotentials around 40–50 mV at 10 mA/cm², and core-shell nanostructures can achieve nearly complete atomic utilization.[43] Non-noble catalysts such as nickel and cobalt phosphides (Ni_2P, CoP) reach overpotentials in the range of 80–120 mV at 10 mA/cm², but their stability in acidic environments is limited to a few hundred hours, currently preventing their commercial use in PEM electrolyzers.[44]

In summary, while Pt- and Ir-based electrocatalysts still set the performance benchmark with reference to overpotential values and durability, research focuses on alternative materials and engineering strategies to reduce noble metal content without compromising electrochemical performance, which is essential for making PEM electrolyzers industrially competitive.

2.4.2 Anion Exchange Membrane Electrolyzers

Anion exchange membrane (AEM) electrolyzers represent a promising alternative to proton exchange membrane (PEM) systems due to their ability to operate in alkaline conditions, which enables the use of non-precious metal catalysts and less expensive cell components. AEM electrolyzers function by splitting water into hydrogen and oxygen using electrical energy, with hydroxide ions (OH^-) as the primary charge carriers. In this configuration, water is oxidized at the anode to produce oxygen, electrons, and OH^- ions, which are transported through the anion exchange membrane to the cathode. At the cathode, hydrogen is generated via the reduction of water and OH^- ions. This mechanism allows operation in less corrosive environments compared to acidic PEM systems, expanding the range of compatible catalyst materials.[45]

The current state of the art in electrocatalyst development for AEM electrolyzers focuses on improving both the activity and stability of catalysts for the hydrogen evolution reaction (HER) and oxygen evolution reaction (OER) in alkaline media. For the HER, transition metal-based materials such as Ni, Co, and Mo, often in the form of phosphides, sulfides, or nitrides, have shown significant promise due to their favorable hydrogen binding energies and low overpotentials.[46] For the OER, layered double hydroxides (LDHs), perovskites, and spinel oxides based on Ni, Fe, and Co have demonstrated high catalytic activity and durability.[47]

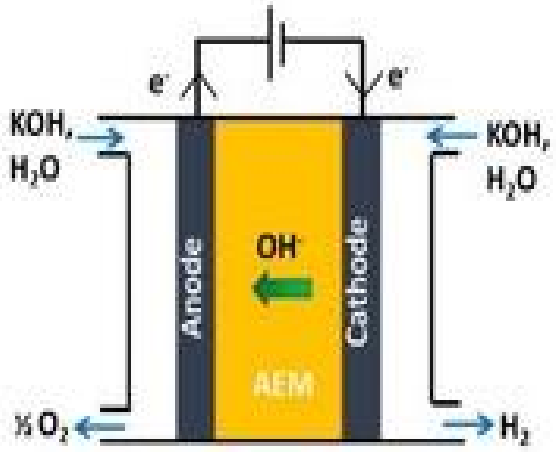

Figure 7: AEM electrolyzer scheme

2.5.1.2 Anion Exchange Membrane Electrolyzers State of the Art

Anion Exchange Membrane Electrolyzers (AEMELs) represent an emerging technology for sustainable hydrogen production, characterized by the use of anion exchange membranes that allow operation in alkaline environments. This feature enables the use of less expensive and more abundant catalytic materials compared to the noble metals typical of PEMELs. For the Oxygen Evolution Reaction (OER), electrocatalysts are mainly based on transition metal oxides such as Ni, Fe, Co and their mixtures, often in the form of amorphous hydroxides or oxyhydroxides (e.g., NiFe-LDH, CoFe-LDH), which exhibit high electrocatalytic activity in alkaline media. These materials typically achieve overpotentials of 250–350 mV at 10 mA/cm², with stability lasting several hundred hours under standard operating conditions[47,48]. The addition of iron to nickel (NiFe) is particularly effective in enhancing catalytic activity and conductivity, making these catalysts currently among the most promising for AEM applications.

For the Hydrogen Evolution Reaction (HER), the possibility to operate in alkaline media allows the use of catalysts free of platinum and other noble metals, such as nickel-molybdenum (NiMo) based alloys and compounds, known for their high activity and good stability. NiMo catalysts can achieve overpotentials in the range of 40–60 mV at 10 mA/cm², with durability exceeding 1000 hours under alkaline conditions[49]. Their nanoporous structure and the synergy between Ni and Mo promote water dissociation and the desorption of reactive

intermediates, significantly improving HER kinetics. Other studied materials include transition metal phosphides, carbides, and nitrides (e.g., Ni_2P, Mo_2C), but NiMo systems remain among the most effective for balancing performance and cost.

Overall, AEMELs benefit from a wider range of cost-effective and abundant catalytic materials compared to PEMELs, potentially leading to significant system cost reductions. However, major challenges remain, such as the long-term durability of membranes and catalysts in alkaline conditions, management of electrode-membrane interfaces, and scalability of nanostructured catalyst synthesis. Research continues to explore new materials and compositions aiming to further improve electrocatalytic efficiency and operational stability of AEM electrolyzers.[50]

2.6 Objectives of the thesis

The main aim of this PhD thesis was to design, synthesize, characterize, and evaluate advanced electrocatalytic materials for sustainable energy conversion, with a focus on hydrogen production, hydrogen oxidation, and oxygen reduction in alkaline media. The work sought to develop non-precious metal, hybrid, and bimetallic nanostructured catalysts—such as $MoO_{3-x}/NiMoO_4$ powders, metal phthalocyanine-silver composites, PdAu/C alloys, and NiW-based systems—investigating how their composition, structure, and morphology influence electrochemical activity, selectivity, and stability. A further objective was to demonstrate the practical feasibility of these materials by integrating them into membrane electrode assemblies and electrolyzer or fuel cell devices, bridging the gap between lab-scale catalyst development and device-level application. Overall, the thesis aimed to provide new insights into structure–activity relationships and to establish scalable strategies for designing cost-effective, high-performance, and durable electrocatalysts for alkaline energy technologies.

2.7 References

1. Redlin, Margarete, and Thomas Gries. "Anthropogenic climate change: the impact of the global carbon budget." *Theoretical and Applied Climatology* 146.1 (2021): 713-721.
2. Choulga, M., et al. "Global anthropogenic CO2 emissions and uncertainties as a prior for Earth system modelling and data assimilation, Earth Syst. Sci. Data, 13, 5311–5335." 2021.
3. Hansen, James, et al. "Ice melt, sea level rise and superstorms: evidence from paleoclimate data, climate modeling, and modern observations that 2 C global warming could be dangerous." *Atmospheric Chemistry and Physics* 16.6 (2016): 3761-3812.
4. Naakka, Tuomas, et al. "Polar winter climate change: strong local effects from sea ice loss, widespread consequences from warming seas." *EGUsphere* 2024 (2024): 1-29.
5. Kleidon, Axel, et al. "Global warming is due to an enhanced greenhouse effect, and anthropogenic heat emissions currently play a negligible role at the global scale." *Earth System Dynamics* 14.1 (2023): 241-242.
6. Wang, Fang, et al. "Climate change: Strategies for mitigation and adaptation." *The Innovation Geoscience* 1.1 (2023): 100015-1.
7. Slameršak, Aljoša, Giorgos Kallis, and Daniel W. O'Neill. "Energy requirements and carbon emissions for a low-carbon energy transition." *Nature communications* 13.1 (2022): 6932.
8. Slameršak, Aljoša, Giorgos Kallis, and Daniel W. O'Neill. "Energy requirements and carbon emissions for a low-carbon energy transition." *Nature communications* 13.1 (2022): 6932
9. Abdirahman, Abdinasir Ahmed, Muhammad Asif, and Osama Mohsen. "Circular economy in the renewable energy sector: A review of growth trends, gaps and future directions." *Energy Nexus* (2025): 100395.
10. Sinsel, Simon R., Rhea L. Riemke, and Volker H. Hoffmann. "Challenges and solution technologies for the integration of variable renewable energy

sources—a review." *renewable energy* 145 (2020): 2271-2285.

11. Erdiwansyah, fnm, et al. "A critical review of the integration of renewable energy sources with various technologies." *Protection and control of modern power systems* 6.1 (2021): 3.
12. Gowrisankaran, Gautam, Stanley S. Reynolds, and Mario Samano. "Intermittency and the value of renewable energy." *Journal of Political Economy* 124.4 (2016): 1187-1234.
13. Worku, Muhammed Y. "Recent advances in energy storage systems for renewable source grid integration: a comprehensive review." *Sustainability* 14.10 (2022): 5985.
14. Vera, Ivan, et al. "Land use for bioenergy: Synergies and trade-offs between sustainable development goals." *Renewable and Sustainable Energy Reviews* 161 (2022): 112409.
15. Uz, Dilek, and Callista Chim. "Intermittency in wind energy and emissions from the electricity sector: evidence from 13 years of data." *Sustainability* 14.4 (2022): 2242.
16. Orecchini, Fabio, and Vincenzo Naso. Energy systems in the era of energy vectors: a key to define, analyze and design energy systems beyond fossil fuels. Springer Science & Business Media, 2011.
17. Onen, Patrick Sunday, Geev Mokryani, and Rana HA Zubo. "Planning of multi-vector energy systems with high penetration of renewable energy source: a comprehensive review." *Energies* 15.15 (2022): 5717.
18. Møller, Kasper T., et al. "Hydrogen-A sustainable energy carrier." *Progress in natural science: Materials International* 27.1 (2017): 34-40.
19. Beyrami, Javid, et al. "Lifetime and performance of solid oxide electrolysis stacks and systems under different operation modes and conditions." *International Journal of Hydrogen Energy* 102 (2025): 980-995.
20. Krebsz, Melinda, et al. "Hydrogen storage, a key technology for the sustainable green economy: current trends and future challenges." *Sustainable Energy & Fuels* (2025).
21. Mekonnin, Abdisa Sisay, et al. "Hydrogen storage technology, and its

challenges: a review." *Catalysts* 15.3 (2025): 260.

22. Pal, Debarshi, et al. "The generation of biohydrogen from pretreated algal biomass in batch fermentation mode." *International Journal of Hydrogen Energy* 107 (2025): 321-331.
23. Liu, Zhihao, et al. "Carbon-embedded Ni catalysts for highly efficient CO2 methanation." *International Journal of Hydrogen Energy* 118 (2025): 170-178.
24. Jiang, Bo, et al. "Recent advances of carbon-based electromagnetic wave absorption materials facing the actual situations." *Carbon* 208 (2023): 390-409.
25. Murray, Leslie J., Mircea Dincă, and Jeffrey R. Long. "Hydrogen storage in metal–organic frameworks." *Chemical Society Reviews* 38.5 (2009): 1294-1314.
26. Modisha, Phillimon M., et al. "The prospect of hydrogen storage using liquid organic hydrogen carriers." *Energy & fuels* 33.4 (2019): 2778-2796.
27. Durbin, Deborah J., and Cecile Malardier-Jugroot. "Review of hydrogen storage techniques for on board vehicle applications." International journal of hydrogen energy 38.34 (2013): 14595-14617.
28. Eppinger, Jorg, and Kuo-Wei Huang. "Formic acid as a hydrogen energy carrier." ACS Energy Letters 2.1 (2017): 188-195.
29. Díaz-Sainz, Guillermo, Manuel Alvarez-Guerra, and Angel Irabien. "Continuous electrochemical reduction of CO2 to formate: comparative study of the influence of the electrode configuration with Sn and Bi-based electrocatalysts." Molecules 25.19 (2020): 4457.
30. Ono, Seo, Ryoichi Kanega, and Hajime Kawanami. "Hydrogen Storage and Release via Carbon Dioxide Hydrogenation to Formate Salts under High-Pressure Conditions with Ir Complex and Subsequent Formic Acid Dehydrogenation." *ChemistryOpen* 14.4 (2025): e202500032.
31. Ávila-Bolívar, Beatriz, et al. "Electrochemical reduction of CO2 to formate on easily prepared carbon-supported Bi nanoparticles." *Molecules* 24.11 (2019): 2032.
32. Ebrahimi, Parisa, Anand Kumar, and Majeda Khraisheh. "Thermodynamic

assessment of effect of ammonia, hydrazine and urea on water gas shift reaction." *International Journal of Hydrogen Energy* 47.5 (2022): 3237-3247.

33. Castello, Carolina, et al. "Direct formate anion exchange membrane fuel cells with a PdAu bimetallic nanoparticle anode electrocatalyst obtained by metal vapor synthesis." *Energy Advances* 3.10 (2024): 2520-2529.
34. Chen, Yimei, et al. "Dual-function electrolyte additive enabling simultaneous electrode interface and coordination environment regulation for zinc-ion batteries." *Energy Storage Materials* 58 (2023): 20-29.
35. Dual-function electrolyte additive enabling simultaneous electrode interface and coordination environment regulation for zinc-ion batteries
36. Fantazzini, Dean, Mikael Höök, and André Angelantoni. "Global oil risks in the early 21st century." *Energy Policy* 39.12 (2011): 7865-7873.
37. Hall, Charles AS, Stephen Balogh, and David JR Murphy. "What is the minimum EROI that a sustainable society must have?." *Energies* 2.1 (2009): 25-47.
38. Cleveland, Cutler J., et al. "Energy and the US economy: a biophysical perspective." *Science* 225.4665 (1984): 890-897.
39. Guilford, Megan C., et al. "A new long term assessment of energy return on investment (EROI) for US oil and gas discovery and production." *Sustainability* 3.10 (2011): 1866-1887.
40. Friedman, Peter D. "Evaluating economic uncertainty of municipal wind turbine projects." *Renewable Energy* 35.2 (2010): 484-489.
41. Hall, Charles AS, Jessica G. Lambert, and Stephen B. Balogh. "EROI of different fuels and the implications for society." *Energy policy* 64 (2014): 141-152.
42. Bao, Chao, and Chuang-lin Fang. "Geographical and environmental perspectives for the sustainable development of renewable energy in urbanizing China." *Renewable and Sustainable Energy Reviews* 27 (2013): 464-474.
43. Niakolas, Dimitris K., et al. "Fuel cells are a commercially viable alternative for the production of "clean" energy." *Ambio* 45.Suppl 1 (2016): 32-37.

44. Lutz, Andrew E., Richard S. Larson, and Jay O. Keller. "Thermodynamic comparison of fuel cells to the Carnot cycle." *International Journal of Hydrogen Energy* 27.10 (2002): 1103-1111.
45. Arif, Muhammad, et al. "Fuel Cell Comparison to Conventional Power Generation Technologies." *Hydrogen Utilization in Fuel Cells* (2024): 82-112.
46. Peighambardoust, S. Jamai, Soosan Rowshanzamir, and Mehdi Amjadi. "Review of the proton exchange membranes for fuel cell applications." *International journal of hydrogen energy* 35.17 (2010): 9349-9384.
47. Parekh, Abhi. "Recent developments of proton exchange membranes for PEMFC: A review." *Frontiers in Energy Research* 10 (2022): 956132.
48. Tellez-Cruz, Miriam M., et al. "Proton exchange membrane fuel cells (PEMFCs): Advances and challenges." *Polymers* 13.18 (2021): 3064.
49. Sun, Xinwei, et al. "Composite membranes for high temperature PEM fuel cells and electrolysers: a critical review." *Membranes* 9.7 (2019): 83.
50. Li, Hongda, et al. "Pt-based oxygen reduction reaction catalysts in proton exchange membrane fuel cells: controllable preparation and structural design of catalytic layer." *Nanomaterials* 12.23 (2022): 4173.
51. Orilade, Mejehiemi, and Jude Iroh. "A Review of Polymer Electrolyte Membrane Fuel Cells (PEMFCs)." (2025).
52. Mo, Shanyun, et al. "Recent advances on PEM fuel cells: from key materials to membrane electrode assembly." *Electrochemical Energy Reviews* 6.1 (2023): 28.
53. Walker, James S., Neil V. Rees, and Paula M. Mendes. "Progress towards the ideal core@ shell nanoparticle for fuel cell electrocatalysis." *Journal of Experimental Nanoscience* 13.1 (2018): 258-271.
54. Antolini, Ermete. "The oxygen reduction on Pt-Ni and Pt-Ni-M catalysts for low-temperature acidic fuel cells: A review." *International Journal of Energy Research* 42.12 (2018): 3747-3769.
55. Vezzù, Keti, et al. "Fe-carbon nitride "Core-shell" electrocatalysts for the oxygen reduction reaction." *Electrochimica Acta* 222 (2016): 1778-1791.

56. Miller, Hamish A., et al. "Recent developments in Pd-CeO2 nano-composite electrocatalysts for anodic reactions in anion exchange membrane fuel cells." *Electrochemistry Communications* 135 (2022): 107219.
57. Maurya, Sandip, et al. "A review on recent developments of anion exchange membranes for fuel cells and redox flow batteries." *Rsc Advances* 5.47 (2015): 37206-37230.
58. Maurya, Sandip, et al. "A review on recent developments of anion exchange membranes for fuel cells and redox flow batteries." *Rsc Advances* 5.47 (2015): 37206-37230.
59. Su, Fa-Cheng, Hsuan-Hung Yu, and Hsiharng Yang. "Anion-Exchange Membranes' Characteristics and Catalysts for Alkaline Anion-Exchange Membrane Fuel Cells." *Membranes* 14.12 (2024): 246.
60. Hagesteijn, Kimberly FL, Shanxue Jiang, and Bradley P. Ladewig. "A review of the synthesis and characterization of anion exchange membranes." *Journal of materials science* 53.16 (2018): 11131-11150.
61. Das, Gautam, et al. "Anion exchange membranes for fuel cell application: a review." *Polymers* 14.6 (2022): 1197.
62. Maurya, Sandip, et al. "A review on recent developments of anion exchange membranes for fuel cells and redox flow batteries." *Rsc Advances* 5.47 (2015): 37206-37230.
63. Su, Fa-Cheng, Hsuan-Hung Yu, and Hsiharng Yang. "Anion-Exchange Membranes' Characteristics and Catalysts for Alkaline Anion-Exchange Membrane Fuel Cells." *Membranes* 14.12 (2024): 246.
64. Das, Gautam, et al. "Anion exchange membranes for fuel cell application: a review." *Polymers* 14.6 (2022): 1197.
65. Adabi, Horie, et al. "High-performing commercial Fe–N–C cathode electrocatalyst for anion-exchange membrane fuel cells." *Nature energy* 6.8 (2021): 834-843.
66. Liu, Guimei, et al. "Inert Copper Incorporation Enables the High Activity and Durability of NiW Electrocatalyst for Alkaline Hydrogen Oxidation Reaction." *Advanced Energy Materials* 15.20 (2025): 2405127.
67. Hyun, Jonghyun, and Hee-Tak Kim. "Powering the hydrogen future: current

status and challenges of anion exchange membrane fuel cells." *Energy & Environmental Science* 16.12 (2023): 5633-5662.

68. Tian, Xiaoyu, et al. "Metal-support interaction boosts the stability of Ni-based electrocatalysts for alkaline hydrogen oxidation." *Nature communications* 15.1 (2024): 76.
69. Qin, Shuai, et al. "Ternary nickel–tungsten–copper alloy rivals platinum for catalyzing alkaline hydrogen oxidation." *Nature Communications* 12.1 (2021): 2686.
70. Xin, Le, et al. "Carbon supported Ag nanoparticles as high performance cathode catalyst for H2/O2 anion exchange membrane fuel cell." *Frontiers in chemistry* 1 (2013): 16.
71. Truong, Van Men, Ngoc Bich Duong, and Hsiharng Yang. "Comparison of carbon supports in anion exchange membrane fuel cells." *Materials* 13.23 (2020): 5370.
72. Hyun, Jonghyun, and Hee-Tak Kim. "Powering the hydrogen future: current status and challenges of anion exchange membrane fuel cells." *Energy & Environmental Science* 16.12 (2023): 5633-5662.

3. Silver nanoparticles combined with metal-phtalocyanines for Anion Exchange Membrane Fuel Cells

3.1 Introduction

As previously discussed, fuel cells, together with batteries, are key technologies for the clean energy transition.[1] However, the electrochemical processes occurring at the anode and cathode are associated with high activation energy barriers that hinder their kinetics.[2] To overcome these limitations and enhance reaction rates, electrocatalysts are required.

The anodic process, the hydrogen oxidation reaction (HOR), is a relatively fast half-reaction and hydrogen is readily oxidized. In contrast, the cathodic process, the oxygen reduction reaction (ORR), is the rate-determining step, owing to the challenge of preserving spin multiplicity during the conversion of oxygen to water.[3]

State-of-the-art catalysts for both HOR and ORR are nanostructured platinum-based electrocatalysts (Pt and PtRu nanoparticles dispersed on carbon), which exhibit outstanding performance in both alkaline (AEMFCs) and acidic environments (PEMFCs)[4]. The superior catalytic activity of platinum arises from its favourable electronic structure, which facilitates efficient electron transfer and optimal interaction with reaction intermediates.[5]

Platinum, and more in general PGMs, are expensive materials and have a poor availability, so it is necessary to find more convenient and diffused metals for fabricating environmentally and economically sustainable anodic and cathodic catalysts for fuel cells.[6] This purpose is easier working in alkaline media with AEMFCs [7]: looking to the Pourbaix's diagrams, a wider plethora of transition metals have stable and not soluble phases at alkaline pHs and anodic or cathodic potentials than acidic one, where only PGMs respect these criteria.[8]

Moreover, in alkaline environment the catalysts and the cell components are less subjected to corrosion phenomena during the operational lifetime of the device.[9]

Silver nanoparticles are promising candidates for fabricating cathodic electrocatalyst for promoting the oxygen reduction reaction (ORR) in alkaline media, primarily due to their ability to adsorb and activate molecular oxygen (O_2)[10]. However, the interaction between oxygen and the silver nanoparticles surface is not fully optimized: the O_2 binding energy is sufficient enough to promote the initial step of the reaction but it is too much weak for facilitating the following intermediate steps.[11] Moreover, silver is prone to surface oxidation and poisoning by contaminants during catalysts, phenomena which progressively reduces its catalytic activity.[12]

Another deeply studied class of cathodes for ORR in alkaline environment is based on metal phthalocyanines; these molecules are macrocyclic compounds containing a central metal ion (e.g. Fe, Co, or Ni) coordinated to the nitrogen atoms of a highly conjugated aromatic ligand. Metal phthalocyanines are very active catalysts for oxygen reduction reaction.[12] The metal centres acts as catalyst active sites enhancing the electron transfer processes and stabilizing the reaction intermediates, such as peroxide (O_2^{2-}) and superoxide (O_2^-).[13] However, metal phthalocyanines are prone to aggregation, which decreases active site availability, lowering the catalyst stability and active surface area, directly related to its electrochemical ORR performances.[14]

It is reported in literature that the combination of nanostructured silver catalysts with metal phthalocyanines represents a promising strategy for overcoming the limitation of both silver nanostructured and phthalocyanine based catalysts in the fabrication of cathodes for ORR.[13,14]

The synergistic effect arises from the capacity of phthalocyanines to adsorb and activate molecular oxygen via their central metal ions (e.g., Co^{2+} or Fe^{2+}), facilitating the formation of key reaction intermediates (OOH*, O*, OH*) and stabilizing them through charge delocalization across the conjugated macrocyclic structure.[15] Additionally, the organic conjugated framework provides a protective layer that mitigates surface passivation of the underlying

silver.[16]

Silver nanoparticles serve as anchoring sites for the metal phthalocyanines, promoting their uniform dispersion, minimizing aggregation (thus enhancing stability), and improving charge transfer owing to their superior electrical conductivity compared to isolated organic films.[17]

This chapter reports a preliminary investigation for the development of a sustainable nanostructured silver-based cathode (Ag/C) combined with three of the most active phthalocyanine (Fe, Co, and Ni) for promoting ORR in alkaline environment.[18] First the silver nanoparticles supported on Vulcan (Ag/C, 20% Ag) were synthetized using cysteamine as capping agent.[19] Later the Ag nanoparticles were capped with Fe, Co, Ni phthalocyanine, yielding the desired M-Pc@Ag/C catalysts (3 % M-Pc and 20% Ag).

The catalysts was morphologically characterized by X-ray diffraction and electron microscopy measurements coupled with EDX mapping; later the electrochemical activity towards ORR in alkaline media was investigated by half-cell measurements, such as RRDE experiments.

3.2 Synthesis of M-Pc (M=Fe, Co, Ni, Cu) @Ag/C

The catalysts were synthesized via a two-step procedure:

- Synthesis of silver nanoparticles immobilized on Vulcan carbon (Ag/C).
- Adsorption of metal phthalocyanine (M-Pc) onto Ag/C nanoparticles.

Silver nanoparticles were prepared by dissolving 40 mg of silver nitrate ($AgNO_3$) in 40 mL of ethylene glycol (EG) and heating the solution to 50 °C under stirring for 20 minutes. In parallel, a dispersion containing 40 mg of Vulcan XC-72 carbon support and 2 mg of cysteamine in 20 mL of ethylene glycol (EG) was prepared by sonication for 1 hour. The two solutions were then combined at 50 °C and heated to 160 °C at a rate of 3 °C min^{-1}, maintaining this temperature for 3 hours to promote the nucleation and growth of silver nanoparticles.

This step is critical because silver nanoparticles tend to aggregate due to their high surface energy, which can lead to a broad particle size distribution and a

reduction in the available catalytic surface area[20]. Cysteamine plays a crucial role in mitigating this issue: its thiol groups strongly coordinate to silver nuclei, preventing aggregation, while its amino groups interact with the carbon support, ensuring homogeneous anchoring of the nanoparticles[19]. In the absence of cysteamine, nucleation predominantly occurs in solution rather than on the carbon surface, resulting in uncontrolled particle growth and poor dispersion.[21]

After the reaction, the mixture was cooled to room temperature, washed with ethanol, filtered, and dried to obtain the Ag/C catalyst. (yield 96%, 18% wt. Ag by ICP-OES) Compared to other grafting and capping agents reported in the literature,[21] cysteamine demonstrates superior yield performance: the silver loading calculated by ICP-OES of 18 wt.% closely approaches the theoretical value of 20 wt.%, indicating a high success silver nanoparticles immobilization onto the carbon support. In the second step, M-Pc molecules (Fe-Pc, Co-Pc or Ni-Pc) were adsorbed onto the Ag/C nanoparticles mixing the dried catalyst (50 mg of Ag/C) and the M-Pcs (1.5 mg of Fe-Pc, 1.5 mg of Co-Pc or 1.5 mg of Ni-Pc) in 50 ml of dimethylformamide (DMF) by overnight stirring. The resulting suspension was filtered and washed with ethanol to remove unabsorbed species, yielding the M-Pc@Ag/C composite catalyst (92% yield, 2.8 Wt.% of Fe, 2.8 wt.% of Co and 2.6% wt of Ni).

3.3 Physical characterization

X-ray diffraction (XRD) analysis was performed to characterize the Ag/C nanoparticles. The diffraction pattern of silver nanoparticles supported on carbon Vulcan (figure 8) confirmed the presence of the characteristic face-centered cubic (FCC) crystalline structure of metallic silver. The diffractogram exhibits the typical FCC Ag diffraction peaks at approximately 2θ = 38.1°, 44.3°, 64.4°, 77.4°, and 79.5°, corresponding to the (111), (200), (220), (311)[23], and (222) crystal planes, respectively, in agreement with JCPDS card no. 04-0783[18]. The absence of reflections at 32.7°, 38.1°, 55°, 65° of Ag2O and 32.7°, 38.1°, 55°, 65° of AgO indicates a high purity of the silver phase and suggests a

uniform dispersion of the nanoparticles on the carbon support.[24,25] Additionally, the sharpening peaks shape reflects high crystalline metallic silver structures[25].

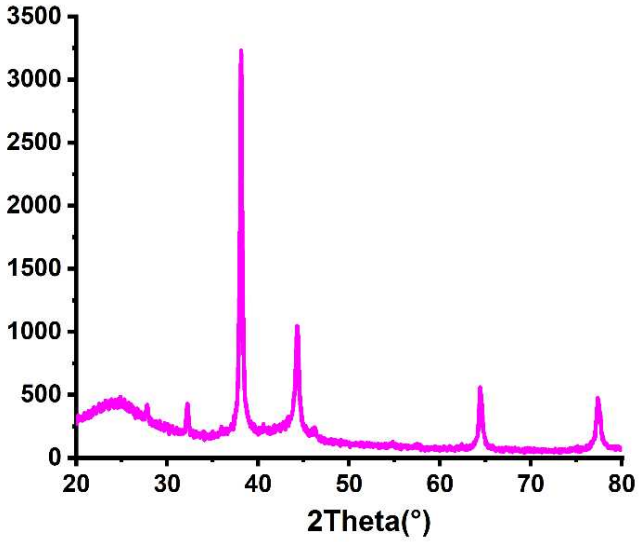

Figure 8: X ray diffraction of silver nanoparticles on carbon

High-resolution transmission electron microscopy (HRTEM) reported in figure 18 revealed silver nanoparticles with a heterogeneous size distribution. The observed interplanar spacing of approximately 0.235 nm corresponds to the (111) planes of FCC metallic silver, confirming their crystalline nature[25]. The nanoparticles appear uniformly dispersed and predominantly located on the external surface of the carbon support (Fig. 9), indicating an efficient and homogeneous surface distribution. Anyway, some nanoparticles of c.a. 150 nm diameter were found in the samples (figure 10a, 10e, 10i). The nanoparticles have a mean size of 15 nm (the aggregates were excluded from the diameter calculations). Furthermore, HRTEM images reveal a higher nanoparticle density on the carbon surface in the presence of cysteamine respect similar catalysts reported in literature synthetized using other capping agents,[25,26] further corroborating cysteamine effectiveness in enhancing the metal deposition process onto Vulcan XC-72.

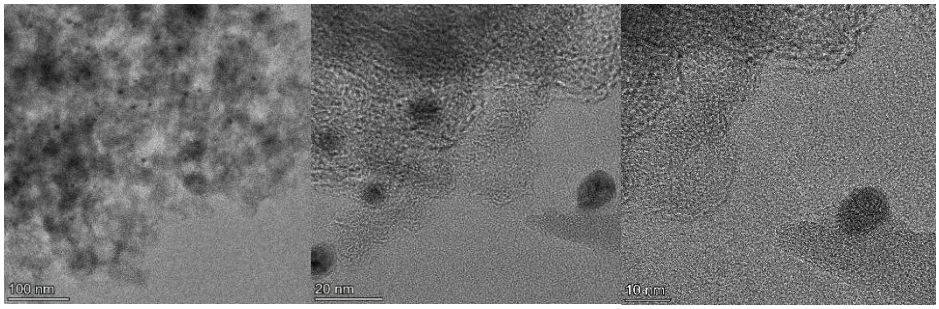

Figure 9: HRTEM of silver nanoparticles on carbon.

XRPD experiments were performed as well on the Fe, Co and NiPc@Ag/C catalysts but the spectra overlap the Ag/C XRD diffraction pattern. This behaviour is due to the low M-Pc amount in the catalysts as well as to a possible high dispersion onto the silver nanoparticles surfaces, forming an amorphous film. To validate this hypothesis, a STEM-EDX analysis coupled with EDX mapping of Fe, Co, Ni, Ag and O elements was performed to investigate presence of metal phthalocyanines (M-Pc) onto silver nanoparticles. Figure 10 reports respectively the STEM images and the related EDX mapping of Fe-Pc@Ag/C (figure 10 a-d), Co-Pc@Ag/C (figure 10 e-h) and Ni-Pc@Ag/C (figure 19 i-n). A clear overlap of the M-Pc metal signals with regions of high silver density was observed, indicating an effective interaction between the nanoparticles and the phthalocyanine complexes.[14] This interaction is considered essential for establishing synergistic active sites involved in the catalytic reaction that will be investigate in the following paragraph by half-cell measurements.

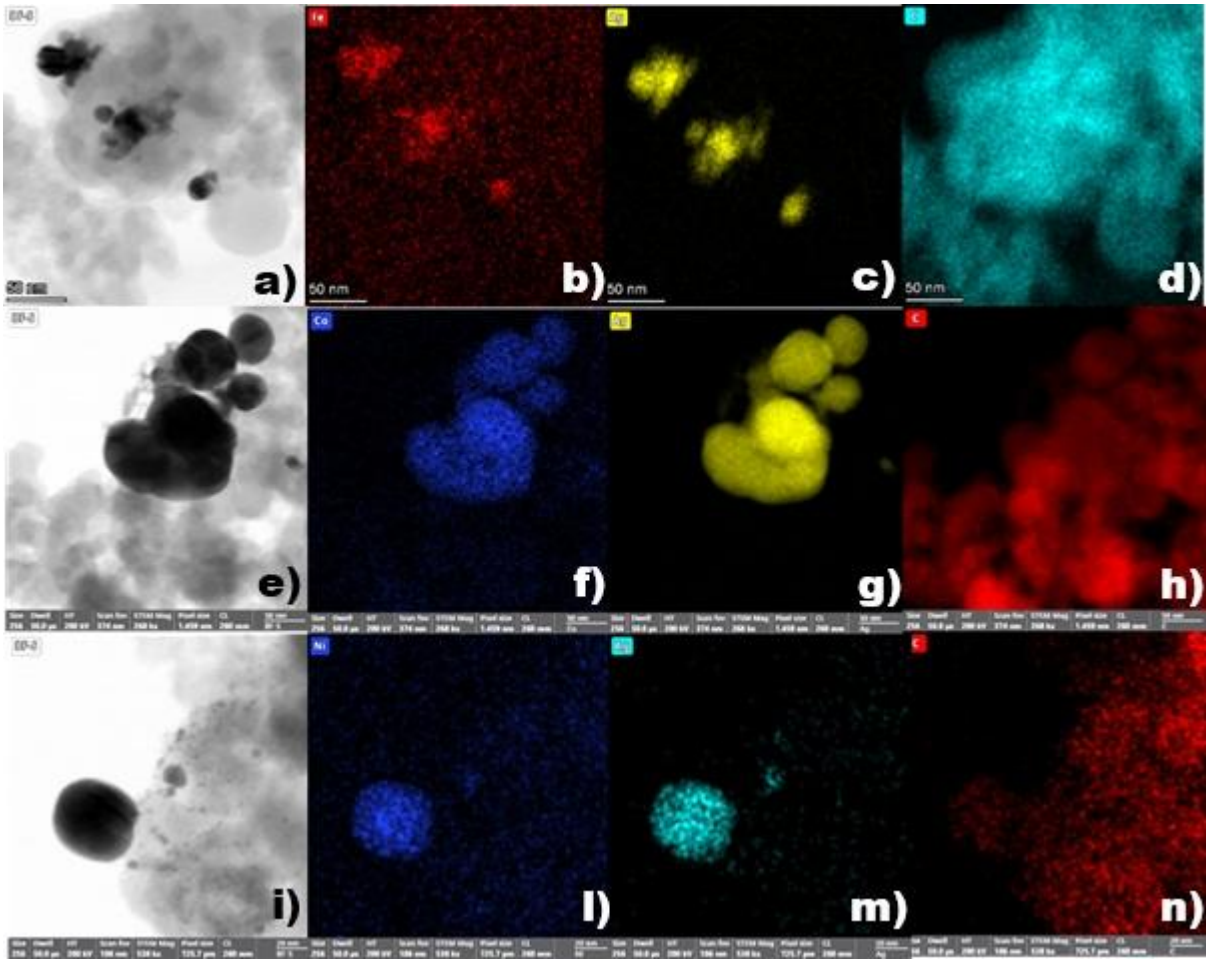

Figure 10: STEM imaging of FePc@Ag/C (a), CoPc@Ag/C (e) and NiPc@Ag/C (i) and their relative EDX mapping: FePc@Ag/C (b-d), CoPc@Ag/C (f-h) and NiPc@Ag/C (l-n).

3.4 Half Cell Measurements

To evaluate the electrocatalytic activity of the M-Pc@Ag/C catalysts (M = Fe, Co and Ni), half-cell electrochemical measurements were carried out. Each catalyst contains 20 wt.% silver (Ag) supported on carbon Vulcan, with the corresponding metal phthalocyanine (M-Pc,3wt.%) species uniformly distributed over the Ag/C substrate. The incorporation of silver aims to enhance the overall electrical conductivity of the catalyst and to promote synergistic interactions between the silver nanoparticles and the M-Pc complexes,[20,21] thereby facilitating electron transfer and improving the kinetics of the oxygen reduction reaction (ORR). Silver possesses high intrinsic electrical conductivity and moderate oxygen adsorption energy, both of which contribute to improved

charge transfer and stabilization of oxygen intermediates during ORR.[22,23]

Electrochemical tests were performed using a standard three-electrode cell configuration, using a rotating ring–disk electrode (RRDE) working electrode with a glassy carbon disk of 0.247 cm^2 and a platinum ring of 0.186 cm^2. The counter electrode is a platinum wire cleaned by flaming and the reference electrode is a mercury-mercury oxide electrode. All measurements were conducted in N_2 or O_2 saturated 0.1 M KOH (Sigma-Aldrich) aqueous solution (Milli-q water, 18 MΩ*cm). The potentials were referred to the reversible hydrogen electrode RHE.

The catalysts (7 mg) were first suspended in a H_2O-EtOH-Nafion 5% (700 mg – 700mg – 15 mg) solution by ultrasound treatment (1h at 45Hz) to obtain an ink that was drop-casted (10 µL) onto the glassy carbon disk electrode of the RRDE. The ink was dried under air before performing the measurements.

First, a set of 20 CVs in N_2 saturated 0.1M KOH solution was acquired in the 0-2.0 V vs RHE potential window at 20 mV s^{-1} scan rate (no iR drop compensation) to investigate the Ag/C electrochemical behaviour. Figure 11 reports the last voltammogram of the set. In the forward scan, the two oxidation peaks at 1.25 V and 1.33V. RHE correspond respectively to formation of Ag_2O and AgO species. At higher potentials, a broad increase of the anodic current between 1.6 and 1.8 V vs. RHE is attributed to the onset of the oxygen evolution reaction (OER). On the reverse sweep, the cathodic peaks at 1.33 and 1.21 V vs RHE

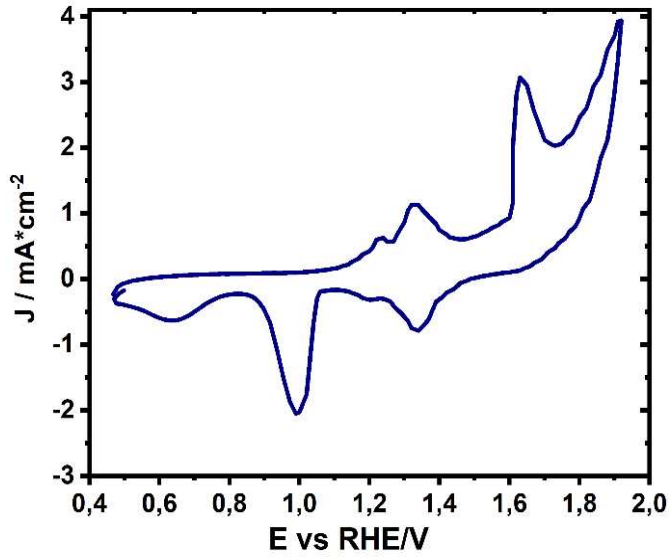

Figure 11: 20th cycle of CV on Ag/C in O_2-saturated 0.1M KOH

correspond to the stepwise reduction of $AgO \rightarrow Ag_2O$ and $Ag_2O \rightarrow Ag^0$. The cathodic peak centered at 1.0 V which are intermediates form that mediate the interaction with oxygen for ORR. RHE is associated with the reduction of $Ag(OH)_x$ and amorphous Ag_2O to Ag^0.[27]

The voltammogram reported in figure 11 is consistent with the CVs reported in literature Ag electrodes in alkaline electrolytes (Fig.11), where metallic silver Ag^0 is the main active form.

The catalysts Electrochemical Active Surface (ECSA) was indirectly evaluated from the double-layer capacitance (C_{dl}),[29] extrapolated from CVs performed at 20, 40, 60, 80, and 100 mV s^{-1} in N_2 saturated KOH 0.1M in the narrow potential window of 0.86-0.96 V vs RHE where the four catalysts have a capacitive behaviour. The slope of the linear fit of the capacitive current versus scan rate provides a C_{dl} value of 1990 μF, 1060 μF, 978 μF and 160 μF, respectively for FePc@Ag/C, CoPc@Ag/C, NiPc@Ag/C and Ag/C. Higher C_{dl} values are related with higher electrochemically active surface area (ECSA) values. The FePc@Ag/C> CoPc@Ag/C>NiPc@Ag/C>Ag/C, C_{dl} trend indicates that Ag nanoparticles improve the metal phthalocyanines dispersion, preventing their agglomeration.

To understand the catalysts activity for oxygen reduction reaction, RRDE experiments were performed in O_2 saturated 0.1M KOH. The linear sweep voltammetry (LSV) measurements were performed at rotation rates of 400, 800, 1200, 1600, 2000, and 2400 rpm with a scan rate of 5 mV s^{-1} between 1.2 V and 0 V vs. RHE; the ring electrode was maintained at 1.0 V vs. RHE for oxidizing the ORR reaction products. All data were corrected for iR drop. The RRDE experiments are reported in figure 12. The onset potentials for oxygen reduction at 1600 rpm is , 0.90 V vs RHE for Fe-Pc@Ag/C, 0.85 V vs RHE for Co-Pc@Ag/C, and 0.83 V vs RHE for Ni-Pc@Ag/C; correspondingly, the current densities recorded at 0.9 V (J@0.9V) were found to be respectively 0.75 mV Ag/C, 0.24239 mA cm^{-2}, 0.09813 mA cm^{-2}, and 0.03294 mA cm^{-2}. Fe-Pc@Ag/C has a superior catalytic activity among the tested materials. Ag/C has the lowest activity in the series, so the introduction of metal phthalocyanines improves the silver nanoparticles activity validating the presence of a synergistic effect

between Ag and M-Pc in the synthetized catalysts.[27] Among the M-Pc@Ag/C materials, the observed trend Fe > Co > Ni reflects the increasing difficulty of O_2 adsorption and activation along the transition metal series, as the M–N_4 site becomes less capable of stabilizing O_2 intermediates (O_2^-, OOH^-) due to the progressive downshift of the metal d-band center.[28]

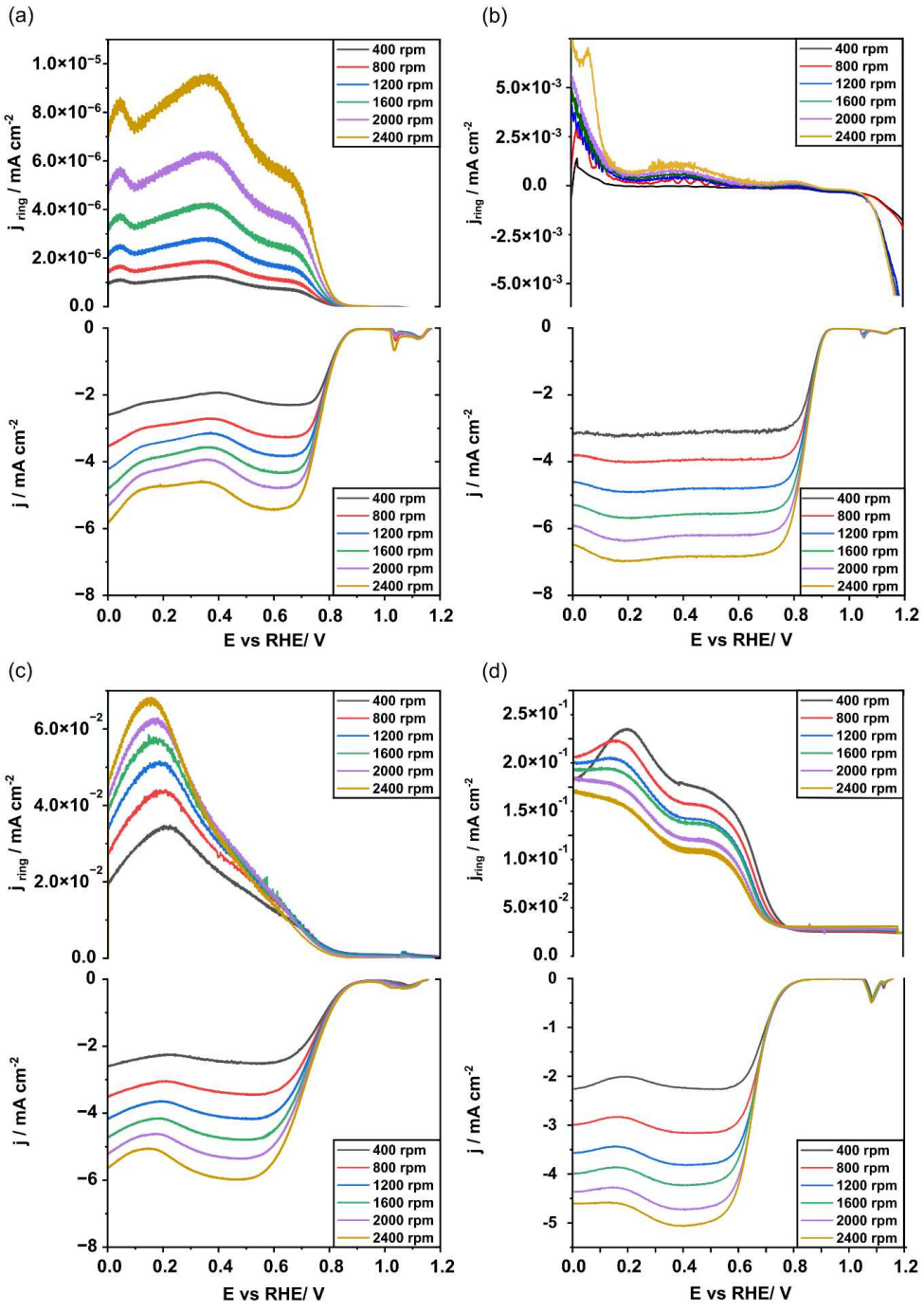

Figure 12: RRDE experiments composed of LSV on the disk (lower diagrams) and on the ring

(upper diagrams) in O_2 saturated KOH 0.1M of (a) CoPc@Ag/C, (b) FePc@Ag/C, (c) NiPc@Ag/C and (d) Ag/C.

The RRDE experiments provide information on the reaction mechanism of the oxygen reduction reaction. In particular, the number of electrons involved in the ORR and the percentage of $\%H_2O_2$ produced were calculated respectively applying eq.19 and eq. 20, where I_d is the disk current, I_r is the ring current, and N is the collection efficiency of the ring electrode (0.37).

$$n = \frac{4I_d}{I_d + \frac{I_r}{N}} \quad \text{Eq.19}$$

$$\%H_2O_2 = \frac{\frac{I_r}{N}}{I_d + \frac{I_r}{N}} \cdot 200 \quad \text{Eq.20}$$

The ORR promoted by Fe or Co or Ni-Pc@Ag/C follow a four-electron transfer pathway (n = 4), indicative of an efficient direct reduction of O_2 to OH^-. The generation of H_2O_2 was minimal, c.a. 1/2% H_2O_2, confirming the high M-Pc@Ag/C selectivity towards the desired $4e^-$ ORR mechanism. On the contrary, Ag/C produces up to ~15% H_2O_2 with a mean number of electrons of 3.7.

Figure 13a reports the average electron transfer number (n) during the ORR, while Figure 13b shows the corresponding molar percentage of H_2O_2 produced, as determined by RRDE measurements. For all Ag@MPc/C catalysts, n values remain close to 4 across the investigated potential range, accompanied by a low peroxide yield (~5%). This behavior indicates a highly selective ORR proceeding predominantly through a direct four-electron pathway. The improved selectivity, compared to Ag/C, can be attributed to the synergistic interaction between Ag nanoparticles and metal phthalocyanine active sites, which promotes the mono-step reduction of oxygen to water and suppresses the two-electron pathway leading to hydrogen peroxide formation.

In contrast, Ag/C exhibits a non-monotonic potential-dependent trend of the apparent electron transfer number between 0.8 and 0 V vs RHE, with calculated

n values exceeding the theoretical limit of 4, while the measured H_2O_2 yield remains below 10%. This apparent inconsistency is commonly reported for silver-based catalysts and is ascribed to additional faradaic contributions associated with silver surface redox processes, such as the formation and reduction of Ag–O species, occurring in the same potential window as the ORR. These processes contribute to the disk current without generating detectable peroxide at the ring, thereby leading to an overestimation of the electron transfer number derived from RRDE analysis. Such effects are significantly reduced in Ag@MPc/C catalysts, where the ORR is predominantly governed by $M–N_4$ active sites, resulting in more reliable RRDE-derived parameters and a well-defined four-electron reaction pathway.[34]

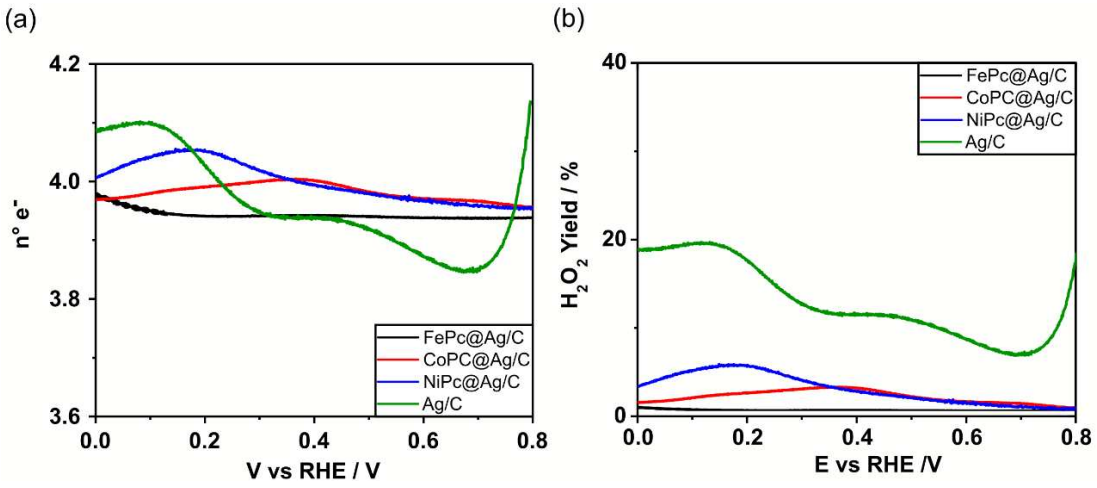

Figure 13: (a) number of electron involved during ORR reaction in the potential window of RRDE experiments. (b) molar % of H_2O_2 produced during ORR.

To further investigate the ORR reaction mechanisms, additional LSV measurements were recorded at 1600 rpm and 1 mV s^{-1} scan rate between 1.2 and 0 V vs. RHE to extrapolate Tafel diagrams (figure.14). The slopes of 93.72, 95,110 mV/dec and 113.00 mV/dec for FePc@Ag/C, CoPc@Ag/C, and NiPc@Ag/C e Ag/C, respectively indicate that the rate-determining step involves the first electron transfer to adsorbed O_2, forming O_2^{-}*[28], which is consistent with the ORR mechanism on transition-metal macrocyclic complexes in alkaline media.[31]The lower Tafel slope of FePc@Ag/C suggests more favourable kinetics

and faster charge transfer, in agreement with the more cathodic onset potential and the higher current density at 0.9 V vs RHE recorded in the LSV experiments.

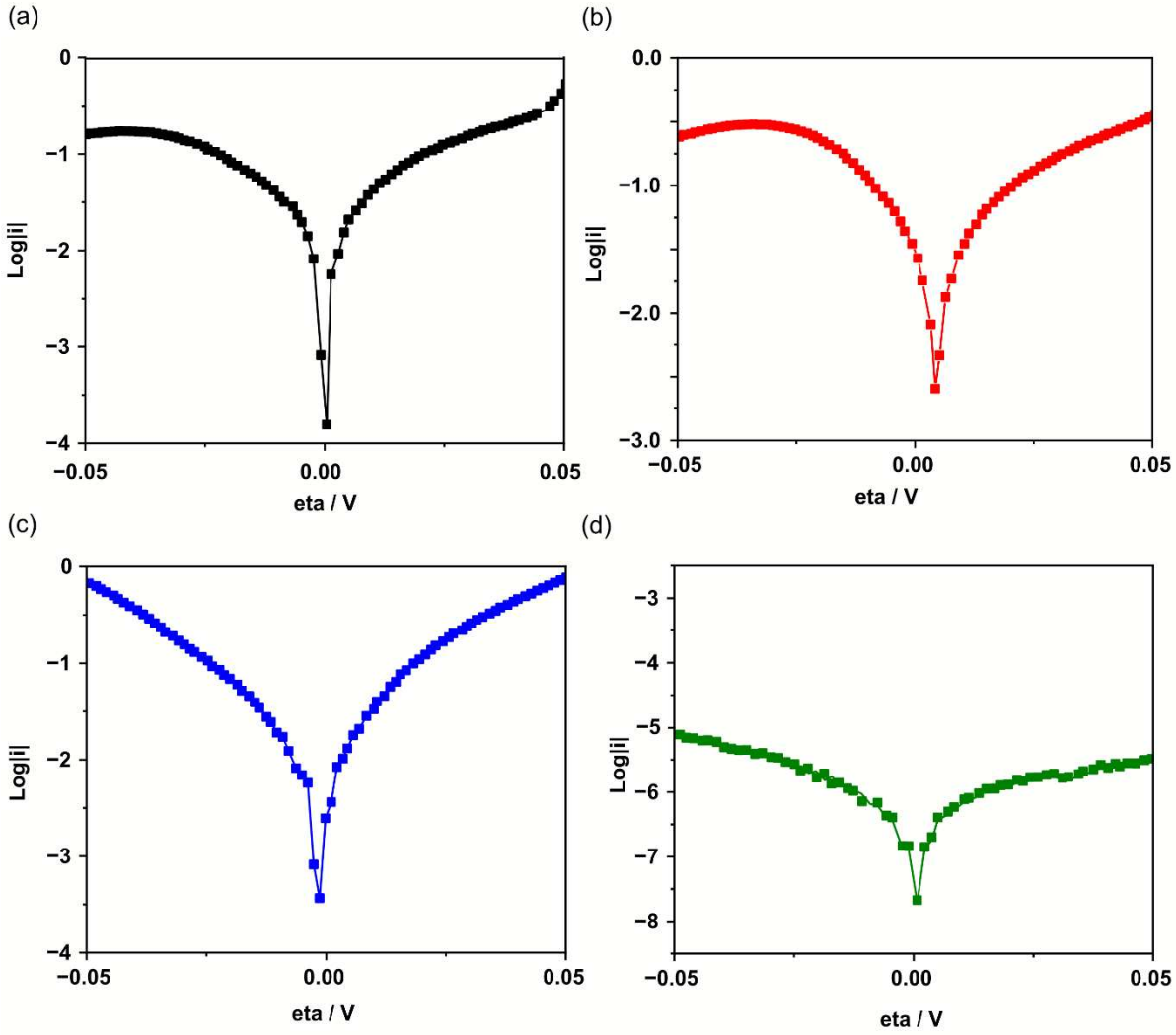

Figure 14: Tafel plot: (a) FePc@Ag/C, (b)CoPc@Ag/C,(c) NiPc@Ag/C and (d) Ag/C.

3.5 Conclusions

This preliminary study demonstrates that the deposition of metal phthalocyanine (Fe, Co and Ni) onto nanostructured Ag/C electrocatalysts improves the silver nanoparticles activity towards oxygen reduction reaction in alkaline media, opening the way to the fabrication of a novel class of electrocatalysts which can be employed as cathodes in alkaline membrane fuel cells.

Silver nanoparticles served as highly conductive anchoring sites, promoting

uniform dispersion of the M-Pc molecules and minimizing aggregation, as described by STEM-EDX analysis. On the other hand, the Fe, Co or Ni phthalocyanines metal centers provided active sites that facilitated oxygen adsorption and stabilized key reaction intermediates (OOH*, O*, and OH*) through charge delocalization within the conjugated macrocyclic framework.[31] In fact, this hybrid M-Pc@Ag/C architecture revealed higher ORR performances respect the Ag/C catalyst. Among the tested cathodes, FePc@Ag/C exhibited the highest ORR performance, with an onset potential of 0.90 V vs. RHE and a current density at 0.9 V of 0.242 mA cm^{-2}, outperforming CoPc@Ag/C and NiPc@Ag/C. The better Iron-based catalyst activity respect CoPC@Ag/C and NiPc@Ag/C can be ascribed to the optimal electronic configuration of the Fe–N_4 centers, which provides a balanced adsorption energy for oxygenated intermediates and facilitates the cleavage of the O–O bond[32].The synergistic coupling between the Fe–N_4 active sites and the conductive Ag nanoparticles enhances electron delocalization, improves the rate of charge transfer, and promotes the complete four-electron reduction of oxygen to water with minimal peroxide formation[33].As a future development of this preliminary investigation, DFT calculation will assess the M-Pc@Ag/C reactions mechanisms and how the phthalocyanines interacts with silver nanoparticles. Moreover, the FePc@Ag/C catalytic activity should be tested in a complete AEMFC.

3.5 References

1. Armaroli, Nicola, and Vincenzo Balzani. "The hydrogen issue." *ChemSusChem* 4.1 (2011): 21-36.
2. Wang, Yun, et al. "A review of polymer electrolyte membrane fuel cells: Technology, applications, and needs on fundamental research." *Applied energy* 88.4 (2011): 981-1007.
3. Nørskov, Jens Kehlet, et al. "Origin of the overpotential for oxygen reduction at a fuel-cell cathode." *The Journal of Physical Chemistry B* 108.46 (2004): 17886-17892.
4. Gasteiger, Hubert A., et al. "Activity benchmarks and requirements for Pt, Pt-alloy, and non-Pt oxygen reduction catalysts for PEMFCs." *Applied Catalysis B: Environmental* 56.1-2 (2005): 9-35.
5. Stamenkovic, Vojislav, et al. "Changing the activity of electrocatalysts for oxygen reduction by tuning the surface electronic structure." *Angewandte Chemie International Edition* 45.18 (2006): 2897-2901.
6. Zhang, Jiujun, ed. *PEM fuel cell electrocatalysts and catalyst layers: fundamentals and applications*. Springer Science & Business Media, 2008.
7. Spendelow, Jacob S., and Andrzej Wieckowski. "Electrocatalysis of oxygen reduction and small alcohol oxidation in alkaline media." *Physical Chemistry Chemical Physics* 9.21 (2007): 2654-2675.
8. Wang, Yun, et al. "Materials, technological status, and fundamentals of PEM fuel cells–a review." *Materials today* 32 (2020): 178-203.
9. Berretti, Enrico, et al. "Direct alcohol fuel cells: a comparative review of acidic and alkaline systems." *Electrochemical Energy Reviews* 6.1 (2023): 30.
10. Qaseem, Adnan, et al. "Pt-free silver nanoalloy electrocatalysts for oxygen reduction reaction in alkaline media." *Catalysis Science & Technology* 6.10 (2016): 3317-3340.

11. Liu, Shizhong, Michael G. White, and Ping Liu. "Oxygen reduction reaction on ag (111) in alkaline solution: A combined density functional theory and kinetic monte carlo study." *ChemCatChem* 10.3 (2018): 540-549.
12. Guo, J., et al. "Tuning the Electrochemical Interface of Ag/C Electrodes in Alkaline Electrolyte." *Journal of Physical Chemistry C* 117.43 (2013): 21927–21934.
13. Chen, K., et al. "Iron Phthalocyanine with Coordination Induced Electronic Localization to Boost Oxygen Reduction Reaction." *Nature Communications* 11 (2020): 4173
14. Yang, Shaoxuan, et al. "Recent advances in electrocatalysis with phthalocyanines." *Chemical Society Reviews* 50.23 (2021): 12985–13011.
15. Qaseem, A., F. Chen, X. Wu, and R. L. Johnston. "Pt-Free Silver Nanoalloy Electrocatalysts for Oxygen Reduction Reaction in Alkaline Media." *Catalysis Science & Technology* 6.9 (2016): 3218–3238.
16. Yang, Shaoxuan, et al. "Recent advances in electrocatalysis with phthalocyanines." *Chemical Society Reviews* 50.23 (2021): 12985–13011.
17. Li, Z., Zhou, Z., Sun, M., Wu, T., Lu, Q., Lu, L., ... & Huang, B. "A mechanism review of metal phthalocyanines as single-atomic catalysts in electrochemical energy conversion." *Chemical Science* 16.31 (2025): 14019–14037.
18. Yang, S., Y. Yu, X. Gao, Z. Zhang, and F. Wang. "Recent Advances in Electrocatalysis with Phthalocyanines." *Chemical Society Reviews* 50 (2021): 12985–13026.
19. Kim, Cheonghee, et al. "Insight into electrochemical CO_2 reduction on surface-molecule-mediated Ag nanoparticles." *Acs Catalysis* 7.1 (2017): 779-785.
20. Alsharaeh, Edreese, et al. "Green synthesis of silver nanoparticles and their reduced graphene oxide nanocomposites as antibacterial agents: A bio-inspired approach." *Acta Metallurgica Sinica (english Letters)* 30.1

(2017): 45-52.

21. Restrepo, Cindy Vanessa, and Cristian C. Villa. "Synthesis of silver nanoparticles, influence of capping agents, and dependence on size and shape: A review." *Environmental Nanotechnology, Monitoring & Management* 15 (2021): 100428.
22. Suriati, G., M. Mariatti, and A. Azizan. "Synthesis of silver nanoparticles by chemical reduction method: Effect of reducing agent and surfactant concentration." *International journal of automotive and mechanical engineering* 10 (2014): 1920-1927.
23. Alsharaeh, Edreese, et al. "Green synthesis of silver nanoparticles and their reduced graphene oxide nanocomposites as antibacterial agents: A bio-inspired approach." *Acta Metallurgica Sinica (english Letters)* 30.1 (2017): 45-52.
24. Chakraborty, Urmila, et al. "A flower-like ZnO–Ag 2 O nanocomposite for label and mediator free direct sensing of dinitrotoluene." *RSC advances* 10.46 (2020): 27764-27774.
25. Dai, Yong-Ming, et al. "Highly dispersed Ag nanoparticles on modified carbon nanotubes for low-temperature CO oxidation." *Applied Catalysis B: Environmental* 103.1-2 (2011): 221-225.
26. Ajitha, B., et al. "Role of capping agents in controlling silver nanoparticles size, antibacterial activity and potential application as optical hydrogen peroxide sensor." *RSC advances* 6.42 (2016): 36171-36179.
27. Linge, J. M., et al. "Oxygen reduction on silver catalysts electrodeposited on various nanocarbon supports." *SN Applied Sciences* 3.2 (2021): 1–10.
28. Haowei, Xu Ji, and Shuang Cheng. "Investigation into the electrochemical behaviour of silver in alkaline solution and the influence of Au-decoration using operando Raman spectroscopy." *RSC advances* 10.14 (2020): 8453-8459.
29. Lu Masa, Justus, et al. "Fundamental studies on the electrocatalytic properties of metal macrocyclics and other complexes for the electroreduction of O2." *Electrocatalysis in Fuel Cells: A Non-and Low-*

Platinum Approach. London: Springer London, 2013. 157–212.

30. Serapinienė, Birutė, et al. "On the electrochemically active surface area determination of electrodeposited porous Cu 3D nanostructures." *Coatings* 13.8 (2023): 1335
31. Khan, Fasiulla, et al. "Silver nanoparticles decorated phthalocyanine doped polyaniline for the simultaneous electrochemical detection of hydroquinone and catechol." (2021).
32. Masa, Justus, et al. "Fundamental studies on the electrocatalytic properties of metal macrocyclics and other complexes for the electroreduction of O2." *Electrocatalysis in Fuel Cells: A Non-and Low-Platinum Approach.* London: Springer London, 2013. 157–212.
33. Yang, S., Y. Yu, X. Gao, Z. Zhang, and F. Wang. "Recent Advances in Electrocatalysis with Phthalocyanines." *Chemical Society Reviews* 50 (2021): 12985–13026.
34. B. B., Philip N. Ross, and N. M. Marković. "Oxygen Reduction on Silver Low-Index Single-Crystal Surfaces in Alkaline Solution: Rotating Ring DiskAg (h kl) Studies." *The Journal of Physical Chemistry B* 110.10 (2006): 4735-4741.

4. Metal vapour synthetized PdAu alloys for direct formate anion exchange membrane fuel cells

4.1 Introduction

Carbon capture and utilization (CCU) has emerged as a promising strategy to address the excess of CO_2 in the atmosphere by converting it into useful products rather than simply storing it. Among the various utilization pathways, the electrochemical reduction of CO_2 (CO_2 RR) stands out for its potential to produce value-added chemicals and fuels, such as formate salts, using renewable electricity. [1,2]

Formate is particularly attractive as a liquid fuel due to its high energy density, low toxicity, non-flammability, and ease of handling and storage[3]. In fuel cells, formate can be electrochemically oxidized to recover the stored energy, effectively closing the carbon loop by regenerating CO_2, which can then be recaptured and reused.[4] Anion exchange membrane fuel cells (AEMFCs), operating in alkaline media, offer additional advantages, most notably the possibility of reducing the required loading of expensive noble metals, while also minimizing catalyst poisoning by CO intermediates[5].

Despite these benefits, catalyst degradation and limited long-term stability remain significant challenges. In acidic environments, traditional direct formic acid fuel cells often suffer from CO poisoning and require high loadings of platinum group metals (PGMs).[6,7] In contrast, operation under alkaline conditions, together with the use of bimetallic catalysts, has shown promise in overcoming these limitations.[8,9]

This study focuses on a carbon-supported PdAu bimetallic catalyst (PdAu/C), designed to combine the high catalytic activity of palladium with the beneficial electronic effects introduced by gold. Palladium is highly active toward formate oxidation but is susceptible to poisoning by CO-like intermediates.[10] Gold, on the other hand, tends to segregate to the surface in PdAu alloys, modifying the local electronic structure and enhancing the oxophilicity of the surface.[11] This

facilitates the removal of poisoning intermediates and stabilizes the active sites, promoting a more efficient and durable catalytic performance.[10,11]

The PdAu/C nanoparticles were synthesized using a metal vapor co-condensation method, which enables controlled nanoparticle growth without the use of organic surfactants or capping agents[12]. This avoids the need for high-temperature treatments that can alter particle size and composition, preserving the desired structural and surface properties[12].

A range of characterization techniques was employed to understand the structural, compositional, and electrochemical properties of the catalysts, including:

- Transmission Electron Microscopy (TEM) to analyze particle size and morphology,
- X-ray Diffraction (XRD) to investigate crystal structure and alloy formation,
- X-ray Photoelectron Spectroscopy (XPS) to study surface composition and electronic interactions,
- Electrochemical methods, including cyclic voltammetry and fuel cell testing, to evaluate catalytic activity, power output, and long-term stability.

Fuel cell tests using potassium formate as fuel were conducted to assess the real-world applicability of the catalyst, with a focus on power density, energy efficiency, and operational durability[6,7].

Overall, this work contributes to the development of efficient and scalable electrochemical systems for sustainable energy conversion and storage, offering a viable route for integrating CO_2 utilization into future energy infrastructures.

4.2 Metal Vapour Synthesis of PdAu electrocatalyst

The bimetallic PdAu catalyst supported on carbon (PdAu/C) was synthesized using the Metal Vapor Synthesis (MVS) technique, a physical-chemical method that enables the preparation of metal nanoparticles with controlled size and without the presence of capping agents or organic residues.[12] The core principle

of this technique involves the co-condensation of metal vapors with a cold organic solvent under high vacuum or inert atmosphere, at cryogenic temperatures. [10,11]

Specifically, palladium (Pd) and gold (Au) were vaporized separately by resistive heating inside two distinct tungsten crucibles coated with alumina.[13] These crucibles were placed inside a glass reaction chamber, which was first evacuated and then cooled using liquid nitrogen (−196 °C). Within the chamber, anhydrous acetone (100 mL) was introduced and rapidly solidified, forming a frozen solvent matrix.[11]

Upon controlled heating, Pd (150 mg, powder) and Au (50 mg, beads) vaporized simultaneously. Their vapors co-condensed with the frozen acetone, forming a solid metal-organic matrix. During this phase, individual metal atoms become solvated by acetone molecules, which prevents premature nucleation and allows for homogeneous atomic dispersion.[10] The co-condensation step was maintained for 1 hour, ensuring the formation of a uniform system of solvated metal atoms (SMA).[11]

After condensation, the reaction chamber was slowly warmed to the melting point of acetone (approximately −95 °C). At this temperature, the frozen matrix liquefies and releases the solvated metal atoms, which then begin to aggregate into nanoparticles, stabilized by the solvent environment. The resulting colloidal solution, with its characteristic red-brown color, indicates the presence of dispersed metal nanoparticles. The SMA solution was transferred, under cold conditions, to a Schlenk tube and stored at −40 °C to prevent oxidation or aggregation.[11]

The resulting PdAu-SMA solution (metal concentrations determined by ICP-OES: 0.85 mg mL^{-1} Pd and 0.4 mg mL^{-1} Au) was used for nanoparticle deposition onto a porous carbon support, Vulcan XC-72 (1.2 g). The carbon was dispersed in anhydrous acetone (50 mL), and 95 mL of the SMA solution was added. The suspension was stirred for 12 hours at room temperature (25 °C) to ensure homogeneous deposition of the nanoparticles onto the carbon surface. During this step, the nanoparticles anchor to the carbon support through physical interactions and the good wetting properties of acetone.

Following deposition, the solvent was removed by vacuum evaporation. The resulting black solid was washed with n-pentane (50 mL) to eliminate residual solvent or byproducts,and then dried under reduced pressure. ICP-OES analysis of the final dry material confirmed a metal loading of 9.0 wt% Pd and 3.0 wt% Au.

To compare the properties of the bimetallic catalyst with monometallic systems, Pd/C and Au/C catalysts were also prepared using the same MVS protocol with only one metal at a time. In both cases, ICP-OES analysis confirmed a total metal content of 10 wt%.

4.3 Physical characterization

The structural and morphological properties of the PdAu/C and Pd/C catalysts were thoroughly investigated using various advanced characterization techniques.[13,14,15] Powder X-ray diffraction analysis (XRD) in Figure 15 confirmed the formation of a PdAu alloy rather than a simple mixture of separate Pd and Au nanoparticles. The characteristic face-centered cubic (fcc)

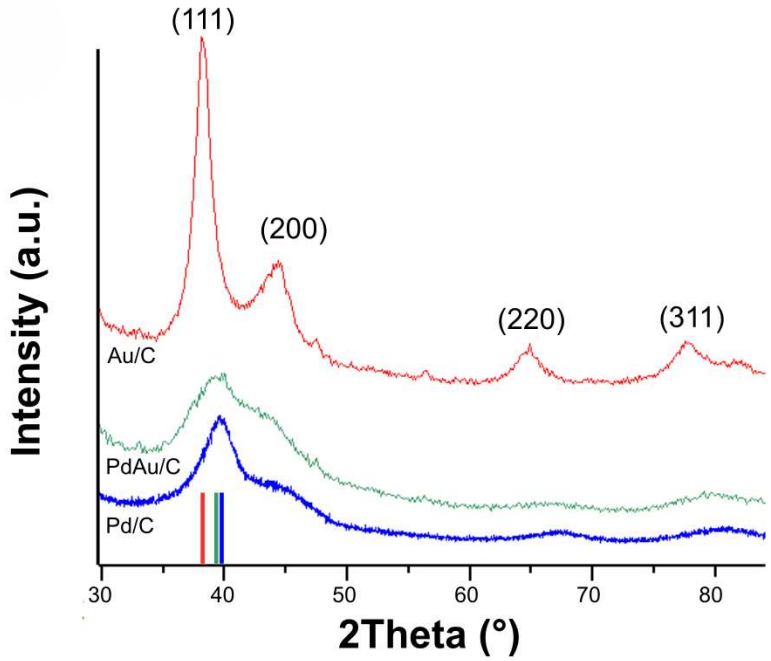

Figure 15:Powder XRD pattern of Au/C, Pd/C and PdAu/C samples

Pd reflections corresponding to the (111), (200), (220), and (311) planes showed a lattice expansion from 2.27 Å in Pd/C to 2.32 Å in PdAu/C, indicating alloy formation due to the incorporation of Au atoms102,103[15].

	Metal loading %	BET $m^2\ g^{-1}$	Tot. pore volume $cm^3\ g^{-1}$	Mean pore size nm
PdAu/C	$9_{Pd}3_{Au}$	85	0.81	33
Pd/C	10_{Pd}	137	0.81	25

Tab5: BET measurments PdAu/C, Pd/C.

Brunauer–Emmett–Teller (BET) surface area measurements indicated that both catalysts possess a macroporous–mesoporous structure, with specific surface areas of 85 $m^2\ g^{-1}$ for PdAu/C and 137 $m^2\ g^{-1}$ for Pd/C (Tab 5). These values reflect the textural properties important for catalytic performance.[16,17]

High-resolution transmission electron microscopy (HR-TEM) and scanning transmission electron microscopy (STEM) equipped with energy-dispersive X-ray spectroscopy (EDX) were employed to analyze nanoparticle size, morphology, and elemental distribution. Both catalysts exhibited well-dispersed nanoparticles of approximately 2–3 nm in diameter (figure 16). Lattice fringe analysis further confirmed the lattice expansion in PdAu/C consistent with alloy formation[18.] Elemental mapping through EDX demonstrated the coexistence of Pd and Au within the same nanoparticles, with an average composition of approximately 76 wt% Pd and 24 wt% Au. Analysis of individual nanoparticles revealed a Pd-rich core with an Au-enriched surface, a distribution known to enhance catalytic activity, particularly in electrochemical oxidation reactions.[19] This atomic arrangement on the nanoparticle surface was supported by elemental intensity profiles obtained from single-particle analysis.[20]

These findings are consistent with previous studies using X-ray absorption

spectroscopy (XAS) and X-ray absorption near-edge structure (XANES), which confirmed that both Pd and Au maintain a metallic state and form a true alloy in the nanoparticles[19,20].

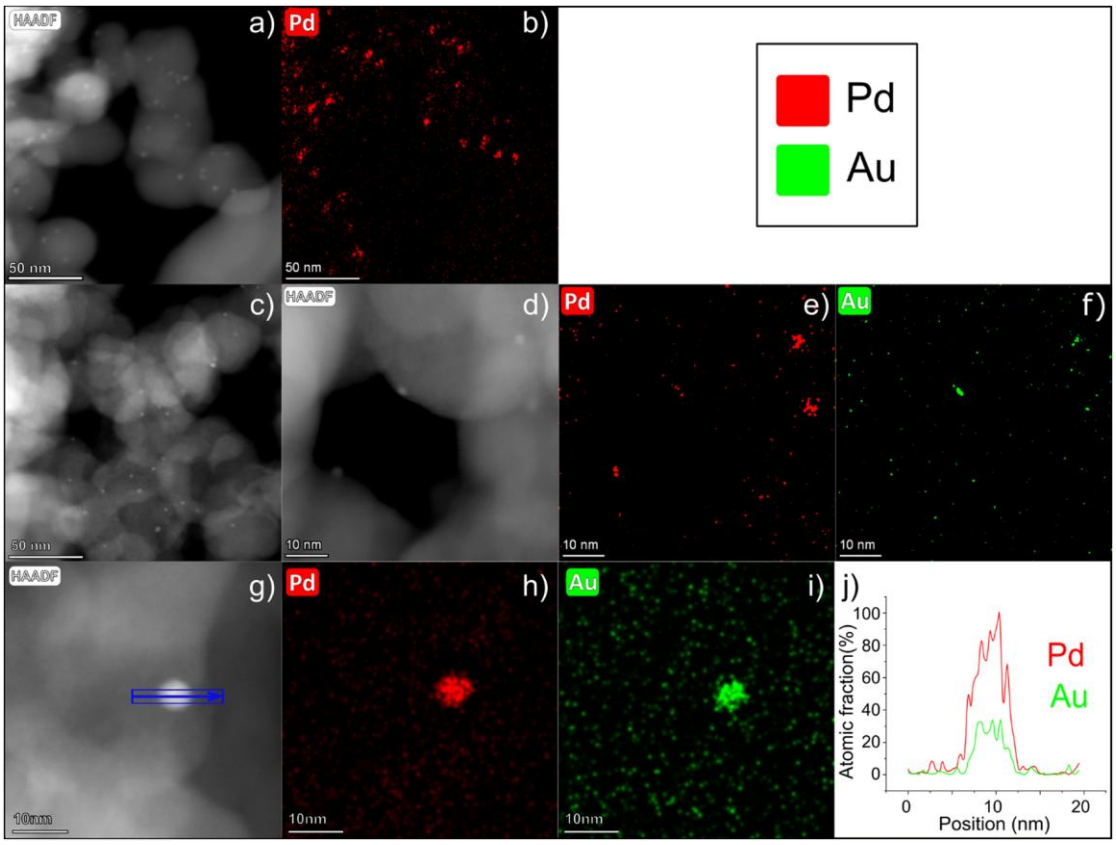

Figure16: (a-b) HAADF images of Au-Pd/C catalyst and (c-d) EDX analysis of the region shown in b.

4.4 Electrochemical characterization

The electrochemical properties of the PdAu/C and Pd/C catalysts were investigated using cyclic voltammetry (CV), CO stripping voltammetry, and electrochemical impedance spectroscopy (EIS). CV measurements were carried out in a 2 M KOH aqueous solution saturated with N_2.As shown in Figure 17a both voltammograms exhibit four anodic and three cathodic peaks typical of palladium: the first anodic feature (A1) is attributed to the oxidative desorption of hydrogen, followed by the formation of Pd–OH species (A2), and finally the formation of Pd oxides (A3–A4). On the cathodic scan, a well-defined peak at approximately 0.7 V (C1) corresponds to the reduction of surface PdO, while

C2 and C3 are associated with Pd–H formation and hydrogen evolution, respectively.[21]

In figure 17-b for PdAu/C, the PdO reduction peak is anodically shifted compared to Pd/C, suggesting that the Pd atoms in the alloy are more resistant to oxidation and passivation.[22] The area under this peak was used to estimate the electrochemically active surface area (EASA), resulting in values of 33 m^2 g^{-1} for PdAu/C and 26 m^2 g^{-1} for Pd/C[22].

The catalysts ability to oxidize adsorbed species was further evaluated via CO stripping experiments[23]. The voltammograms show a notable difference in the

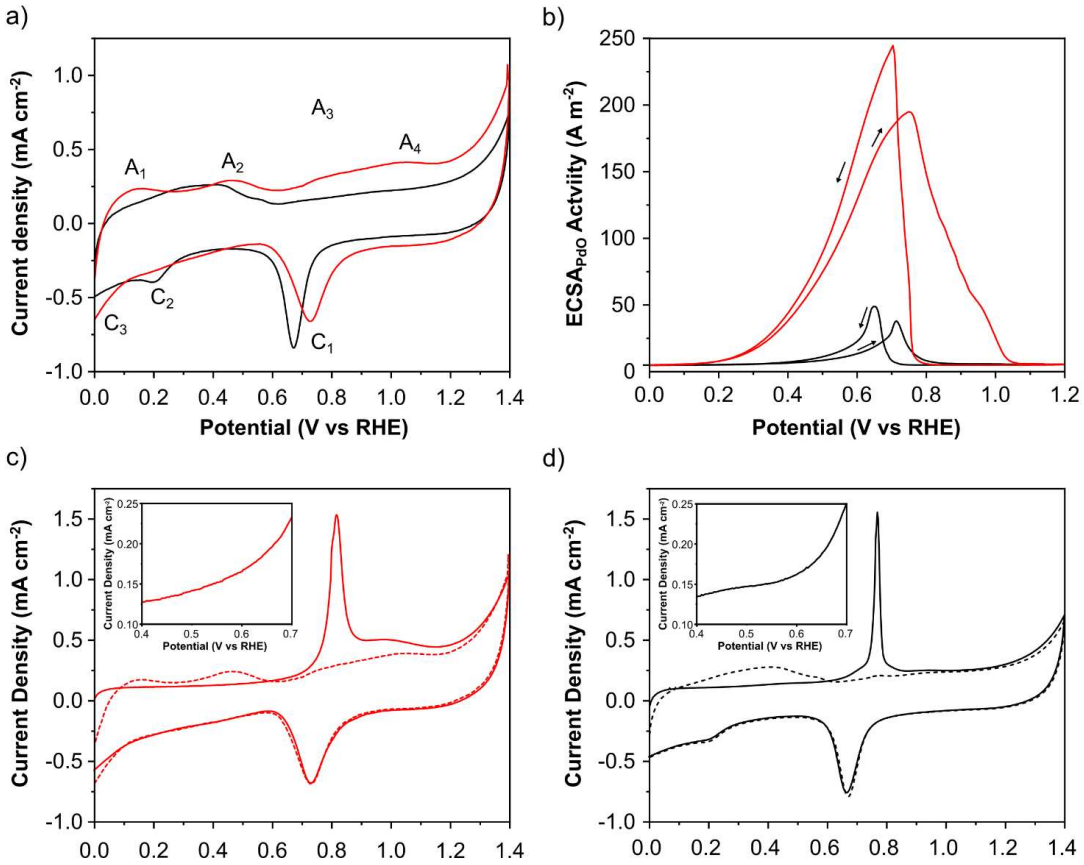

Figure17: Electrochemical characterization (a) CVs of PdAu/C (red) and Pd/C (black) (N2 saturated 2M KOH; 0 to 1.4 V (RHE) scan rate 50 mV s-1); (b) in N2 saturated 2 M HCOOK and 2 M KOH (0 to 1.2 V (RHE) at a scan rate 50 mV s-1. (c) COads stripping curves (d) show a zoom on the onset region of CO oxidation.

onset potential of CO oxidation, which occurs earlier for PdAu/C, indicating that the alloy facilitates CO removal more efficiently[24](figure 17 c-d). EASA values calculated from CO stripping curves were 48 m^2 g^{-1} for PdAu/C and 20 m^2 g^{-1}

for Pd/C.[24]The improved electrocatalytic performance of PdAu/C was confirmed by CV studies in 2 M potassium formate and 2 M KOH solution. The onset potential for formate oxidation on PdAu/C was recorded around 0.1 V vs RHE, approximately 200 mV earlier than for Pd/C. Moreover, the EASA-normalized anodic peak current density was about five times higher for PdAu/C. This result demonstrates that the Pd atoms on the surface of the alloyed catalyst are more active toward formate oxidation than those on pure Pd.

As the anode potential increases during the forward scan, the anodic current for Pd/C is limited due to progressive coverage of the surface by inactive Pd oxides. In contrast, PdAu/C maintains electrocatalytic activity even at potentials above 1.0 V vs RHE, whereas Pd/C becomes completely inactive beyond 0.85 V. In the reverse scan, an additional anodic peak appears around 0.7 V, attributed to the reactivation of Pd sites following oxide reduction, occurring earlier for PdAu/C. This further confirms its resistance to passivation.

At the nanoscale level, the improved performance of PdAu/C can be explained by multiple structural and electronic factors. The presence of Au dilutes and stabilizes isolated Pd atoms on the surface, which are known to be highly active.[19] In addition, Au-enriched surface regions enhance formate adsorption, while Pd-rich areas promote its oxidation[25]. The bifunctional interaction between Pd and the oxophilic Au facilitates the transfer of adsorbed OH species to the active Pd sites, improving the removal of intermediates such as CO.[26]

The electrocatalytic reactions can be described by the following equations:

$$Pd+Pd–HCOO(ad)\rightarrow Pd–H(ad)+Pd–(COO)(ad) \quad \text{Eq.21}$$

$$Pd–(COO)(ad) + Pd–H(ad) + Au–OH(ad) \rightarrow 2Pd + Au + H_2O + CO_2 \quad \text{Eq.22}$$

Therefore, the Pd–Au nanoparticle surface enhances formate oxidation via the synergistic combination of isolated, highly active Pd atoms and neighboring Au atoms that promote OH transfer, facilitating a bifunctional catalytic mechanism[27,28,29].

Electrochemical impedance spectroscopy (EIS) measurements performed at 0.4 V vs RHE further supported these findings. In Figure18-a, Nyquist plots revealed that PdAu/C displays a significantly lower charge transfer resistance (Rct) compared to Pd/C, despite having a similar resistance solution (Rs ≈ 3 Ω). In Figure 18-b, the double-layer capacitance (Cdl) values obtained via both EIS and CV techniques showed a consistent trend, with higher values for PdAu/C, indicating a rougher surface and improved ion accessibility.

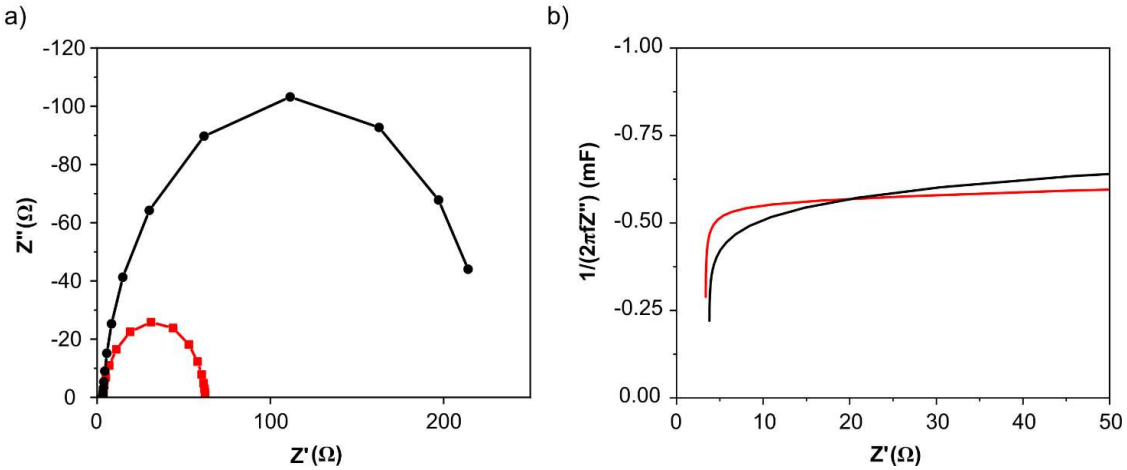

Figure18: Electrochemical impedance spectroscopy (EIS) of PdAu/C (red curves) and Pd/C (black curves) in KOH 2M at 0.4V vs RHE: a) Nyquist plot and b) Capacitance plot.

In Figure 18-b, capacitance plots (C vs Z') showed a steeper initial slope for PdAu/C, suggesting better conductivity and faster oxidation kinetics. Additionally, Cdl values obtained from CVs in the double-layer region (0.01 to 0.1 V s^{-1} scan rate) were 4.22 mF cm^{-2} for PdAu/C and 3.07 mF cm^{-2} for Pd/C, further supporting the enhanced electrochemical behavior of the bimetallic system.

4.5 Direct Formate Fuel Cell Testing

To evaluate the electrocatalytic performance under real operating conditions, direct formate fuel cell tests were carried out. The anode electrodes were prepared by coating nickel foam with homogeneous catalyst ink composed of the catalyst (Pd/C or PdAu/C) and PTFE as a binder. The metal loading on the electrode surface was 1.3 mgPd cm^{-2} for Pd/C and 1.2 mgPd cm^{-2} for PdAu/C.

The anion exchange membrane used was a FUMASEP FAA-3-30, pressed between the anode and cathode to form the membrane electrode assembly (MEA). As cathode electrocatalyst, a Fe–Co/C-based material supported on carbon cloth and previously developed by our group was used, also employing PTFE as a binder.

The fuel solution consisted of 1 M potassium formate and 1 M KOH (1:1 molar ratio), which was recirculated through the anode compartment at 1 mL min^{-1}. The cathode was fed with humidified oxygen at a flow rate of 0.1 slm. Polarization and power density curves were recorded under isothermal conditions at temperatures between 40 and 60 °C.

Both MEAs (Pd/C and PdAu/C) underwent five consecutive cycles, each consisting of a potential scan from open circuit voltage (OCV) to 0.1 V (10 mV s^{-1}), followed by a constant current density test at 0.05 A cm^{-2} until the cell voltage dropped to zero. A fresh fuel solution was used for each cycle. This protocol enabled an assessment of MEA stability during prolonged cycling under working conditions.

As shown in the results, the fuel cell with PdAu/C anode initially reached a peak power density of 140 mW cm^{-2}, compared to 100 mW cm^{-2} with Pd/C. After five cycles, both cells exhibited a slight performance decline, yet PdAu/C maintained a higher output (120 mW cm^{-2} vs. 90 mW cm^{-2} for Pd/C). During the constant current test, the PdAu/C cell consistently operated at higher voltages and longer durations (16–18 h) than the Pd/C cell (12–14 h), indicating improved energy and faradaic efficiency.

Specifically, the PdAu/C-based cell exhibited an energy efficiency (EE) of 33%, significantly higher than the 25% recorded for the Pd/C system. Similarly, faradaic efficiency (FE) reached 80% for PdAu/C and 65% for Pd/C. These values indicate a more effective utilization of the fuel and better energy conversion.

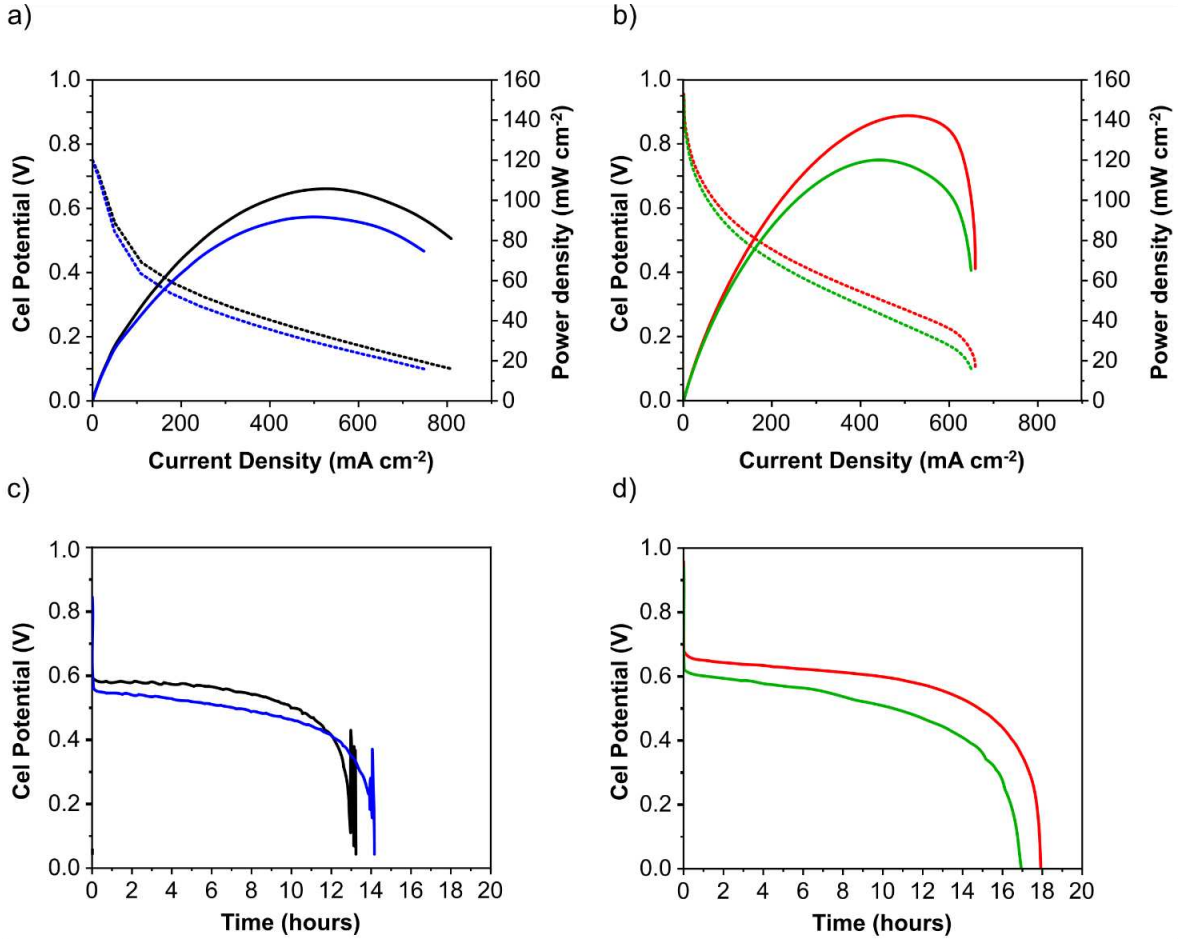

Figure 19: DFFC experiments containing the Pd/C (a and c) and PdAu/C anode (b and d). All cells used FeCo/C cathode catalyst and Fumatech FAA-3-30AEM. The fuel was 1 M HCOOK and 1 M KOH. Tcell = 60 °C: Figures (a) and (b) are voltage and power density current.

Catalyst stability under working conditions is a key factor in determining fuel cell durability. It is known that Pd is prone to electrochemical dissolution under highly alkaline conditions and elevated anodic potentials. However, when formate is used as fuel, such degradation is considerably reduced compared to ethanol, as previously shown in in-operando studies.[30] Thus, formate emerges as a more stable and promising fuel for alkaline direct fuel cells. Additionally, the PdAu/C catalyst demonstrated enhanced resistance to Pd surface passivation, as confirmed by the preceding electrochemical studies—contributing to longer-lasting performance[31].

Further stability testing was performed under single-pass fuel feed conditions, eliminating the effect of fuel concentration decrease or product accumulation during operation (Figure20-a). Under these conditions, the global cell reaction

is:

$$2HCOOK + KOH \rightarrow K_2CO_3 + H_2O + H_2 \qquad \text{Eq.23}$$

During these experiments, increasing the anode fuel flow rate resulted in higher and more stable cell voltages, suggesting that constant supply of fresh fuel and efficient removal of reaction products enhance operational stability. In contrast, varying the oxygen flow rate at the cathode had negligible impact (figure20-b). Nevertheless, at a flow rate of 0.3 slm, periodic voltage drops up to 100 mV were observed, which gradually recovered—likely due to intermittent flooding of the cathode with liquid water[32]. At higher flow rates, this effect was mitigated, as water accumulation on the cathode surface was less pronounced. Lastly, the effect of operating temperature was evaluated (Figure20-c). temperature. All experiments fuel composition 1 M KOH and 1 M HCOOK.

Power density curves recorded at 60 °C showed higher performance compared to those at 40 °C, as expected for fuel cell systems. However, up to a current density of 150 mA cm^{-2}, the power output remained similar at both temperatures, also reflected in the stable voltage profiles at constant current density (0.05 A cm^{-2}) for both temperatures.

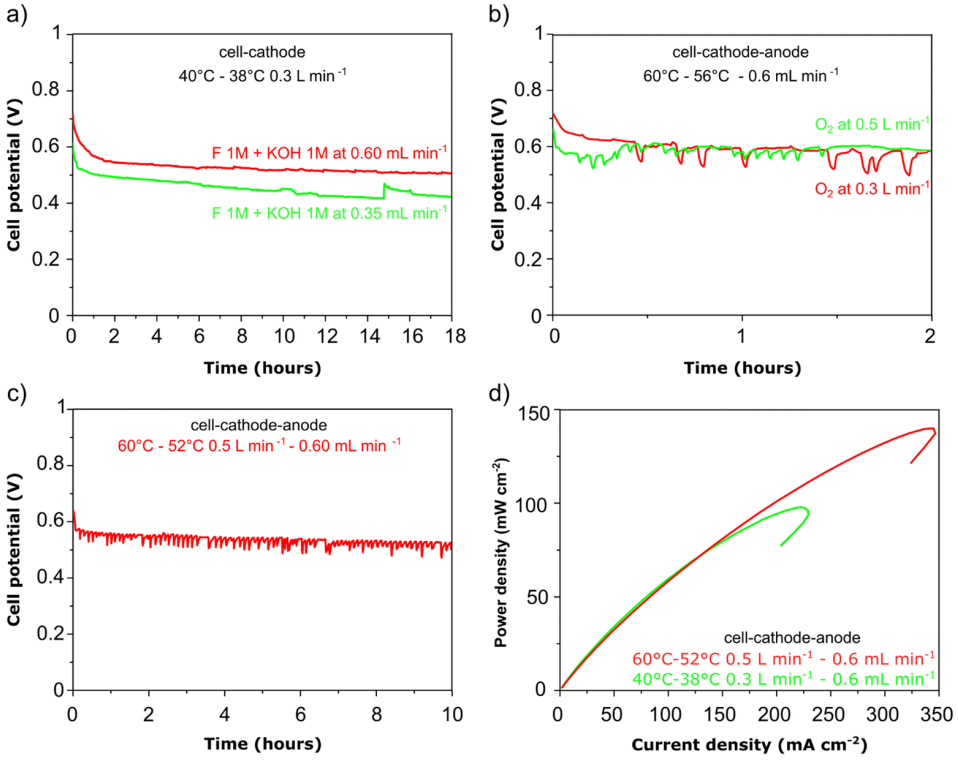

Figure 20**:** DFFC stability experiments carried out a single pass fuel feed (galvanostatic – 0.05 A cm^{-2}). (a) Variable anode flow; (b) variable cathode flow; (c) high anode and high cathode flow test showing stable power density delivery; (d) power density *vs.* current density curves at variable cell temperature. All experiments fuel composition 1 M KOH and 1 M HCOOK.

4.6 Conclusions

In this research work, a synthetic strategy was developed for the controlled preparation of PdAu bimetallic nanoparticles supported on carbon, employing the Matrix Isolation Synthesis (MVS) technique. This approach enabled the production of nanostructured systems free from stabilizing agents or residual ligands, allowing for a precise study of the intrinsic properties of the catalysts.[11] The combination of metals with distinct chemical and physical characteristics, such as Pd and Au, allowed modulation of the electronic and structural properties of the nanoparticles, significantly impacting their electrocatalytic performance.[15]

The choice of the PdAu system was driven by two complementary needs: on one hand, to exploit palladium's high catalytic activity for the oxidation of small organic intermediates; on the other, to introduce gold as a stabilizing element capable of modifying the electronic environment of Pd, reducing surface passivation and improving tolerance to adsorbed reactive intermediates like CO.[20] Morphological and structural characterizations (HR-TEM, STEM-EDX, XRD, BET) confirmed the formation of PdAu alloys at the nanometer scale with sizes between 2 and 3 nm, a face-centered cubic (fcc) crystalline structure, and a homogeneous distribution of elements within individual particles. EDX results also suggest a Pd-rich core composition with a Au-enriched surface, favorable for a bifunctional oxidation mechanism.

Electrochemical tests, including rotating disk electrode studies and cyclic voltammetry, revealed a higher electrochemically active surface area (EASA) and lower charge transfer resistance for the PdAu/C catalyst compared to the

monometallic Pd/C. Specifically, the onset potential for formate oxidation was shifted approximately 200 mV earlier, with current densities normalized to active surface area up to five times higher. These findings suggest that isolated Pd sites on the PdAu alloy surface are more active than those on pure Pd, and that the interaction with Au enhances the availability of adsorbed OH species, crucial for removing reaction intermediates.

Direct fuel cell tests (DFFCs) further confirmed the system's effectiveness. Under practical operating conditions, the PdAu/C catalyst exhibited not only higher power density (up to 140 mW cm^{-2}) but also improved long-term stability, maintaining good performance over several cycles. The PdAu/C cell achieved an energy efficiency of 33% and a faradaic efficiency of 80%, outperforming the Pd/C cell (25% and 65%, respectively). The longer operational lifetime and resistance to passivation or electrochemical dissolution phenomena make PdAu/C a promising material for use in alkaline direct formate fuel cells.[31]

In conclusion, the PdAu/C system developed in this work demonstrates how nanostructural engineering of bimetallic alloys can lead to significant improvements in electrocatalytic performance, offering a feasible path for designing more efficient, stable, and sustainable catalysts for clean energy devices.

4.7 References

1. Sun, Bin, et al. "Pt-Te alloy nanowires towards formic acid electrooxidation reaction." *Journal of Energy Chemistry* 85 (2023): 481-489.
2. Miller, Hamish Andrew, Francesco Vizza, and Alessandro Lavacchi. "Direct Alcohol Fuel Cells: Nanostructured Materials for the Electrooxidation of Alcohols in Alkaline Media." *Nanomaterials for Fuel Cell Catalysis*. Cham: Springer International Publishing, 2016. 477-516.
3. Du, Yadong, et al. "Graphene-based catalysts for CO2 electroreduction." *Wuli Huaxue Xuebao* 38 (2022): 2101009.
4. Castello, Carolina, et al. "Direct formate anion exchange membrane fuel cells with a PdAu bimetallic nanoparticle anode electrocatalyst obtained by metal vapor synthesis." *Energy Advances* 3.10 (2024): 2520-2529.
5. Guo, Longfei, et al. "Reconstruction of an AgPd nanoalloy with oxidation for formate oxidation electrocatalysis." *Journal of Materials Chemistry A* 10.26 (2022): 13998-14010.
6. Nguyen, Tien Q., et al. "Ambient temperature operation of a platinum-free direct formate fuel cell." *Journal of Fuel Cell Science and Technology* 12.1 (2015): 014501.Wang, L. Q., M. Bellini, J. Filippi, M. Folliero, A. Lavacchi, M. Innocenti, A. Marchionni, H. A. Miller, and F. Vizza. "Appl. Energy." *Applied Energy* 175 (2016): 479–487.
7. Wang, Junpeng, et al. "Strain effects on catalytic activity and stability of PdM nanoalloys with grain boundaries." *RSC advances* 15.22 (2025): 17317-17329.
8. Castello, C., Peruzzolo, T., Bellini, M., Pagliaro, M. V., Bartoli, F., Berretti, E., ... & Miller, H. A. (2024). Direct formate anion exchange membrane fuel cells with a PdAu bimetallic nanoparticle anode electrocatalyst obtained by metal vapor synthesis. *Energy Advances*, *3*(10), 2520-2529. F. Vizza. "Energy Technol." *Energy Technology* 7 (2019): 1800859.

9. Evangelisti, Claudio, et al. "Bimetallic Gold–Palladium vapour derived catalysts: The role of structural features on their catalytic activity." *Journal of catalysis* 286 (2012): 224-236.
10. López-Martín, Raúl, et al. "Gas phase synthesis of multi-element nanoparticles." *Nanomaterials* 11.11 (2021): 2803.
11. Suo, Yange, and I-Ming Hsing. "Synthesis of bimetallic PdAu nanoparticles for formic acid oxidation." *Electrochimica acta* 56.5 (2011): 2174-2183.
12. Łukaszewski, M., M. Soszko, and A. Czerwiński. "Electrochemical methods of real surface area determination of noble metal electrodes–an overview." *International Journal of Electrochemical Science* 11.6 (2016): 4442-4469.
13. Fang, Lan-lan, et al. "Determination of the real surface area of palladium electrode." *Chinese Journal of Chemical Physics* 23.5 (2010): 543-548.
14. Geraldes, Adriana Napoleão, et al. "Ethanol electro-oxidation in an alkaline medium using Pd/C, Au/C and PdAu/C electrocatalysts prepared by electron beam irradiation." *Electrochimica Acta* 111 (2013): 455-465.
15. Jover, J., M. García-Ratés, and Núria López. "The interplay between homogeneous and heterogeneous phases of PdAu catalysts for the oxidation of alcohols." *ACS Catalysis* 6.7 (2016): 4135-4143.
16. Szumełda, T., et al. "Hydrogenation of cinnamaldehyde in the presence of PdAu/C catalysts prepared by the reverse "water-in-oil" microemulsion method." *Applied Catalysis A: General* 487 (2014): 1-15.
17. Zhang, Xiangbo, et al. "Preparation of freestanding palladium nanosheets modified with gold nanoparticles at edges." *Nano Research* 11.8 (2018): 4142-4148.
18. Shan, Bin, et al. "First-principles-based embedded atom method for PdAu nanoparticles." *Physical Review B—Condensed Matter and Materials Physics* 80.3 (2009): 035404.
19. Silva, Tiago AG, et al. "Volcano-like behavior of Au-Pd core-shell nanoparticles in the selective oxidation of alcohols." *Scientific reports* 4.1 (2014): 5766.

20. Zhang, Xiangbo, et al. "Preparation of freestanding palladium nanosheets modified with gold nanoparticles at edges." *Nano Research* 11.8 (2018): 4142-4148.
21. Szumełda, T., et al. "Hydrogenation of cinnamaldehyde in the presence of PdAu/C catalysts prepared by the reverse "water-in-oil" microemulsion method." *Applied Catalysis A: General* 487 (2014): 1-15.
22. Ruiz-Montoya, José G., et al. "Effect of palladium on gold in core-shell catalyst for electrooxidation of ethanol in alkaline
23. Maroun, Fouad, et al. "The role of atomic ensembles in the reactivity of bimetallic electrocatalysts." *Science* 293.5536 (2001): 1811-1814.
24. Choun, Myounghoon, Sujik Hong, and Jaeyoung Lee. "Adsorbed hydrogen as a site-occupying species in the electrocatalytic oxidation of formate on Pd/C in alkaline medium." *Journal of The Electrochemical Society* 165.15 (2018): J3266.
25. Huang, Wenyu, et al. "Highly active heterogeneous palladium nanoparticle catalysts for homogeneous electrophilic reactions in solution and the utilization of a continuous flow reactor." *Journal of the American Chemical Society* 132.47 (2010): 16771-16773.
26. da Silva, Sirlane G., et al. "PdAu/C electrocatalysts as anodes for direct formate fuel cell." *Electrocatalysis* 6.5 (2015): 442-446.
27. Liu, Yang, et al. "High active carbon supported PdAu catalyst for formic acid electrooxidation and study of the kinetics." *The Journal of Physical Chemistry C* 114.49 (2010): 21417-21422.
28. Yuan, D. W., and Z. R. Liu. "Atomic ensemble effects on formic acid oxidation on PdAu electrode studied by first-principles calculations." *Journal of power sources* 224 (2013): 241-249.
29. Berretti, E., Pagliaro, M. V., Giaccherini, A., Montegrossi, G., Di Benedetto, F., Lepore, G. O., ... & Lavacchi, A. (2022). Experimental evidence of palladium dissolution in anodes for alkaline direct ethanol and formate fuel cells. *Electrochimica Acta*, *418*, 140351.
30. Lafforgue, Clémence, et al. "Selected review of the degradation of Pt and Pd-based carbon-supported electrocatalysts for alkaline fuel cells:

Towards mechanisms of degradation." *Fuel Cells* 18.3 (2018): 229-238.
31. Bartrom, Amy M., and John L. Haan. "The direct formate fuel cell with an alkaline anion exchange membrane." *Journal of Power Sources* 214 (2012): 68-74.

5. Nanoalloys Bimetallic nickel-tungsten with palladium for hydrogen oxidation reaction

5.1 Introduction

Hydroxide exchange membrane fuel cells (HEMFCs) have emerged as a promising alternative to proton exchange membrane fuel cells (PEMFCs) for sustainable energy conversion technologies, primarily due to their ability to operate under alkaline conditions. This enables the use of non-platinum group metal (PGM) catalysts, as well as low-cost membranes and bipolar plates, thereby offering significant potential for cost reduction. Despite these advantages, the sluggish hydrogen oxidation reaction (HOR) kinetics in alkaline media remains a critical bottleneck, even on state-of-the-art PGM catalysts such as Pt whose intrinsic activity in alkaline electrolytes is markedly lower than in acidic environments. Consequently, the high PGM loadings still required at the anode undermine the overall economic viability of HEMFC systems.

To overcome this limitation, considerable efforts have been dedicated to the development of electrocatalysts that combine high intrinsic HOR activity, long-term durability, and reduced reliance on PGMs. Among the various approaches explored, engineering the catalyst support using transition metal-based alloys has attracted particular attention, as it allows modulation of surface electronic properties and enhancement of interfacial reaction dynamics.

In this study, we report the design and synthesis of a nanostructured HOR electrocatalyst consisting of a binary nickel–tungsten (Ni-W) alloy support decorated with 10 wt% of palladium (Pd). The Ni-W alloy serves as a robust, corrosion-resistant, and electronically tunable substrate that promotes favorable hydrogen and hydroxide adsorption energetics. The small amount of Pd provides active sites for hydrogen dissociation, while its interaction with the Ni-W support generates synergistic effects that enhance HOR kinetics. This catalyst architecture delivers significantly improved electrocatalytic

performance compared to both monometallic Ni-based systems and conventional Pt/C, despite its substantially lower PGM content.

Ketjen black carbon was employed as the support material because of its high specific surface area, electrical conductivity, and a chemical stability, that promotes the uniform dispersion of metallic nanoparticles and enhance the efficiency of electron transfer during the catalytic process.

Initially, the compound tungstic acid monohydrate ($H_2WO_4 \bullet H_2O$) was synthesized and served as a tungsten precursor for the synthesis of catalysts. Subsequently, with tungsten and nickel precursors, the synthesis was carried out to obtain catalysts with molar ratio Ni:W (5:1) supported on amorphous Ketjen black Carbon (Ck) in a 1:1 ratio (metal:carbon). The choice of carbon as a support is motivated by its high electrical conductivity, chemical stability, and its ability to maintain high active surface areas through good dispersion of the components. The synthesis in-volves the reduction of the metal precursors in situ on the carbon support. These materials were calcinated at different temperatures (400, 500, 600, and 700 °C); however, as reported in the literature, the temperature of 500°C showed the best results for obtaining the expected alloys and oxides.[1,2]

The morphology of the synthesized catalysts was characterized by transmission electron microscopy (TEM) and scanning electron microscopy (SEM) imaging and by X-Ray Diffraction (XRD). Their electrocatalytic activity for the oxidation and evolution of hydrogen was evaluated by cyclic voltammetry and linear scan voltammetry conducted in a half cell.

5.2 Material Synthesis and Characterization

The synthesis of Ni-W supported on carbon (Ck) was carried out through a multi-step process involving the preparation of intermediate precursors, followed by thermal treatment under a reducing atmosphere. In this study, nickel nitrate hexahydrate ($Ni(NO_3)_2 \cdot 6H_2O$), tungstic acid monohydrate ($H_2WO_4 \cdot H_2O$), and potassium tetrachloropalladate (K_2PdCl_4) were used as pre-cursors to provide Ni^{2+}, W^{6+}, and Pd^{2+} ions, respectively.

5.2.1. Preparation of the tungsten precursor solids (H2WO4•H2O)

In a 250 mL Erlenmeyer flask, 20 g of sodium tungstate dihydrate ($Na_2WO_4 \cdot 2H_2O$) were added to 40 mL of deionized water, followed by the addition of 80 mL of 6 mol L^{-1} hydrochloric acid. Immediately after mixing the reagents, the formation of a yellow emulsion was observed, which was maintained under vigorous mechanical stirring for 3 hours at 20°C. The resulting solid was filtered and repeatedly washed with deionized water, then dried in an oven for 8 hours at 105°C.

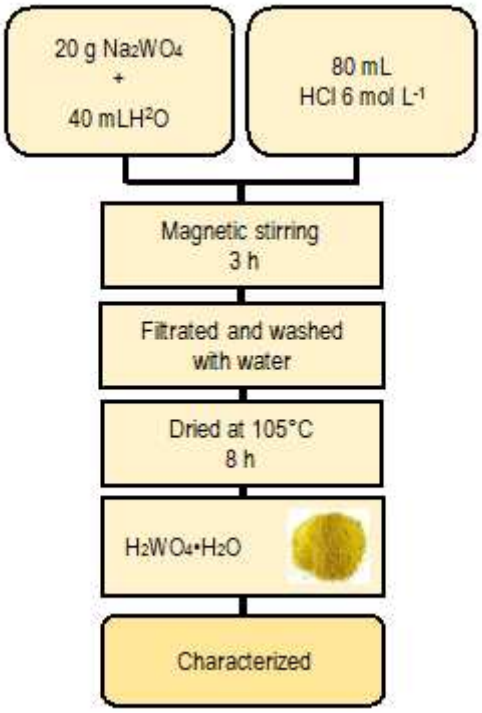

Figure 20: Flowchart describing the steps involved in the synthesis used for obtaining the precursor $H_2WO_4 \bullet H_2O$ precursor.

The tungstic acids can be obtained with different hydration degrees depending on the synthetic conditions such as temperature and concentration of the used acid. The synthesis followed the conditions to obtain the hydrate acid (Equation 1).

Na2WO4 (aq) + 2HCl (aq) → H2WO4•nH2O (s) + 2NaCl (aq) Eq.24

5.3 Synthesis of Ni4W/Ck alloys.

First, Ni4W precursors were synthesized by microwave heating route. Briefly, 3.03 g of nickel nitrate hexahydrate (Ni(NO3)2·6H2O) was dispersed into 3 mL H2O and 0.5 g of tungstic acid (H2WO4•H2O) into 1,2 mL of ammonia NH3·H2O and mixed in a 25 mL microwave glass vessel, followed by the addition of 15 mL ethylene glycol. After stirring for 20 min, the mixture was irradiated in the microwave reactor (CEM Mars 6 Synthesis) at 200 °C for 6 min with continuous magnetic stirring. After cooling to room temperature, the green powders were collected by centrifugation, washed with water and dried at 60°C overnight. The obtained Ni4W precursors was annealed in 5:95 H2/N2 atmosphere at 500 °C with a heat ramp of 5°C/min for 1 h. Ni4W was subsequently physically mixed with carbon Ketjen black (CK) in a 1:1 mass ratio using a ball mill operated at 10 rpm for 30 minutes and this sample was named Ni4W/Ck.

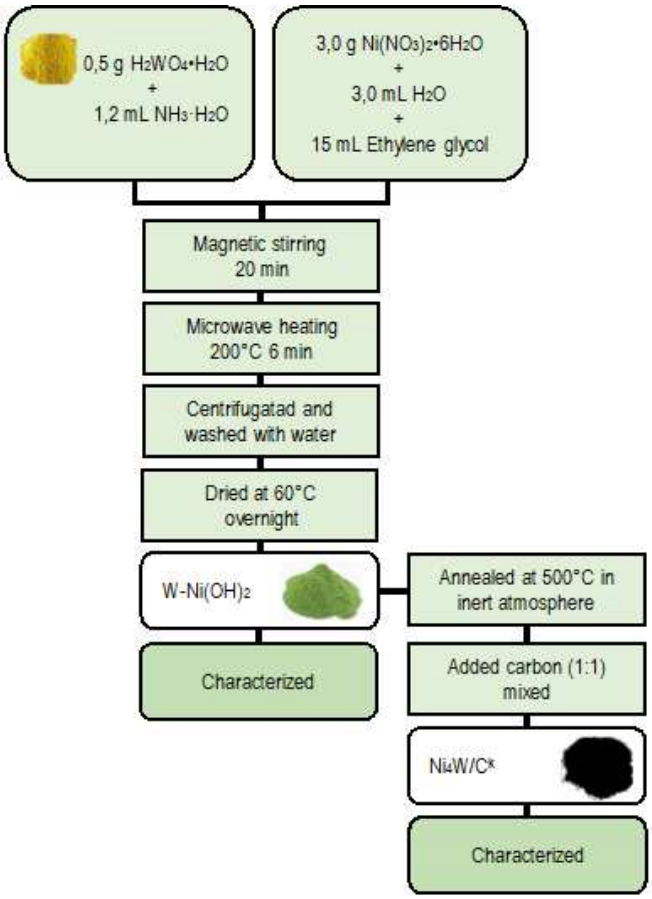

Figure21: Flowchart describing the steps involved in the synthesis used for obtaining the Ni4W/Ck.

5.4 Synthesis of Pd@Ni4W/Ck

Ni4W/Ck (0,1 g) was suspended in water (250 mL), stirred vigorously for 30 min and sonicated for 30 min. To this mixture, a solution of K2PdCl4 (0,03 g) in water (15 mL) was slowly added with peristaltic pomp (1 mL min-1) under vigorous stirring, followed by 2,1 mL of KOH aqueous solution (2.5M) and after 11 mL of ethanol, was then added to the resulting mixture, which was then heated at 80 °C for 60 min. The desired product Pd@Ni4W/Ck was filtered off, washed several times with distilled water to neutrality and finally dried at 40°C overnight.

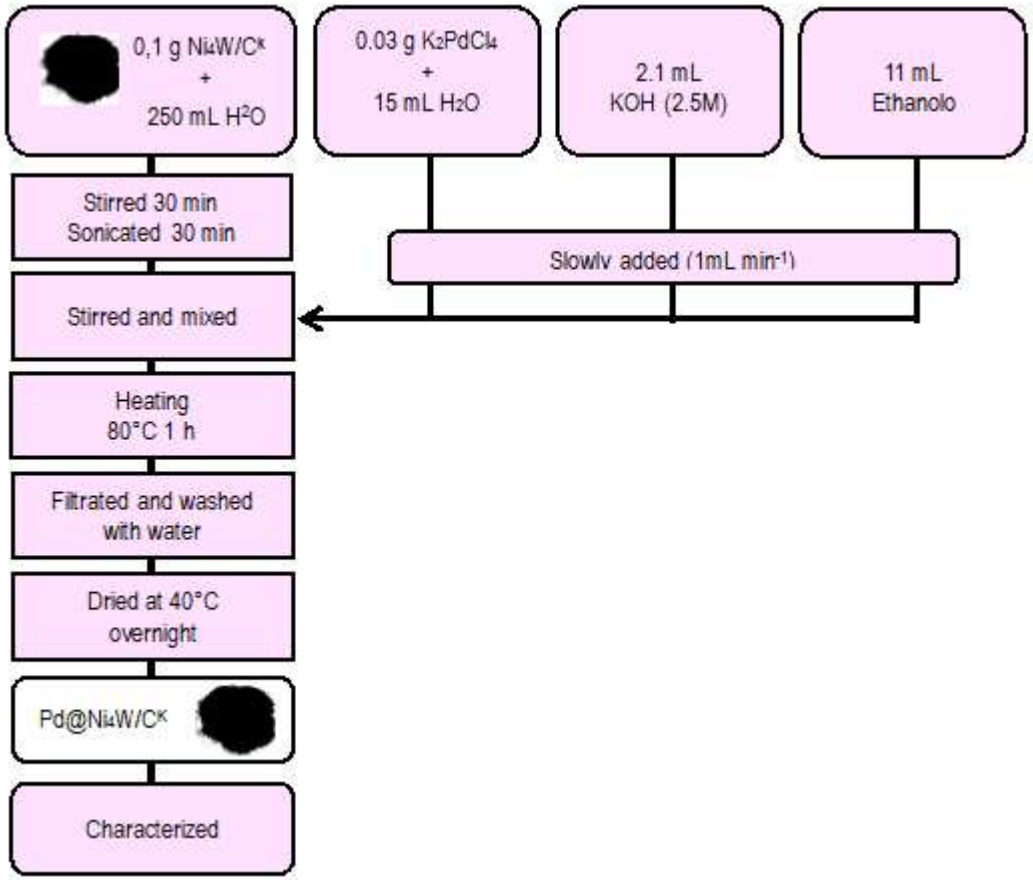

Figure 22: Flowchart describing the steps involved in the synthesis used for obtaining the Pd@Ni4W/Ck.

5.5 Physical characterization

The morphological and structural characterization of the Ni and W catalysts was performed to confirm the formation of the desired Ni_4W bimetallic alloy and to determine its distribution on the carbon support. Furthermore, this analysis was employed to rationalize the structure of the Ni_4W
bimetallic systems in terms of lattice parameters and the degree of crystallinity of the nanoparticles, as well as to verify the presence and distribution of palladium within the catalyst.

5.5.1. X Ray Diffraction

Figure 22 shows the powder X-ray diffraction pattern of tungstic acid monohydrate (H2WO4*H2O) where a typical crystalline profile of tungstic acid monohydrate is shown, as confirmed by comparison with CARD 18-1418 from the Joint Committee on Powder Diffraction Standards (JCPDS). [3,4,5,6]

All the diffraction peaks of the sample can be attributed to orthorhombic tungstic acid monohydrate, $H_2WO_4 \cdot H_2O$, corresponding to the reflections (020), (111), and (002) at 2θ = 16.5°, 25.6°, and 34.9°, respectively. The narrow and intense peaks suggest good crystallinity of the sample, and the similarity with the reference pattern indicates that the sample exhibits a

satisfactory degree of purity. [3,4,6]

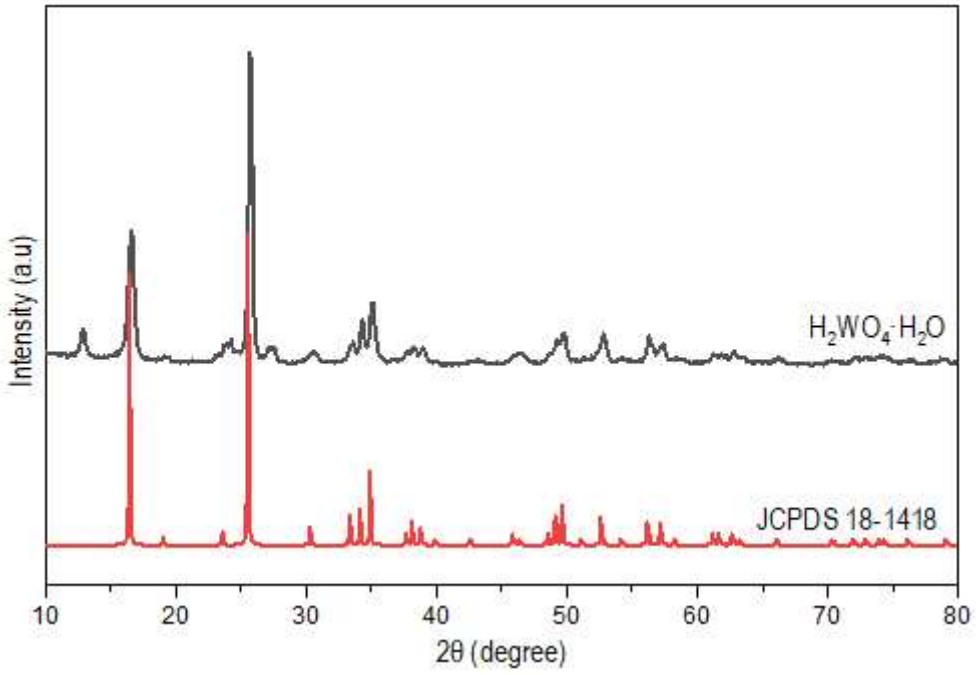

Figure 22: X ray diffraction pattern of the tungstic acid hydrate solid H2WO4•H2O

Figure 23 shows the X-ray diffraction pattern of the green precursor solid W–Ni(OH)₂before of calcination at 500°C in an inert atmosphere furnace. The diffraction peaks at 33.5°, 34.4°, and 60° correspond to the (101), (012), and (110) planes of α-Ni(OH)₂ (JCPDS 22-0444) doped with tungsten (W). The broad and low-intensity diffraction peaks, indicate a poorly crystalline lamellar structure, typical of α-Ni(OH)₂ and the absence of the well-defined peaks of β-Ni(OH)₂ confirms that the sample maintains the hydrated α-phase. Moreover, the slight shift and broadening of the main reflections suggests a local distortion of the lattice and an increase in the interlayer spacing, which can be attributed to the intercalation or partial substitution of tungstate (W–Ox) species within the hydroxide layers. Such features are consistent with the formation of a Ni–W layered double hydroxide (LDH) structure, in which tungsten ions are incorporated between the α-Ni(OH)2 lamellae, leading to structural disorder and expanded basal spacing. [7,8,9,10]

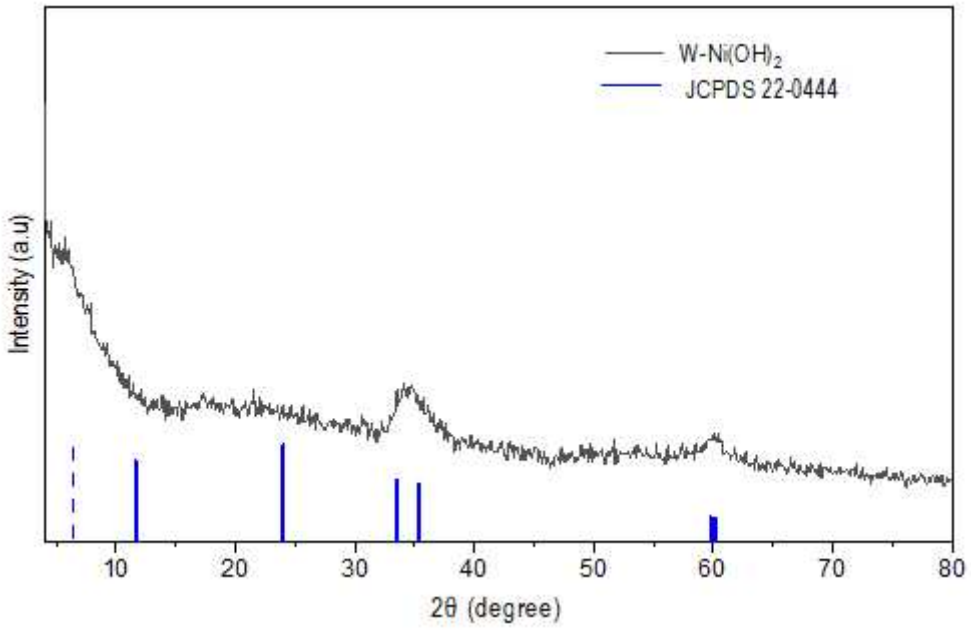

Figure 23: shows the X ray diffraction pattern of the green precursor solid W-Ni(OH)2 before calcination and blue lines indexed to reference standard XRD patterns for α-Ni(OH)₂ JPDS 22-0444.

After thermal treatment at 500°C under inert atmosphere H2/N2 (5:95), the composition and crystal phase obtained of the Ni4W/Ck were verified by X-ray powder diffraction (XRD) pattern (Figure 24). Hybrid diffraction signals indicating the presence of the Ni₄W alloy (JCPDF No. 65-2673) were observed,

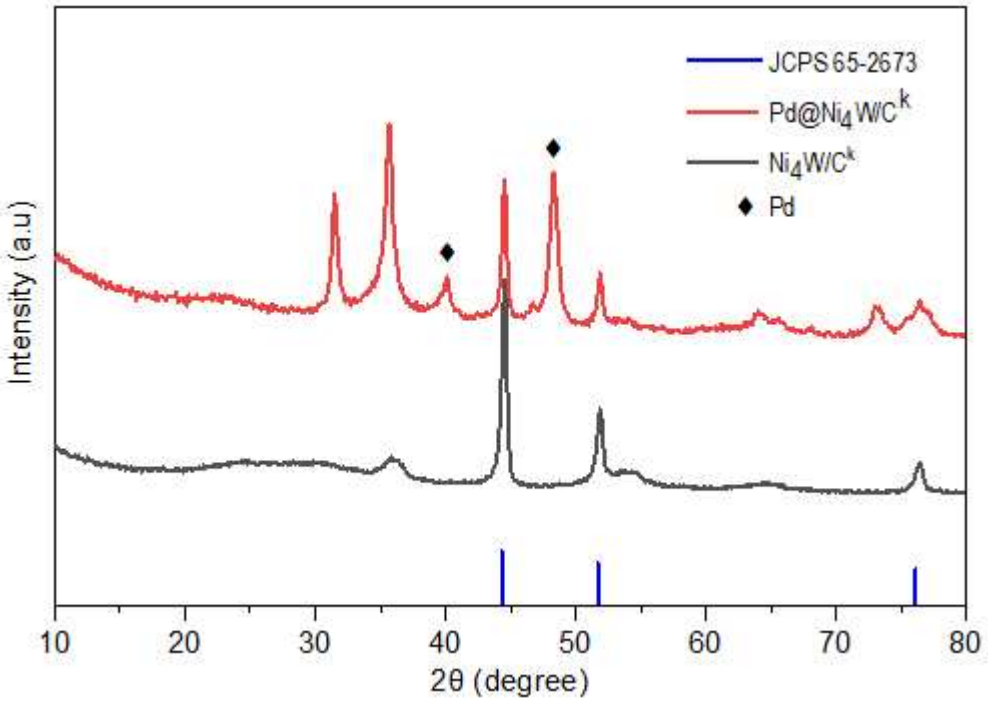

Figure 24: shows the X ray diffraction pattern of Ni4W/Ck and after palladium impregnation Pd@ Ni4W/Ck red line indexed to reference standard XRD patterns for Ni4W JPDS 65-2673.

highlighting the crucial role of the H_2/N_2 atmosphere in the synthesis of this alloy. Additional hybrid reflections can be assigned to mixed tungsten oxides (W–O), which are typically detected at lower diffraction angles (2θ < 40°) and were clearly observed in the Ni_4W/Ck sample. In turn, the diffraction peaks located at 40° (2θ) and 46° (2θ) can be ascribed to the (111) and (200) planes of metallic palladium, respectively, impregnated on the samples after the deposition reaction. [6,7,8,9,10]

The XRD pattern of the Pd@Ni_4W/Ck sample also revealed a higher crystallinity for some reflections compared to the pristine Ni_4W/Ck. Considering that the Pd impregnation was carried out in aqueous medium without hight thermal treatment, it is likely that a mild redox interaction occurred between Pd^{2+} ions and the metallic Ni–W surface, leading to the partial reoxidation of tungsten species. This phenomenon may account for the slight enhancement of diffraction signals associated with WO_2 phases (2θ <40°) observed in the Pd@Ni_4W/Ck sample.[7]

5.5.2. SEM and TEM

The morphology of the synthesized Ni_4W/Ck and Pd@Ni_4W/Ck sample were investigated by SEM and TEM characterization. The SEM analysis revealed that the Ni4W nanohybrids (Figure 25), exhibiting a morphological characteristics of the Ni_4W alloy as reported in the literature [7,10]. The low-magnification image shows agglomerated metallic particles with irregular morphology and heterogeneous size distribution, at higher-magnification, the surface appears compact and composed of interconnected nanosized grains, typical of Ni–W alloy structures formed through reduction processes.

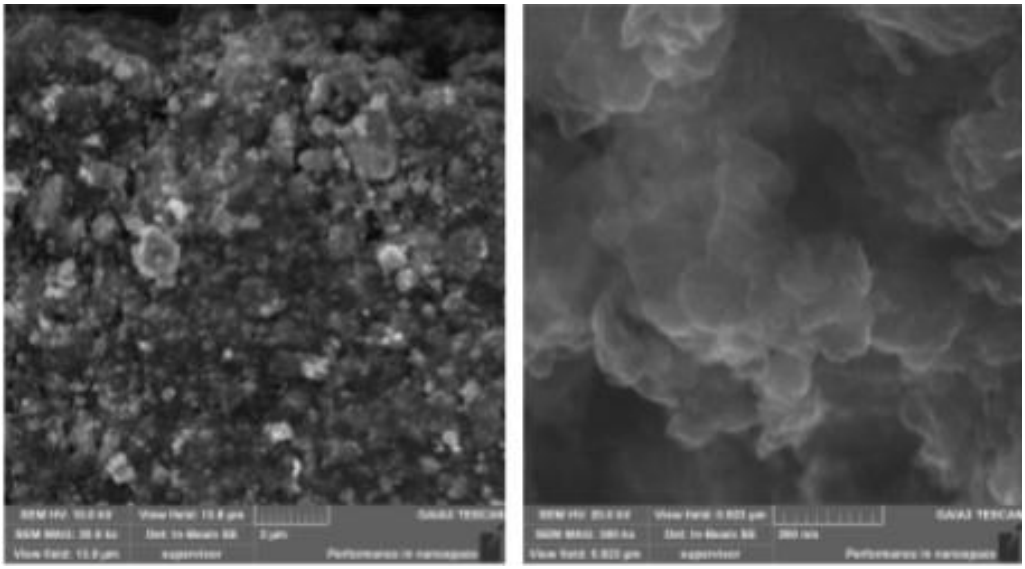

Figure 25: SEM micrographs of the Ni4W sample at different magnifications

Structural and compositional information was obtained by high-resolution transmission electron microscopy (HRTEM) combined with energy-dispersive X-ray spectroscopy (EDS) and scanning transmission electron microscopy (STEM). As shown in Figure 26, the HRTEM micrograph of the Ni_4W/CK sample reveals a high density of well-dispersed nanoparticles exhibiting clear lat-tice fringes with an interplanar spacing of 0.203 nm, corresponding to the (200) crystalline plane of the Ni_4W alloy. [7,10,11]

The nanoparticles display a pronounced crystalline contrast and a highly ordered atomic arrangement, indicating that the calcination process effectively promoted crystallization. The regular and parallel alignment of the lattice fringes further confirms the high crystallinity and well-defined structural order of the Ni_4W phase.

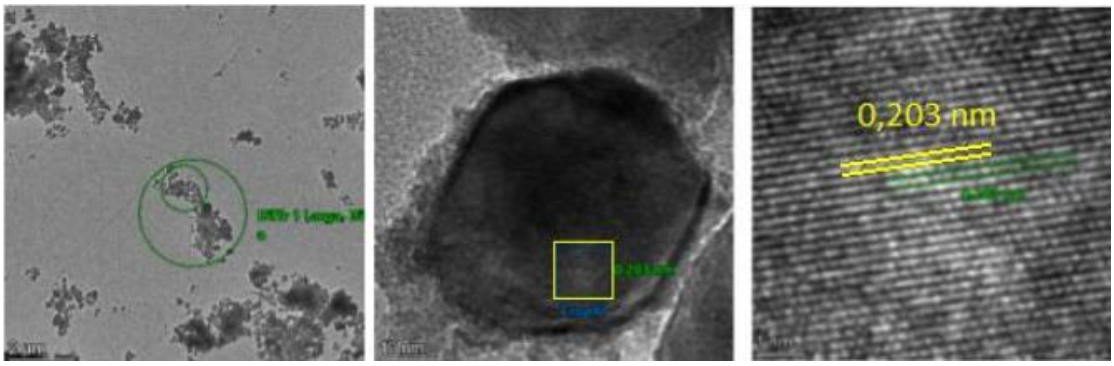

Figure 26: shows high-resolution transmission electron microscopy (HRTEM) images of the synthe-sized Ni–W structures.

Figure 27 presents transmission electron microscopy (TEM) images acquired using high-angle annular dark-field (HAADF) contrast along with the corresponding energy-dispersive X-ray spectroscopy (EDX) elemental maps for Ni, W, C and O. In the HAADF micrographs, agglomerates of nanoparticles exhibiting regions of higher contrast correspond to the alloy nanoparticles dispersed into the carbon support. The elemental mapping reveals the simultaneous and homogeneous distribution of Ni (blue) and W (green) throughout the nanoparticles, indicating that both metals are well dispersed within the structure. This co-localization supports the formation of the bimetallic Ni–W nanostructures, as expected during the calcination process. [7,10]

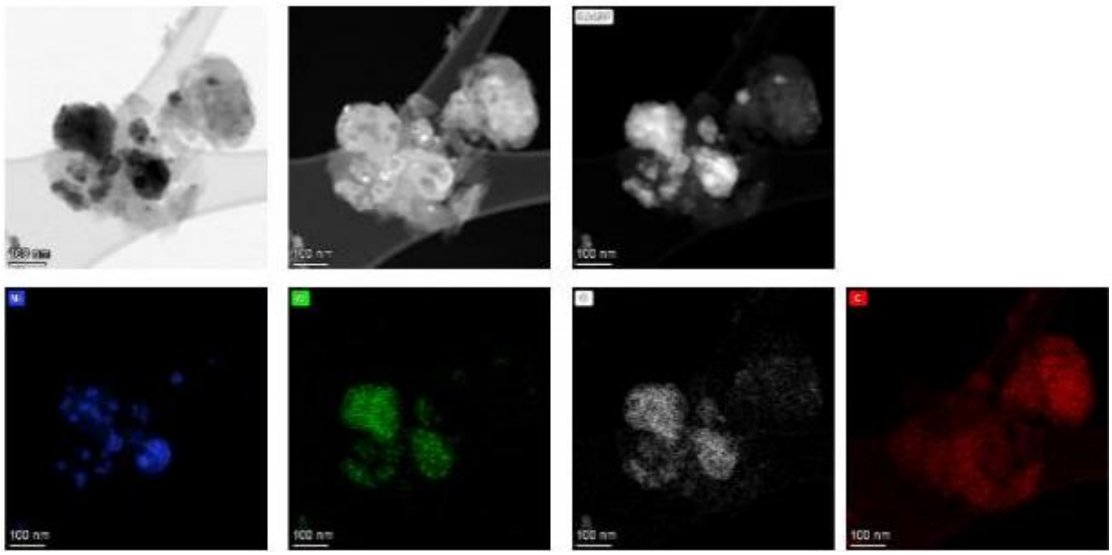

Figure 27: HAADF-STEM image EDX elemental maps of the Ni_4W/Ck solid. The distribution of nickel (Ni, blue), tungsten (W, green), oxygen (O, white), and carbon (C, red) is shown. The homogeneous co-localization of Ni and W indicates the formation of Ni–W alloy domains supported on the carbonaceous matrix.

In the Figure 28, it can be observed that after the impregnation synthesis (palladium addition), the material retained the structural basis of the pre-existing alloy (Ni_4W/C_k). A well-defined presence of palladium (Pd, yellow) is also evident, mainly distributed over the regions containing the Ni–W alloy. This

clearly confirms that palladium was effectively incorporated into the system and successfully deposited onto the carbonaceous support containing the Ni–W bimetallic phase. Carbon (C,red) exhibits a homogeneous distribution, corresponding to the conductive matrix that sustains the metallic nanoparticles. These morphological and compositional analyses therefore demonstrate that the carbon support containing the Ni–W alloy was successfully enriched with palladium, which is effectively dispersed over the bimetallic regions, confirming the success of the impregnation process and the formation of the Pd@Ni$_4$W/Ck catalyst.

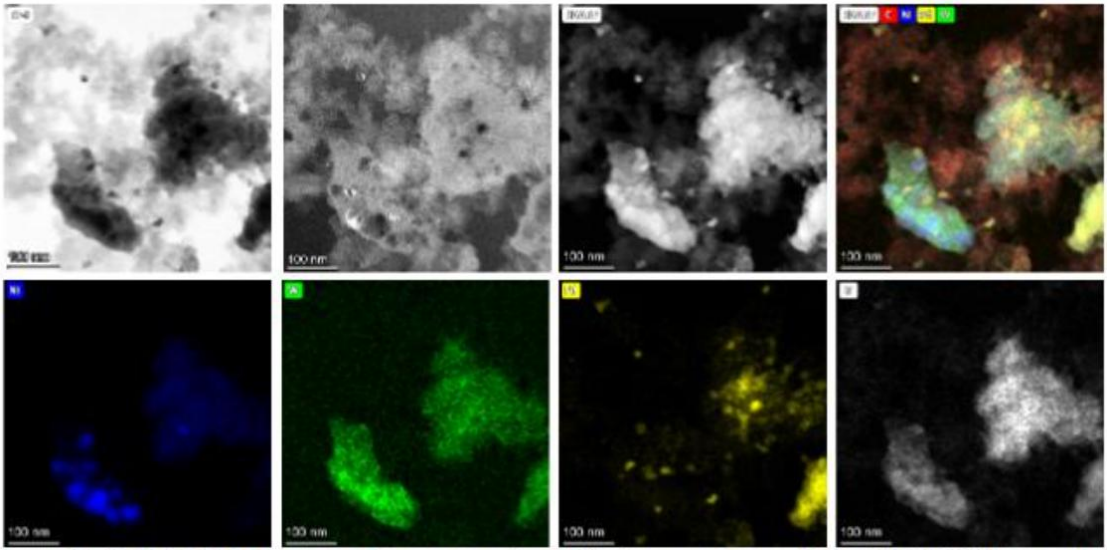

Figure 28. HAADF-STEM image and corresponding EDX elemental maps of the Pd@Ni$_4$W/Ck sample. The elemental distributions of nickel (Ni, blue), tungsten (W, green), palladium (Pd, yellow), and oxygen (O, white) are shown. The first three images were acquired in bright-field, dark-field, and high-angle annular dark field (HAADF) modes, respectively, highlighting the contrast differences related to local atomic density variations and the presence of heavy metals such as Ni, W, and Pd.

5.6 Electrochemical characterization

5.6.1. Half-cell measurements

The electrocatalytic performance of NiW/C and Pd@NiW/C catalysts was evaluated in an alkaline medium (0.1 M KOH) using a three-electrode configuration, with a reversible hydrogen electrode (RHE) as the reference, a

gold wire as the counter electrode, and a rotating disk electrode (RDE) as the working electrode. The catalyst ink was prepared by dispersing 0.0211 g of catalyst in a hydroalcoholic mixture containing 0.7 g of 2-propanol and 0.0196 g of Nafion. The suspension was ultrasonicated to achieve a uniform dispersion, and 10 µL of the ink were drop-cast onto a 0.196 cm^2 geometric area of glassy carbon disk and dried under ambient conditions. Considering that both catalysts consist of 50 wt% carbon and 50 wt% metal, the total metal loading on the electrode was 0.054 $mg \cdot cm^{-2}$, corresponding to 1.06×10^{-5} g of metal per electrode. For the Pd@NiW/C sample, where 10 wt% of the total metal fraction corresponds to Pd, the Pd loading was 0.0011 $mg \cdot cm^{-2}$. To activate the catalytic surface, 20 cyclic voltammetry (CV) cycles were performed in the potential range of –0.2 V to 0.6 V vs RHE. The current response stabilized after approximately five cycles, confirming rapid surface activation and the establishment of stable active sites for hydrogen-related reactions.

Linear sweep voltammetry measurements were subsequently carried out at a rotation speed of 1600 rpm, from –0.4 V to 0.4 V exploring both the HOR and HER branches, at 1 mV/s.

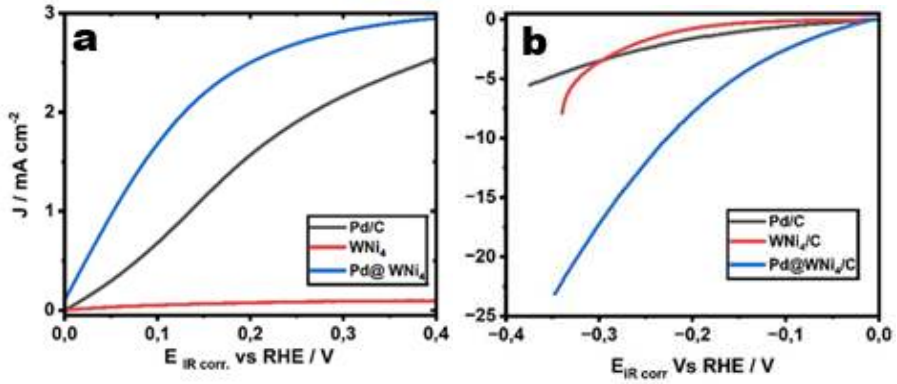

Figura 29: Linear Sweep voltammetry at 1600 rpm and 1 mv/S

a) HOR in KOH 0.1M b)HER in KOH 0.1M;

For the HOR process at 0.1 V vs RHE, the current densities were 1.68 $mA \cdot cm^{-2}$ for Pd@NiW/C, 0.0449 $mA \cdot cm^{-2}$ for NiW/C, and 0.67 $mA \cdot cm^{-2}$ for Pd/C (10 wt% Pd) (Fig. 29a). The corresponding mass activities were 31.1 $A \cdot g^{-1}$ (Pd@NiW/C), 0.83 $A \cdot g^{-1}$ (NiW/C), and 12.4 $A \cdot g^{-1}$ (Pd/C), while the Pd-

normalized mass activities reached 311 $A \cdot g^{-1}$ Pd for Pd@NiW/C and 124 $A \cdot g^{-1}$ Pd for Pd/C, confirming the superior intrinsic HOR activity of Pd when supported on NiW/C. For the HER process at –0.1 V vs RHE, the current densities were –2.50 $mA \cdot cm^{-2}$ for Pd@NiW/C, –0.127 $mA \cdot cm^{-2}$ for NiW/C, and –0.567 $mA \cdot cm^{-2}$ for Pd/C (Fig. 29 b). The derived mass activities were 46.3 $A \cdot g^{-1}$ for Pd@NiW/C, 2.35 $A \cdot g^{-1}$ for NiW/C, and 10.5 $A \cdot g^{-1}$ for Pd/C, with Pd-normalized mass activity of 463 $A \cdot g^{-1}$ Pd for Pd@NiW/C, substantially higher than Pd/C.

The Tafel slopes derived from LSV data were 131.87 $mV \cdot dec^{-1}$ for NiW/C, 115.37 $mV \cdot dec^{-1}$ for Pd@NiW/C, and 107.83 $mV \cdot dec^{-1}$ for Pd/C for HOR, while for HER they were 84.20 $mV \cdot dec^{-1}$ for NiW/C, 92.43 $mV \cdot dec^{-1}$ for Pd@NiW/C, and 121.58 $mV \cdot dec^{-1}$ for Pd/C (Fig.30). These values indicate that both HOR and HER proceed via mixed Volmer–Heyrovsky mechanisms, with the rate-determining step influenced by hydrogen adsorption or electrochemical desorption, and that the presence of Pd on NiW/C optimizes the reaction kinetics by modulating the electronic structure and adsorption energies.[12]

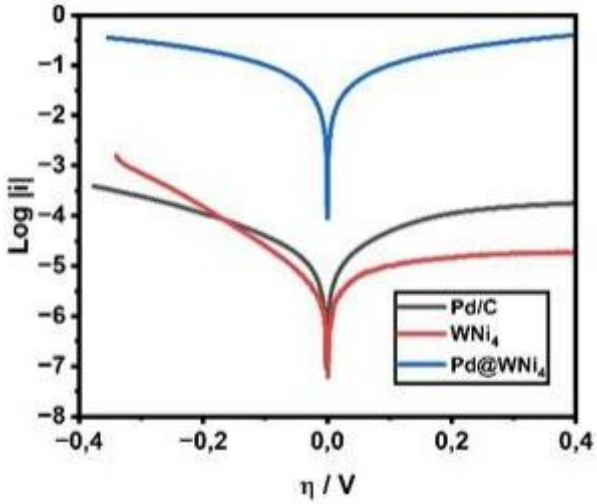

Figura 30: Tafel plot

Electrochemical impedance spectroscopy (EIS) conducted at 0.6 V vs RHE under H_2-saturated 0.1 M KOH at 1600 rpm revealed distinct interfacial characteristics: NiW/C exhibited a single, well-defined semicircle with a charge transfer resistance (Rct) of 37 Ω, followed by a Warburg-type diffusion tail; Pd/C showed an initial semicircle with Rct ≈ 78 Ω, followed by a second, unresolved semicircle extending to ~1000 Ω (Fig. 31a-b). The lower Rct for NiW/C indicates faster electron transfer kinetics, while the Pd@NiW/C system shows improved overall activity compared to Pd/C, demonstrating the synergistic effect of Pd and NiW in enhancing HOR and HER performance.[13] These results align with previous reports on bimetallic and supported catalysts, which highlight the crucial role of electronic interactions and support effects in improving both activity and stability of hydrogen electrocatalysts in alkaline media[14]. For instance, studies have shown that the incorporation of Pd into Ni-based catalysts can significantly enhance electrocatalytic performance due to the synergistic effects between Pd and the support material. Additionally, the optimization of catalyst composition and structure is essential for achieving high efficiency in hydrogen evolution reactions.[16]

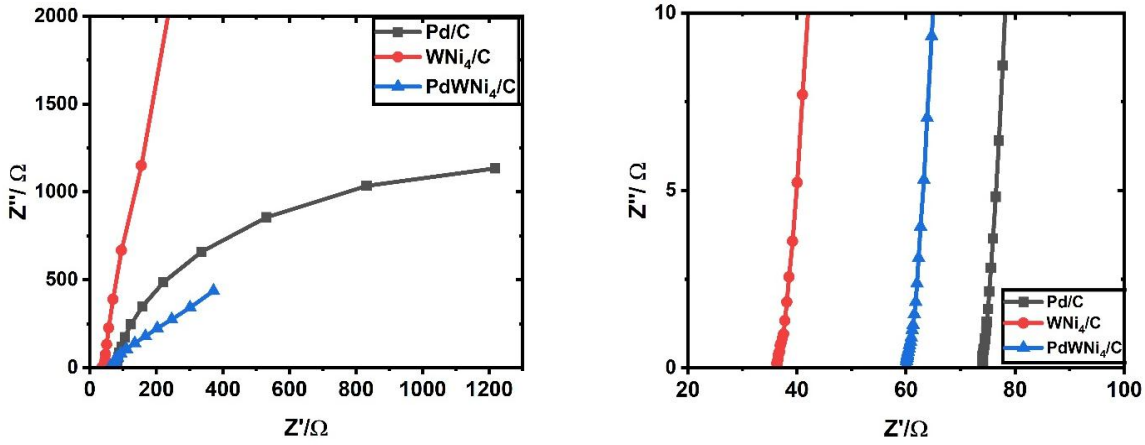

Figura 31: Nyquist plot in saturated N2-KOH 0.1M at 0.6V vs RHE :a) complete frequency scan range b) low frequency semicircles

The $PdNi_4W/C$ catalyst presents an intermediate Rct of 60 Ω; however, it is followed by a second semicircle extending to ~200 Ω and a pronounced vertical Warburg tail reaching ~400 Ω, evidencing complex interfacial processes

involving mixed charge transfer resistance and diffusion phenomena. The presence of multiple semicircles and extended diffusion tails in $PdNi_4W/C$ suggest synergistic interactions between Pd nanoparticles and the Ni_4W alloy support, which modulate surface adsorption properties and reaction intermediates, thereby impacting both electron transfer and mass transport steps. These results demonstrate that despite a moderately higher charge transfer resistance relative to Ni_4W/C, $PdNi_4W/C$ achieves superior HOR performance due to optimized catalytic sites and enhanced kinetics arising from the Pd–NiW interface, underscoring the multifaceted nature of electrocatalytic activity beyond simple resistance metrics.[17]

5.7 Conclusions

The electrochemical characterization of the synthesized catalysts unequivocally demonstrates the beneficial role of Pd incorporation on the Ni–W alloy support toward enhancing hydrogen electrocatalysis in alkaline environments. The Pd@NiW/C catalyst exhibited markedly superior HOR and HER activities compared to both NiW/C and Pd/C, despite its significantly reduced PGM loading (Pd: 0.0011 mg·cm^{-2}). At 0.1 V vs RHE, the HOR current density reached 1.68 mA·cm^{-2} for Pd@NiW/C, substantially higher than that of NiW/C (0.0449 mA·cm^{-2}) and Pd/C (0.67 mA·cm^{-2}). The corresponding mass activity of 31.1 A·g^{-1} for Pd@NiW/C—translating to a Pd-normalized value of 311 A·g^{-1} Pd—represents a more than 2.5-fold improvement relative to Pd/C (124 A·g^{-1} Pd).

For the HER process, Pd@NiW/C delivered a current density of –2.50 mA·cm^{-2} at –0.1 V vs RHE, compared to –0.127 mA·cm^{-2} and –0.567 mA·cm^{-2} for NiW/C and Pd/C, respectively. The derived mass activity of 46.3 A·g^{-1} (or 463 A·g^{-1} Pd) further confirms the pronounced catalytic enhancement afforded by Pd–NiW interfacial synergy. Analysis of the Tafel slopes revealed values of 115.37 mV·dec^{-1} (HOR) and 92.43 mV·dec^{-1} (HER) for Pd@NiW/C, consistent with a mixed Volmer–Heyrovsky mechanism in which the rate-determining step is governed by hydrogen adsorption/desorption kinetics.

Electrochemical impedance spectroscopy (EIS) provided additional insight into

the interfacial behavior of the catalysts. The Pd@NiW/C electrode exhibited a charge transfer resistance (Rct) of 60 Ω, intermediate between that of NiW/C (37 Ω) and Pd/C (78 Ω), accompanied by a distinct Warburg-type diffusion feature. This indicates that while Pd incorporation slightly increases the interfacial resistance due to modified surface energetics, it concurrently facilitates more favorable charge and mass transport processes, resulting in a net improvement in overall electrocatalytic performance.

These results collectively confirm that the formation of a Pd–NiW interface induces beneficial electronic and structural modifications that optimize hydrogen binding energy and enhance electron transfer efficiency. The Ni–W alloy acts as a corrosion-resistant, electronically tunable substrate that stabilizes Pd nanoparticles and promotes synergistic adsorption dynamics. The outstanding activity of Pd@NiW/C, together with its low PGM content and enhanced kinetic parameters, highlights the effectiveness of alloy–support engineering as a strategy to overcome the intrinsic sluggishness of the hydrogen oxidation reaction in alkaline media. Consequently, the Pd@NiW/C system represents a promising, cost-effective anode catalyst for hydroxide exchange membrane fuel cells, combining high activity, durability, and reduced reliance on precious metals.

5.8 References

1. X. Tian et al., "Metal-support interaction boosts the stability of Ni-based electrocatalysts for alkaline hydrogen oxidation," Nat Commun, vol. 15, no. 1, Dec. 2024, doi: 10.1038/s41467-023-44320-w.

2. B. Zhang, X. Qiu, T. Chen, C. Huang, X. Yue, and S. Huang, "Construction of Heterostructure between Ni17W3 and WO2 to Boost the Hydrogen Oxidation Reaction in Alkaline Medium," ACS Appl Mater Interfaces, vol. 16, no. 3, pp. 3270–3278, Jan. 2024, doi: 10.1021/acsami.3c13952.

3. H. I. S. Nogueira, A. M. V. Cavaleiro, J. Rocha, T. Trindade, and J. D. P. De Jesus, "Synthesis and characterization of tungsten trioxide powders prepared from tungstic acids," Mater Res Bull, vol. 39, no. 4–5, pp. 683–693, 2004, doi: 10.1016/j.materresbull.2003.11.004.

4. X. L. Yang, W. L. Dai, R. Gao, and K. Fan, "Characterization and catalytic behavior of highly active tungsten-doped SBA-15 catalyst in the synthesis of glutaraldehyde using an anhydrous approach," J Catal, vol. 249, no. 2, pp. 278–288, 2007, doi: 10.1016/j.jcat.2007.05.002.

5. H. Lu et al., "Synthesis of hexagonal ultrathin tungsten oxide nanowires with diameters below 5 nm for enhanced photocatalytic performance," Superlattices Microstruct, vol. 116, pp. 17–26, Apr. 2018, doi: 10.1016/j.spmi.2018.01.032.

6. L. Niu et al., "Simple synthesis of amorphous NiWO4 nanostructure and its application as a novel cathode material for asymmetric supercapacitors," ACS Appl Mater Interfaces, vol. 5, no. 16, pp. 8044–

8052, Aug. 2013, doi: 10.1021/am402127u.

7. Y. H. Wang et al., "Unraveling Stoichiometry Effect in Nickel-Tungsten Alloys for Efficient Hydrogen Oxidation Catalysis in Alkaline Electrolytes," Angewandte Chemie - International Edition, vol. 63, no. 32, Aug. 2024, doi: 10.1002/anie.202407613.

8. C. Huang et al., "In Situ Construction of Ni/Ni0.2Mo0.8N Heterostructure to Enhance the Alkaline Hydrogen Oxidation Reaction by Balancing the Binding of Intermediates," Adv Funct Mater, vol. 33, no. 34, Aug. 2023, doi: 10.1002/adfm.202300593.

9. S. Qin et al., "Ternary nickel–tungsten–copper alloy rivals platinum for catalyzing alkaline hydrogen oxidation," Nature Communications , vol. 12, no. 1, Dec. 2021, doi: 10.1038/s41467-021-22996-2.

10. Y. Duan et al., "Bimetallic nickel-molybdenum/tungsten nanoalloys for high-efficiency hydrogen oxidation catalysis in alkaline electrolytes," Nature Communications , vol. 11, no. 1, Dec. 2020, doi: 10.1038/s41467-020-18585-4.

11. B. Xiong, W. Zhao, H. Tian, W. Huang, L. Chen, and J. Shi, "Nickel-Tungsten Nano-Alloying for High-Performance hydrogen Electro-Catalytic oxidation," Chemical Engineering Journal, vol. 432, Mar. 2022, doi: 10.1016/j.cej.2021.134189.

12. Mu, X., et al. "Alkaline Hydrogen Oxidation Reaction Catalysts: Insight and Opportunities." *Small Structures*, vol. 4, no. 5, 2023, p. 2200281. Wiley-VCH.
13. Guo, Z., et al. "Understanding the Strain Effect in Alkaline Hydrogen

Oxidation Reaction." *Chemical Science*, vol. 16, no. 4, 2025, pp. 2314–2325. Royal Society of Chemistry.

14. Akamine, Y., et al. "The Impact of Metal–Support Interaction on the Structure and Activity of Ni Nanoparticles in Alkaline Hydrogen Oxidation." *ACS Applied Energy Materials*, vol. 7, no. 12, 2024, pp. 10521–10533.

15. Yang, F., et al. "Review: Alkaline Hydrogen Oxidation Reaction on Ni-Based Non-Precious Electrocatalysts." *Coordination Chemistry Reviews*, vol. 489, 2023, p. 215153.

16. Ipadeola, A. K., et al. "Pd/Ni Synergetic Activity for Hydrogen Oxidation Reaction in Alkaline Conditions." *Electrochimica Acta*, vol. 176, 2015, pp. 346–355.

17. [17] Zhang, Y., et al. "Engineering Bimetallic Interfaces for Efficient Hydrogen Evolution and Oxidation in Alkaline Media." *Nature Communications*, vol. 15, no. 1, 2024, article 44320.

6. Advanced Mixed Metal Oxide Nanostructures for Anion Exchange Membranes Water Electrolysis

6.1 Introduction

The transition to a low-carbon energy economy demands efficient and scalable technologies for green hydrogen production.[1,2] Among the available methods, water electrolysis powered by renewable energy stands out as a clean and sustainable route.[3,4,5] Anion exchange membrane water electrolysis (AEMWE) has gained considerable interest due to its potential to combine the advantages of both proton exchange membrane (PEM) and alkaline systems—namely, high efficiency, lower cost, and the possibility to use non-precious metal catalysts.[3] One of the key challenges in AEMWE remains the development of high-performance electrocatalysts for the hydrogen evolution reaction (HER) that are stable under alkaline conditions and composed of earth-abundant elements.[6,7]

In this regard, mixed metal oxides, and especially molybdenum-based compounds, have emerged as promising candidates due to their tunable electronic properties, structural versatility, and known activity for HER.[8,9] Recent studies have focused on the design of composite systems where MoO_3 is combined with other transition metal oxides to promote electron conductivity, increase the density of active sites, and improve overall catalytic performance[10,11].

A particularly innovative strategy involves the synthesis of MoO_{3-x}/$NiMoO_4$ nanorods starting from NiO nanoparticles[12]. This approach enables precise control over both composition and nanostructure. The use of NiO as a precursor not only facilitates the formation of nickel molybdate phases but also plays a role in inducing oxygen vacancies within the MoO_3 lattice during thermal treatment[13]. These vacancies are known to enhance catalytic activity by improving charge transfer kinetics and modifying the local electronic environment of active sites.[13,14]

The resulting MoO_{3-x}/$NiMoO_4$ nanorods exhibit a one-dimensional morphology that favors rapid electron transport and efficient electrolyte access.[14,15] Moreover, the intimate interface between the two oxide phases creates synergistic effects that go beyond the simple sum of the individual components.[15,16] These include enhanced stability under operating conditions, improved hydrogen adsorption properties, and better integration within membrane electrode assemblies (MEAs)[17,18].

This chapter provides a detailed discussion of the synthesis methodology, structural characterization, and electrochemical performance of these nanostructured catalysts, placing them in the broader context of HER catalyst development for AEM systems. The insights gained from this work contribute to the growing understanding of how nanoscale engineering and defect chemistry can be leveraged to design next-generation materials for green hydrogen technologies.

6.2 Synthesis of MoO_{3-x}/$NiMoO_4$

The synthesis of MoO_{3-x}/$NiMoO_4$ nanostructures relies on a multi-step procedure designed to achieve both compositional control and nanoscale morphological definition. The process begins with the preparation of a physical mixture of commercial molybdenum trioxide (MoO_3) and nickel oxide (NiO) nanoparticles[19,20], typically in a molar ratio optimized to favor the formation of mixed oxide[21,22,23] phases during subsequent thermal processing.[24] The NiO nanoparticles play a dual role in this context: they not only serve as a source of nickel ions for the formation of nickel molybdate but also act as a structural and chemical modifier that influences the defect chemistry of the final material. After homogenization—often facilitated by ball milling or ultrasonication in an appropriate solvent—the precursor mixture is subjected to a controlled thermal treatment in a reducing or inert atmosphere[25]. This calcination step is critical, as it induces solid-state reactions between MoO_3 and NiO, leading to the in situ formation of $NiMoO_4$ while simultaneously creating oxygen-deficient MoO_{3-x} domains. The oxygen vacancies arise because of partial reduction of Mo^{6+} species and are known to enhance the electrical conductivity and catalytic

behavior of the resulting composite[25].

The thermal treatment parameters, such as temperature, duration, and atmospheric composition, are carefully tuned to promote the growth of one-dimensional nanorods while avoiding unwanted phase segregation or particle sintering. Nanorods morphology is particularly advantageous, as it contributes to an increased surface area and facilitates both electron mobility and ion transport during electrocatalysis. Notably, the coexistence of MoO_{3-x} and $NiMoO_4$ within a single nanostructure leads to a high degree of interfacial contact between the two phases, a feature believed to play a key role in the observed electrocatalytic synergy[23,24].

Overall, this synthetic approach offers a relatively simple and scalable route to obtain complex oxide nanomaterials with finely tuned properties, making it highly relevant for practical implementation in anion exchange membrane electrolyzer systems[22].

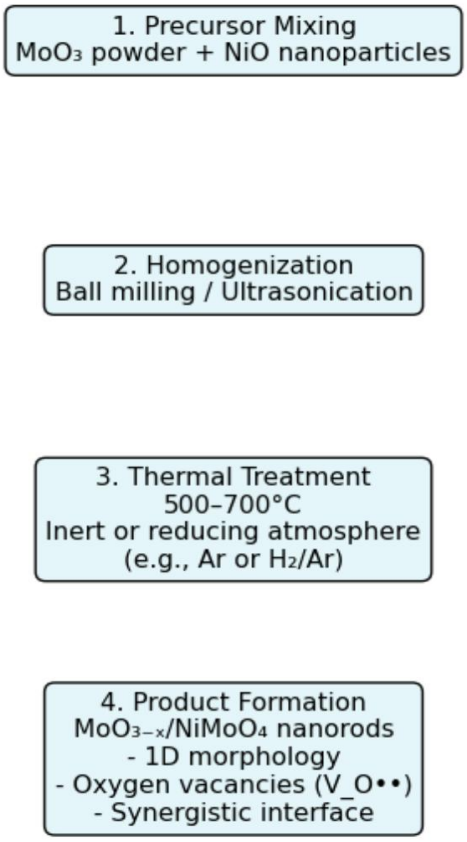

Figure 32: Synthesis of NiMox

6.3 Physical Characterization

The comprehensive physical characterization of the $MoO_{3-x}/NiMoO_4$ nanorods elucidates their complex structural and chemical features, which are crucial for their enhanced electrocatalytic performance. X-ray diffraction (XRD) analysis reveals the coexistence of two distinct crystalline phases: orthorhombic molybdenum oxide with oxygen deficiencies and monoclinic nickel molybdate.
In Figure 31,the diffraction peaks observed at approximately 12.7°, 23.4°, 25.7°, 27.4°, 34.4°, and 39.6° (2θ) can be indexed to the (020), (110), (021), (111), (040), and (002) planes of orthorhombic MoO_3, respectively, confirming the presence of a well-defined crystal lattice[26]. However, these peaks exhibit noticeable broadening, indicative of nanoscale crystallite dimensions and possible lattice strain induced by oxygen vacancy formation. In parallel, reflections at around 18.2°, 30.1°, 35.8°, 38.7°, and 52.2° correspond to the (110), (−112), (111), (202), and (−114) planes of monoclinic $NiMoO_4$, substantiating the successful incorporation of nickel species into the oxide framework and formation of the nickel molybdate phase[27]. The slight shift of MoO_3 peaks toward lower angles suggests lattice expansion caused by oxygen vacancies, which alter the local atomic arrangement and have been linked to improved electrical conductivity and catalytic sites.[28] The absence of residual NiO peaks supports the efficient conversion of the nickel oxide precursor into $NiMoO_4$ during the thermal treatment, ensuring phase purity and homogeneity.

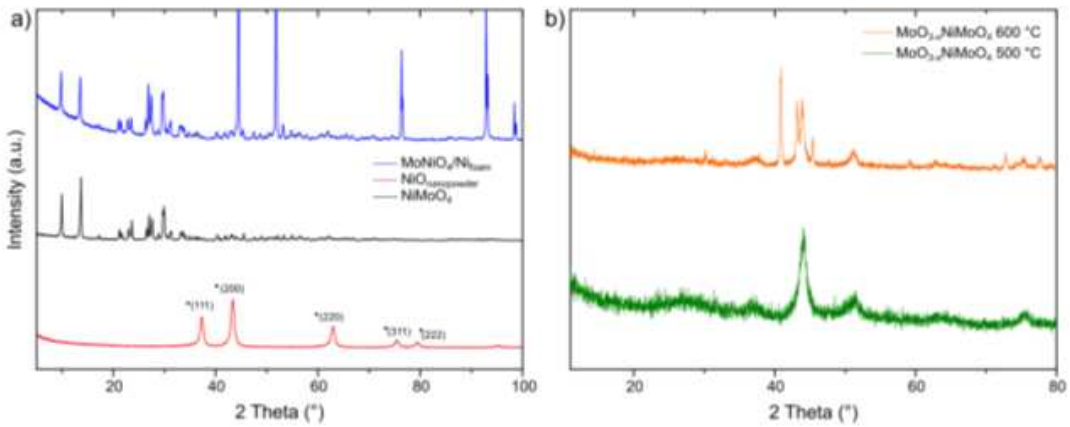

Figure32: X Ray diffraction: (a) precursors and $NiMoO_4$ (b) thermal treated samples

Morphological insights provided in figure 33 by scanning electron microscopy (SEM) demonstrate that the product is composed of uniform nanorods with high aspect ratios, which enhance surface area and facilitate efficient electron transport pathways critical for electrocatalysis. Transmission electron microscopy (TEM) complements these findings by resolving the internal structure at higher resolution (Figure34-a), where clear lattice fringes corresponding to both MoO_{3-x} and $NiMoO_4$ phases are visible, confirming the coexistence and close spatial proximity of these two components. This intimate interface is essential for synergistic effects that boost catalytic activity. Additionally, high-resolution TEM images reveal the presence of structural defects such as oxygen vacancies and dislocations, which create active sites and improve charge carrier mobility within the nanorods.

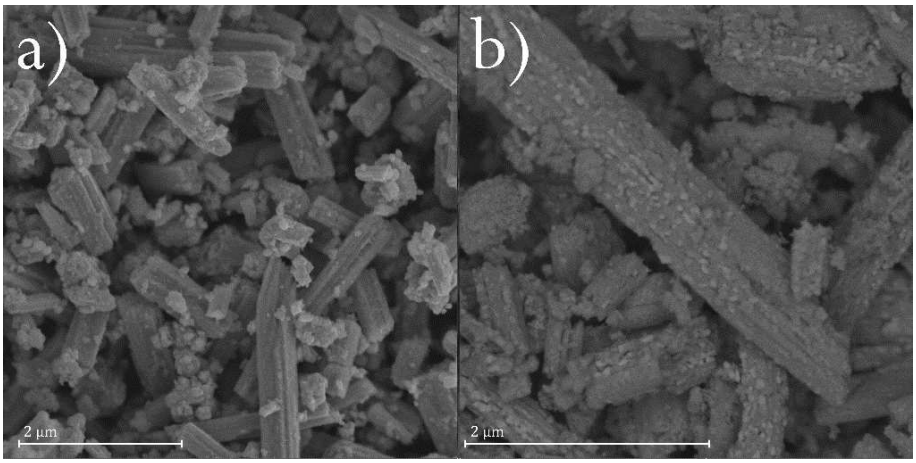

Figure 33: SEM images of a) MoO3-xNiMoO4 500°C and b) MoO3-xNiMoO4 600°C.

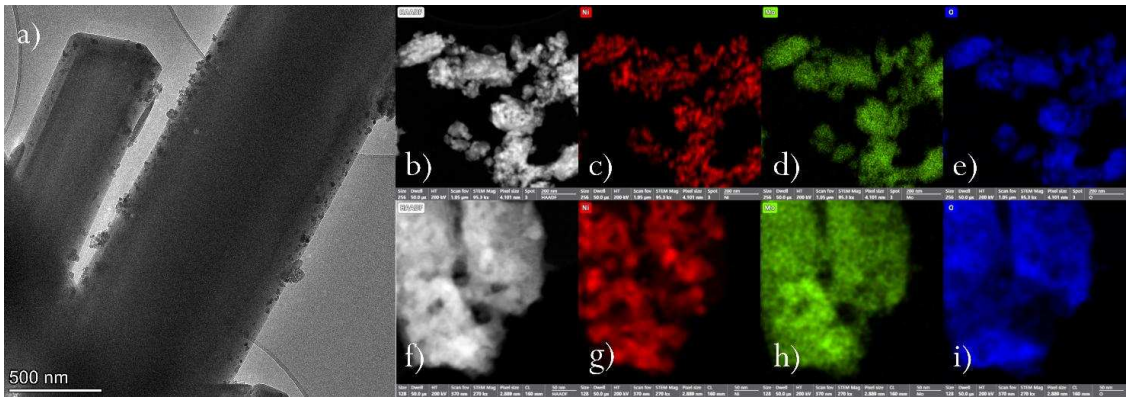

Figure 34: a) TEM image of precursor NiMoO4. b-e) STEM images and elemental mapping of MoO3-xNiMoO4 500°C, and f-i) STEM images and elemental mapping of MoO3-xNiMoO4 600 °C.

X-ray photoelectron spectroscopy (XPS) offers a detailed view of the surface chemical states, shedding light on the oxidation states and defect chemistry that are pivotal for catalytic behavior. The Mo 3d spectra (Figure 35-a) exhibit two sets of spin-orbit doublets: the dominant pair centered around 232.5 eV (Mo $3d_5/_2$) and 235.6 eV (Mo $3d_3/_2$) corresponds to hexavalent molybdenum (Mo^{6+}), while a secondary doublet at lower binding energies (~231.2 eV and ~234.3 eV) indicates the presence of pentavalent molybdenum (Mo^{5+}), consistent with partial reduction caused by oxygen vacancy formation[29]. The Ni 2p spectrum (Figure 35-b) displays characteristic peaks at approximately 855.7 eV (Ni $2p_3/_2$) and 873.3 eV (Ni $2p_1/_2$), accompanied by satellite features typical of Ni^{2+} ions in an octahedral coordination environment, which aligns with the $NiMoO_4$ crystal structure[29]. The O 1s region further corroborates the defect chemistry: a main peak near 530.2 eV is attributed to lattice oxygen, whereas a higher binding energy shoulder at approximately 531.5–532.0 eV corresponds to surface hydroxyl groups and oxygen vacancies. The enhanced intensity of this component relative to pristine MoO_3 confirms an increased concentration of oxygen defects, which are well-known to facilitate electron transfer processes and create more catalytically active sites. Together, these complementary characterization techniques (Figure 35,a-b-c-d-e-f) provide a comprehensive picture of the $MoO_{3-x}/NiMoO_4$ nanorods as a hybrid material

featuring a composite crystalline architecture with significant oxygen vacancy concentrations and well-integrated phase interfaces[20,25]. These structural and chemical attributes are fundamental to their superior performance in the hydrogen evolution reaction under alkaline conditions.

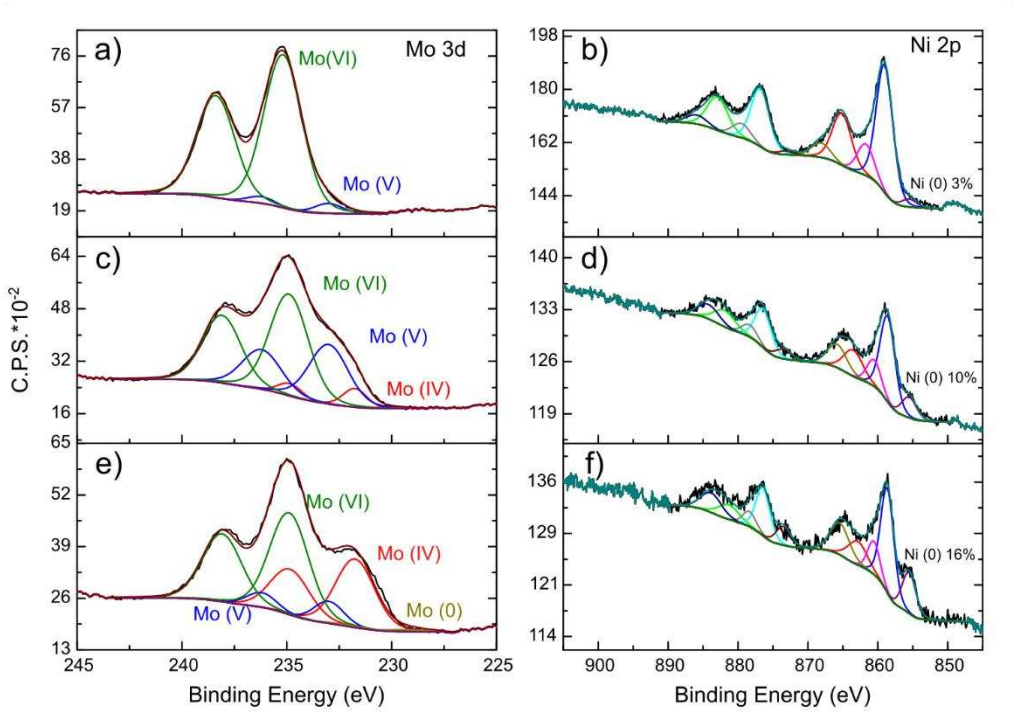

Figure 35: XPS spectra of Mo and Ni for a-b) NiMoO4 precursor, c-d) MoO3-xNiMoO4 500 °C, e-f) MoO3-xNiMoO4 600 °C.

6.3.1. In situ Raman Spectroscopy

Raman spectroscopy was employed both *in situ* and *ex situ* to thoroughly investigate the structural evolution of $NiMoO_4$-based catalysts during thermal treatment and hydrogen reduction. The *ex situ* Raman spectrum recorded at room temperature (Figure 36-a) displayed distinct vibrational modes characteristic of the hydrated nickel molybdate phase ($NiMoO_4 \cdot nH_2O$), particularly intense peaks corresponding to molybdenum-oxygen tetrahedral coordination[30]. Notably, the absence of Raman bands around 700 cm^{-1}—typically associated with the α-phase featuring octahedral molybdenum coordination—indicated that the precursor material was predominantly in the hydrated form. As the sample was heated, temperature-dependent spectra

(Figure 36-b) revealed clear changes: the disappearance of a mode at 871 cm^{-1}

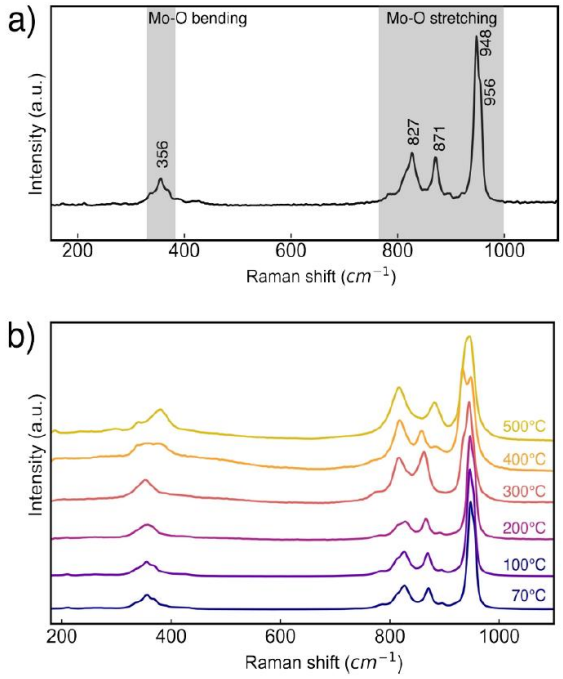

Figure 36: a) Room temperature Raman spectrum of the NiMoO4 precursor. b) Spectra of the NiMoO4 precursor as a function of temperature.

and the emergence of a new peak near 881 cm^{-1} signaled the phase transformation to the thermally stable β-$NiMoO_4$ polymorph[31]. Additionally, the shift of the Mo–O bending vibration from 356 cm^{-1} to 380 cm^{-1} supported a modification in the local coordination environment. The absence of any α-phase signatures throughout this thermal ramp confirmed the preferential stabilization of β-$NiMoO_4$ under these synthesis conditions. During in situ Raman measurements under reducing atmosphere at 630 °C (Figure 37a), a rapid decrease in the intensity of $NiMoO_4$ precursor peaks was observed after approximately 20 minutes, indicating a swift surface reduction and structural rearrangement rather than a gradual formation of oxygen-deficient sub-stoichiometric phases[31]. This rapid transition is evident from the normalized intensity plot of $NiMoO_4$ stretching modes (Figure 37b), which shows a sharp decline, while the position of these modes remains constant (Figure 37c), suggesting a phase change rather than bond length expansion typically caused by oxygen vacancies[32]. The visible darkening of the sample surface, which

reduced laser penetration depth, further supported this interpretation.

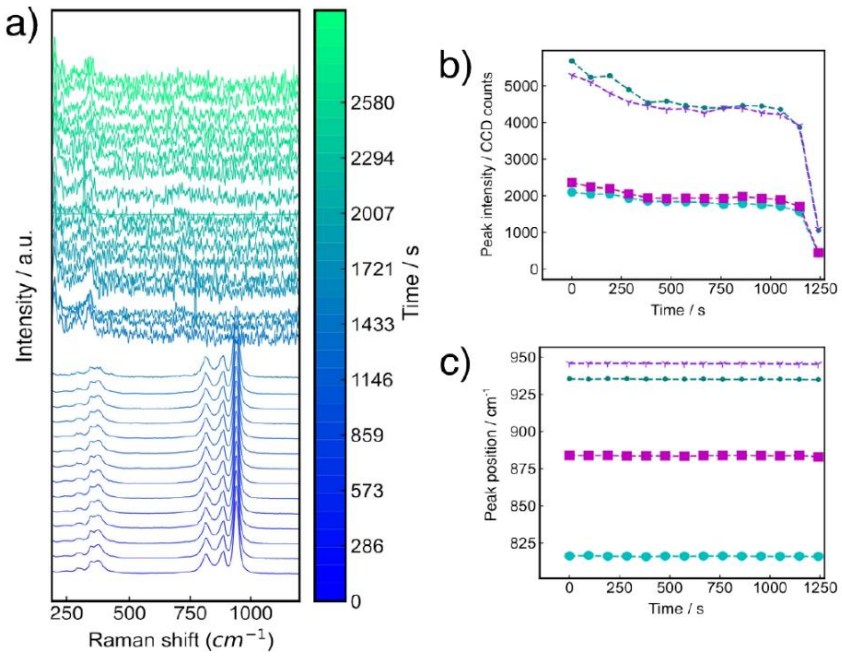

Figure 37:1a) In situ Raman spectroscopy of the reduction of NiMoO4

Raman spectra of catalysts reduced at 500 °C and 600 °C (Figure 38) showed residual $NiMoO_4$ features above 850 cm^{-1}, indicating incomplete reduction of the precursor phase. Alongside these, weaker vibrational modes appeared at approximately 189, 340, 714, and 815 cm^{-1}, which are characteristic of MoO_{3-x} suboxides, intermediate phases between MoO_3 and MoO_2[33]. The prominent mode near 814 cm^{-1} corresponds specifically to MoO_3, confirming that Mo remains partially in the +6 oxidation state[33]. The presence of these suboxide phases indicates partial reduction to lower oxidation states and suggests a heterogeneous catalyst surface composed of mixed oxidation states[34,35]. These Raman observations correlate well with XPS measurements, which also revealed the coexistence of multiple molybdenum oxidation states, confirming the complex and dynamic nature of the catalyst surface after thermal and reductive treatments.[36]

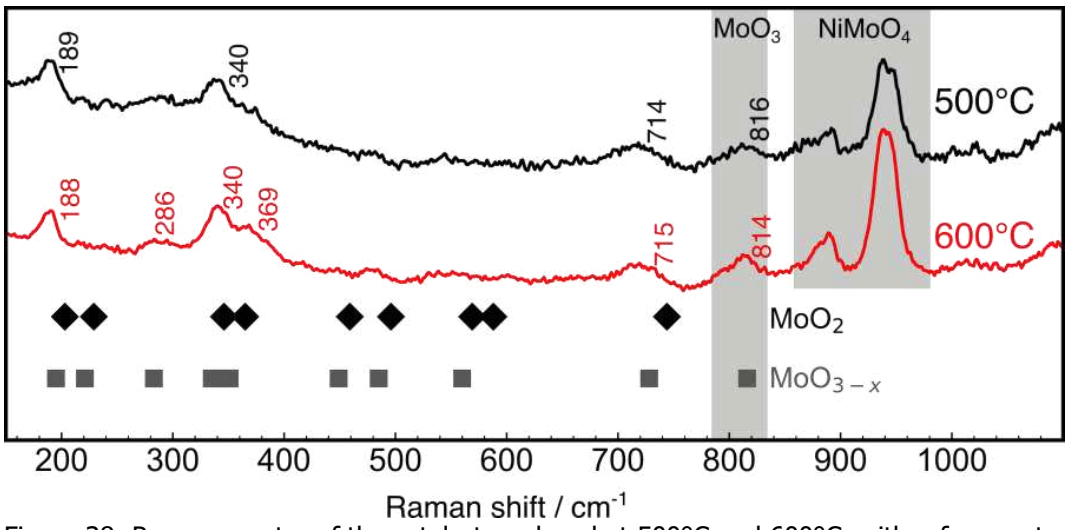

Figure 38: Raman spectra of the catalysts reduced at 500°C and 600°C, with reference to MoO2 and $MoO3_{-x}$

These structural insights are critical for understanding and optimizing the catalyst's hydrogen evolution performance. The transition from hydrated $NiMoO_4 \cdot nH_2O$ to β-$NiMoO_4$ ensures a stable crystalline framework, essential for maintaining catalyst integrity during operation[34]. The coexistence of MoO_{3-x} suboxides along with residual $NiMoO_4$ suggests an ideal balance between oxidized and reduced species that can enhance electronic conductivity and increase the density of catalytically active sites, thereby boosting activity. Furthermore, the retention of higher oxidation states likely contributes to improved stability by minimizing sintering or phase segregation. Collectively, the Raman and XPS data underscore the importance of carefully controlled thermal and reductive processing to tailor catalyst structure and maximize electrocatalytic efficiency.[36]

6.4 Electrochemical characterization

6.4.1. Half-cell measurements

The evaluation of catalytic activity for the hydrogen evolution reaction (HER) in half-cell configurations represents a fundamental step in the characterization of electrocatalysts. In this study, $MoO_{3-x}NiMoO_4$ catalysts synthesized at annealing temperatures of 500 °C and 600 °C were investigated to elucidate the influence of thermal treatment on their electrochemical performance. As a benchmark, commercial Pt (40%)/C was also tested under identical conditions to provide a reference for catalytic efficiency.

Electrochemical measurements were conducted using a standard three-electrode setup, with the catalyst-coated glassy carbon electrode as the working electrode, a platinum wire as the counter electrode, and a reversible hydrogen electrode (RHE) as the reference. The electrolyte consisted of an alkaline solution (1 M KOH) to mimic the operational environment of alkaline water electrolysis cells. To ensure reproducibility and control of mass transport effects, linear sweep voltammetry (LSV) was performed at a scan rate of 1 mV s^{-1} with the electrode rotating at 1600 rpm.

The LSV results (Fig. 39-a) demonstrate a clear improvement in catalytic activity for the $MoO_{3-x}NiMoO_4$ sample annealed at 600 °C compared to the 500 °C counterpart.[40,41] This is reflected by the increased current density at given overpotentials, as well as by the reduced overpotential required to achieve benchmark current densities such as -10 mA cm^{-2}. Table 5 quantitatively summarizes these enhancements, highlighting superior mass and specific activities for the higher temperature sample. These performance gains can be attributed primarily to morphological and compositional changes induced by thermal treatment. Electrochemical double-layer capacitance (Cdl) measurements were employed to estimate the electrochemically active surface area (ECSA), a critical parameter correlating surface structure

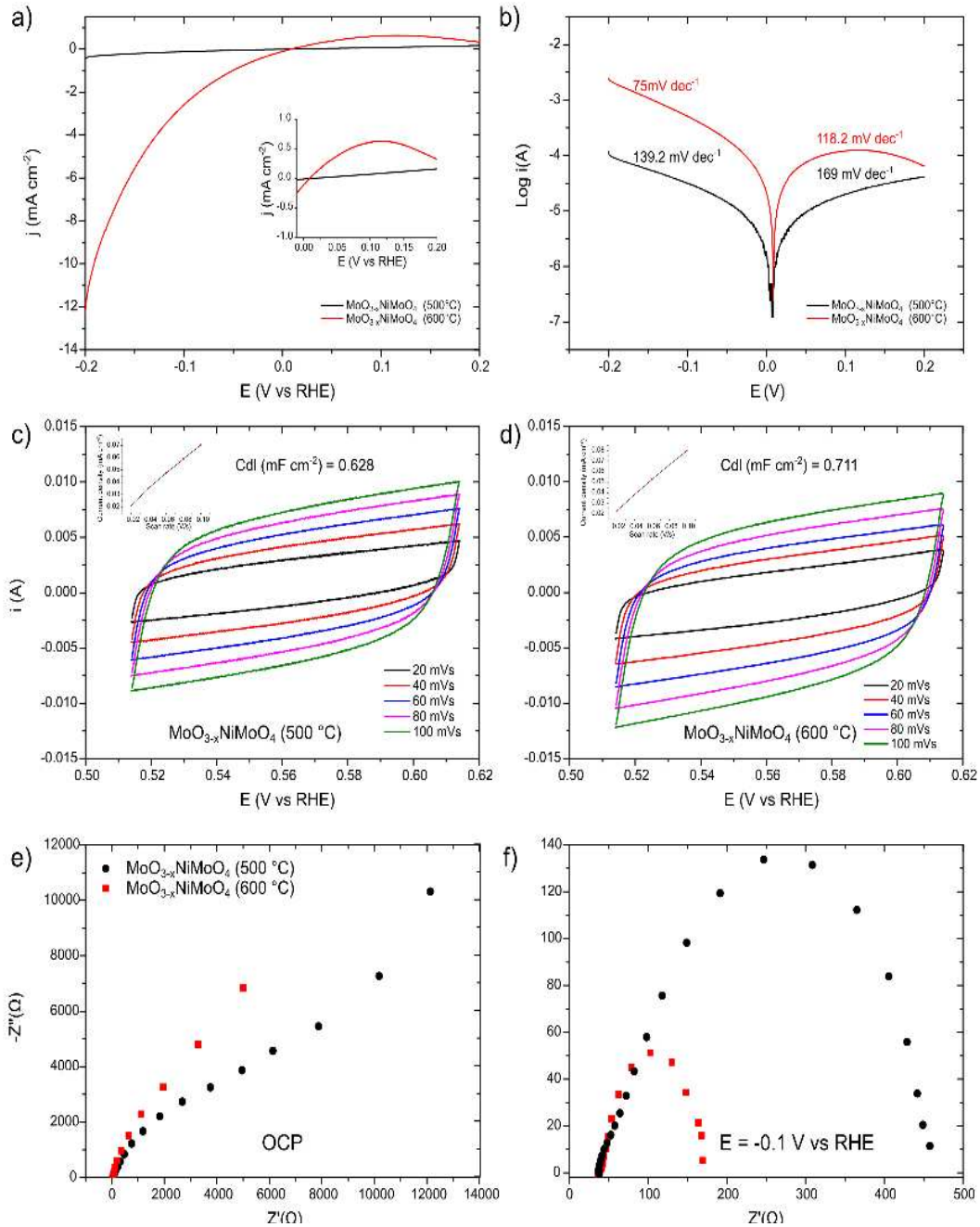

Figure 39: LSVs from HER to HOR region of MoO3-xNiMoO4 500 and 600 °C, 1 mV s-1 at 1600 rpm rotating disk. Inset shows the comparison in the HOR region. b) Tafel plots with relative Tafel slope for HER and HOR. Cdl measurement for c) MoO3-xNiMoO4 500 °C and d) MoO3-xNiMoO4 600C. CVs recorded in the potential windows of 0.514-0.614V vs RHE with no faradaic processes. Cdl (capacitance double layter) measurements were obtained by the slope of the capacitive current determined at 0.56V as a function of scan rate (see insets). Nyquist plot obtained from impedance measurments at open circuit value e), and f) in HER region at -0.1V vs RHE.

with catalytic activity. Cyclic voltammetry scans were recorded in a non-faradaic potential range (0.514–0.614 V vs RHE), where no redox processes occur, allowing the current response to be dominated by capacitive charging (Fig. 39 c-d). The slope of the capacitive current at 0.56 V plotted against scan rate provided the Cdl values, which increased from 0.63 mF cm^{-2} for the 500 °C sample to 0.71 mF cm^{-2} for the 600 °C sample. This increment suggests that annealing at the higher temperature enhances surface roughness or porosity, as corroborated by SEM images (Figure 33), which reveal more pronounced surface features consistent with increased catalyst dispersion and accessible active sites.

Further insights were gained from surface chemistry characterization via X-ray photoelectron spectroscopy (XPS) and transmission electron microscopy (TEM). XPS data (Fig. 10) confirmed an enrichment of molybdenum species at the surface, with a higher fraction of Mo(IV) oxidation states present in the sample annealed at 600 °C. TEM micrographs (Fig. 34) corroborate the uniform distribution of oxide species, indicating that the catalyst maintains structural homogeneity upon heat treatment. The absence of signals corresponding to metallic Mo(0) in XPS spectra excludes the presence of NiMo alloys, which are often reported as active phases in similar systems but typically require more aggressive reducing conditions or higher temperatures for formation (Figure35). This observation aligns with prior literature indicating the difficulty of reducing molybdenum below 600 °C under these [41,42].

The enhancement in HER catalytic activity observed cannot be simply ascribed to compositional changes but is also intimately related to the interplay of the catalyst's microstructure and interfacial properties. The phase separation of oxygen-deficient MoO_{3-x} towards the catalyst surface during annealing at 600 °C is hypothesized to create active sites with favorable electronic structures that promote HER kinetics . Additionally, the coexistence of Ni and NiO phases at the interface appears to facilitate the Volmer–Heyrovsky or Volmer–Tafel reaction pathways, thereby lowering energy barriers for hydrogen evolution[43].

Kinetic parameters extracted from Tafel analysis (Fig. 39b) provide a more

quantitative comparison between samples. The Tafel slope of the 600 °C annealed sample is significantly lower than that of the 500 °C counterpart, indicating faster reaction kinetics and more efficient charge transfer. The exchange current density, which represents the intrinsic catalytic activity at zero overpotential, was also higher for the 600 °C catalyst (3.24 A g/Metal^{-1}). This directly reflects the improved catalytic performance, highlighting the beneficial effect of increased annealing temperature on the active sites' availability and reactivity.

Electrochemical impedance spectroscopy (EIS) further elucidated the charge transfer and mass transport phenomena occurring at the electrode/electrolyte interface. Nyquist plots recorded both at open circuit potential (OCP) and under HER conditions (−0.1 V vs RHE) reveal a significant reduction in charge transfer resistance (Rct) for the 600 °C sample, dropping from 420 Ω for the 500 °C sample to 134 Ω (Fig. 39e-f). The high-frequency semicircle observed remained largely unaffected by changes in overpotential, suggesting that it corresponds to processes other than the catalytic reaction kinetics, such as electrode porosity or electrical contact resistances[44,45]. In contrast, the low-frequency semicircle, which varied with applied potential, is assigned to the charge transfer step directly related to HER activity. The reduction in Rct at more negative potential indicates enhanced electron transfer and catalytic turnover, consistent with the polarization curves.

	Specific activity |[mA cm^{-2}]| @η = 0.1 V		Mass activity |[A g_{Metal}^{-1}]| @η = 0.1 V		Exchange current [A g_{Metal}^{-1}]	Tafel slope [mV dec^{-1}]	
	HOR	HER	HOR	HER		HOR	HER
$MoO_{3-x}NiMoO_4$ 500 °C	0.07	0.11	0.48	0.76	0.30	169	139.2
$MoO_{3-x}NiMoO_4$ 600 °C	0.61	2.60	4.16	17.64	3.24	118.2	75
Pt(40%)/C	3.11	25.8	32.88	272.32	16.45	74.6	43.1

Table 5: Parameter obtained from LSV

Complementing these findings, comparison of HER activity with similar catalysts prepared on nickel foam substrates demonstrated that using NiO as a seed layer improves specific activity, with a marked increase in current density at −0.1 V vs RHE. This is likely due to better catalyst integration and increased active surface area, underlining the importance of substrate selection and catalyst morphology control in electrocatalyst design.

Collectively, these half-cell measurements provide a comprehensive picture of how annealing temperature and synthesis strategy modulate the catalytic behavior of $MoO_{3-x}NiMoO_4$ materials. Higher temperature treatment results in a catalyst with increased surface roughness, optimized phase distribution, and improved electronic properties, leading to superior HER performance. These results not only validate the material's potential for alkaline water electrolysis applications but also emphasize the critical role of fine-tuning structural and interfacial properties in the development of efficient non-precious metal electrocatalysts.

6.4.2. AEM Water Electrolysis cell testing

To assess the practical applicability of the $MoO_{3-x}NiMoO_4$ electrocatalyst in a device-relevant context, a lab-scale anion exchange membrane (AEM) water electrolyzer was assembled, employing the catalyst synthesized at 600 °C as the cathode and a nickel foam as the anode. The system was evaluated via polarization measurements conducted at 60 °C, with a voltage sweep from 0 to 2 V at a scan rate of 10 mV s^{-1}. As shown in Fig. 13a, the cell exhibited a current density of 820 mA cm^{-2} at 2 V, significantly outperforming the previously reported MoO_2/Ni foam cathode under identical conditions, which reached only 517 mA cm^{-2}. This improvement highlights the superior activity of the powder-based catalyst, particularly in terms of its specific mass activity and interfacial effectiveness. The enhanced performance is attributed to the increased number of accessible active sites, better surface coverage, and more intimate contact between the catalyst particles and the membrane interface, which collectively reduce interfacial resistances and improve charge transport kinetics.

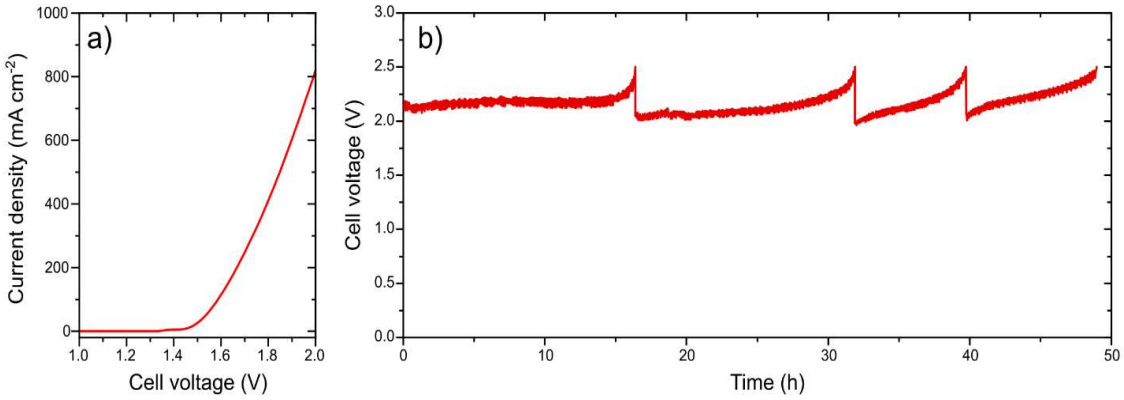

Figure 40:Typical polarization curve for AEM Electrolyzers cell at 60°C, b) cell voltage monitored at 1 A cm2. AEMWE with MoO3-xNiMo=4 600C cathode and Ni foam anode with Fumatech FAA-3-PK-130 AEM

In addition to the initial activity assessment, long-term operational stability was evaluated through chronoamperometric testing at a fixed current density of 1 A cm^{-2} over a 50-hour period. The corresponding voltage profile, shown in Fig. 40a-b, reveals excellent stability, with the cell voltage remaining consistently close to 2.2 V. Minor oscillations in the voltage were observed, correlating with periodic replacement of the KOH electrolyte, but no signs of performance degradation or catalyst deactivation were detected. The estimated energy consumption of 57.7 kWh per kilogram of hydrogen produced is competitive for non-precious metal-based systems and confirms the material's suitability for practical electrolytic hydrogen production. Comparatively, a MoO_2/Ni foam cathode tested under similar conditions maintained stable operation at 1.85 V, but only at 0.5 A cm^{-2}, demonstrating the benefit of employing a powder-based morphology for enhanced catalyst layer utilization. Overall, these results validate the catalytic efficiency and durability of $MoO_{3-x}NiMoO_4$ in a full-cell AEM electrolysis setup. The performance gains observed are closely linked to the rational design of the catalyst architecture—particularly the use of NiO nanoparticle seeds during synthesis—which favors phase segregation of MoO_{3-x} at the catalyst surface. This not only enhances electron transfer pathways but also promotes stable reaction interfaces. Moreover, the powder catalyst format allows for more efficient packing and mechanical integration within the membrane–electrode assembly (MEA), minimizing ohmic losses and facilitating scale-up[47]. These findings underline the promise of Mo-based oxide systems as efficient and scalable alternatives to precious metal catalysts in next-generation AEM water electrolyzers.

6.4.3. Scale up of electrode preparation and testing

To assess the practical applicability of the $MoO_{3-x}NiMoO_4$ catalyst in an operational electrochemical environment, the material annealed at 600 °C was integrated into a lab-scale anion exchange membrane (AEM) water electrolysis cell. The membrane-electrode assembly (MEA), with a geometrical area of 78.5 cm^2, was fabricated using a catalyst-coated substrate (CCS) method. In this configuration, the cathode comprised the powdered $MoO_{3-x}NiMoO_4$ material supported on Ni foam, with a catalyst loading of 5 mg cm^{-2}. The catalyst ink was prepared by ball-milling the active material with Vulcan XC-72 carbon, followed by dispersion in a suitable solvent and deposition onto the substrate via ultrasonication. Importantly, the catalyst layer was blended with a poly(styrene-ethylene-butylene-styrene) copolymer (PSEBS-CM), which was subsequently functionalized with DABCO to introduce quaternary ammonium groups. This modification imparted anion conductivity to the polymer binder,

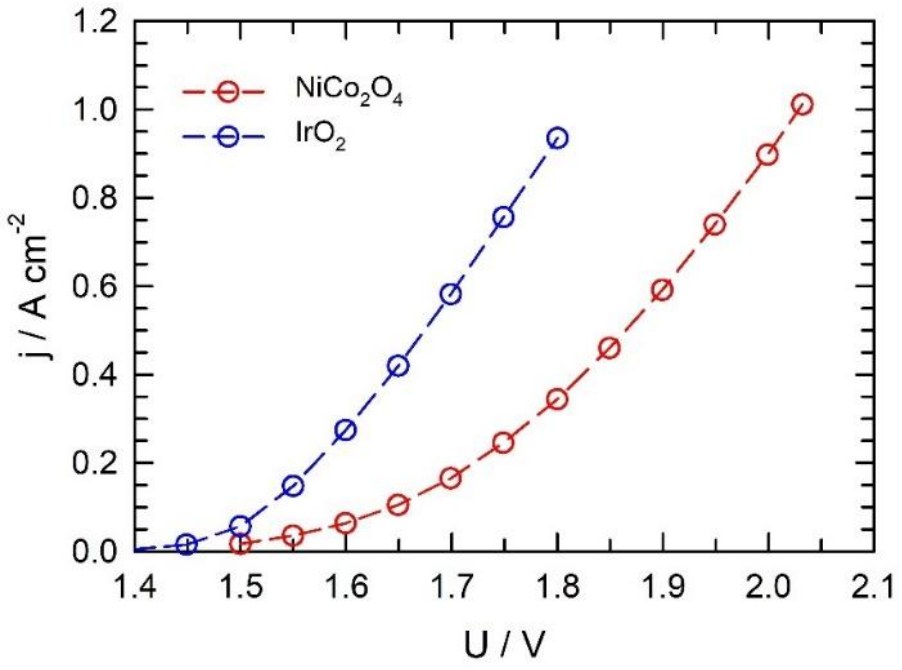

Figure 41: Load curves of the alkaline water electrolysis with MoO3-x NiMoO4 600 °C cathode and anodes using IrO_2 and $NiCo_2O4$ catalyst. Temperature 50°C, 1 mol dm^{-3} KOH, PSEBS-CM-DABCO (60 µm thick) separator 2mg IrO_2 cm^{-2}, 5 mg $NiCo_2O_4$ cm^{-2}, geometrical aerea 78.5 cm^{-2}

allowing it to simultaneously function as both ionomer and structural support. The assembled MEA utilized a 60 μm-thick. The assembled MEA utilized a 60 μm-thick PSEBS-CM-DABCO membrane as the solid-state electrolyte. Two distinct anode configurations were evaluated for comparative analysis: one employing a platinum group metal (PGM) catalyst, IrO_2 (2 mg cm^{-2}), and another based on a non-PGM $NiCo_2O_4$ spinel oxide (5 mg cm^{-2}), both deposited on nickel foam. The electrochemical testing was conducted at 50 °C with 1 M KOH aqueous solution circulated in both the anode and cathode compartments. As illustrated in Figure 41, the polarization curve for the complete cell using IrO_2 as the anodic catalyst revealed a current density of 0.9 A cm^{-2} at a cell voltage of 1.8 V. In comparison, the cell employing $NiCo_2O_4$ reached the same current density only at 2.0 V, clearly demonstrating the performance gap between noble-metal and transition-metal-based OER catalysts under identical operating conditions.

These results were contextualized by comparison with previous work using MoO_2 grown directly on nickel foam as the cathode catalyst. In that earlier configuration, the cell achieved only 0.23 A cm^{-2} at 1.8 V and sustained 0.2 A cm^{-2} at 1.95 V over 60 hours of continuous operation. The improved performance observed with the powder-based $MoO_{3-x}NiMoO_4$ catalyst is likely due to two primary factors: first, a significant enhancement in the intrinsic catalytic activity, and second, improved interfacial contact between the catalyst layer and the polymer membrane. This more intimate contact reduces both charge transfer and ohmic losses, which are critical limitations in membrane-based electrolysis cells, especially when using powder catalysts.

Further insight into the resistive contributions within the cells was obtained by electrochemical impedance spectroscopy (EIS). Measurements were performed across a frequency range of 100 kHz to 10 Hz using a perturbation amplitude of 10 mV. Figure 10 reports the values of ohmic resistance (Rs) and polarization resistance (Rp) extracted from the spectra. The cell employing the IrO_2 anode exhibited a slightly lower Rs (approximately 7% less) compared to the $NiCo_2O_4$-based counterpart (Figure 42-a). This difference is attributable to the higher intrinsic electrical conductivity of IrO_2, which facilitates electron transport

through the catalyst layer. However, a more pronounced disparity was observed in the Rp values. The $NiCo_2O_4$-containing cell displayed a single high Rp semicircle, suggesting that the slow oxygen evolution reaction (OER) kinetics dominate the overall polarization losses. In contrast, the IrO_2 cell revealed two distinct semicircles, which were assigned to the OER and possibly also to HER or interfacial processes at the cathode side, now discernible due to the reduced anodic polarization.

Specifically, the Rp (Figure 42-b) value for the $NiCo_2O_4$ anode was approximately 1.51 Ω cm², a reflection of the sluggish four-electron transfer mechanism involved in the OER on non-PGM materials. Conversely, for the IrO_2-based anode, Rp values were significantly lower, 0.13 and 0.04 Ω cm² respectively, confirming that OER kinetics no longer constitute the performance-limiting step in that configuration. These findings underline the critical importance of developing more active non-PGM OER catalysts to fully unlock the potential of non-noble metal-based cathodes such as $MoO_{3-x}NiMoO_4$. The cathodic performance is clearly enhanced by the high conductivity and phase composition of the catalyst, but this advantage can only be fully exploited when paired with a comparably efficient anode.

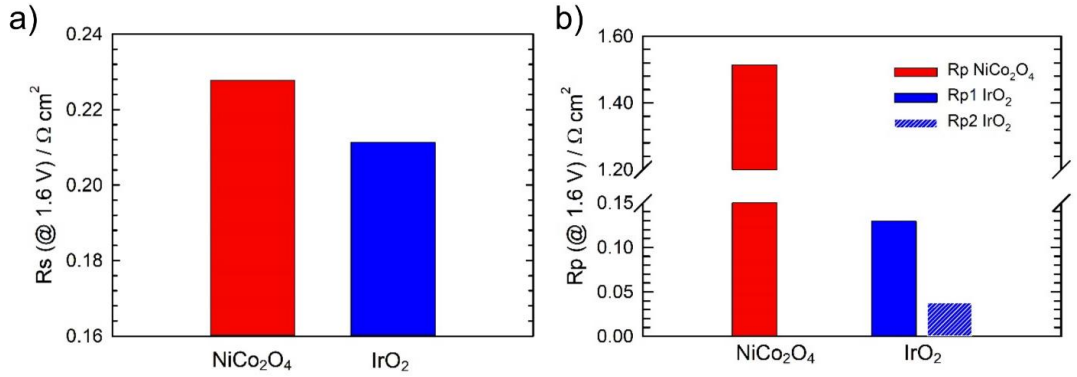

Figure 42: Results of ohmic resistance (a) (Rs) and (b) polarisation resistances (Rp) evaluated from EIS spectra. Temperature 50 °C, 1 mol dm^{-3} KOH, PSEBS-CM-DABCO (60 µm thick) separator, 2 mg IrO_2 cm^{-2}, 5 mg $NiCo_2O_4$ cm^{-2} $MoO_{3-x}NiMoO_4$ 600 °C cathode, geometrical are 78.5 cm^2. EIS measured in the frequency range 100 kHz–10Hz, with maximal amplitude 10 mV.

In summary, the $MoO_{3-x}NiMoO_4$ powder catalyst synthesized at 600 °C demonstrates excellent potential as a cathode material in AEM electrolysis. Its

integration in a large area MEA delivers high current densities with improved stability and efficiency. The comparative analysis between noble and non-noble metal anodes further confirms the importance of synergistic electrode design. Optimizing both electrodes and their interfacial properties with the membrane is essential to minimize losses and ensure durable, high-performing AEM electrolyzer systems.

6.5 Conclusions

This doctoral work has focused on the design, synthesis, characterization, and application of non-noble metal catalysts for hydrogen production via alkaline anion exchange membrane (AEM) electrolysis. Through a comprehensive and multidisciplinary approach, a new catalytic system based on MoO_{3-x}/$NiMoO_4$ composite powders has been developed, offering a promising alternative to conventional electrode fabrication methods based on metallic supports.

The synthetic strategy presented here leverages the use of commercially available NiO nanopowder as a structural and chemical template to direct the formation of a fully particulate catalyst material. Unlike traditional methods that rely on the direct growth of catalytic phases on conductive substrates (e.g., Ni foam), this approach results in a self-supported powder catalyst entirely composed of the active phase, significantly simplifying electrode processing. Such configuration enhances the physical contact between the catalyst and the membrane when used in MEAs, while also allowing better accessibility to active sites and improved catalyst utilization.

Advanced surface and structural characterizations, including X-ray photoelectron spectroscopy (XPS), high-resolution transmission electron microscopy (HR-TEM/STEM), and in-situ Raman spectroscopy, have provided detailed insights into the evolution of the catalyst during thermal treatment. It has been shown that annealing under reductive conditions at 600 °C leads to a surface restructuring that favors the formation of MoO_{3-x}-rich phases with increased surface roughness and a heterogeneous morphology characterized by small particles aggregated onto rod-like backbones. In-situ Raman analysis further confirmed the partial decomposition of $NiMoO_4$ and the progressive

emergence of sub-stoichiometric Mo oxides under hydrogen, correlating the structural evolution with catalytic function.

Electrochemical evaluation in three-electrode half-cell setups revealed that the catalyst annealed at 600 °C displayed significantly higher specific and mass activities for the hydrogen evolution reaction (HER) compared to the material treated at 500 °C. Impedance spectroscopy measurements corroborated these findings, highlighting lower charge transfer resistances and suggesting improved kinetics due to the enhanced interface properties and possible synergistic effects at the Ni/NiO–MoO_{3-x} junction. These effects are particularly beneficial in promoting HER mechanisms under alkaline conditions, including both Volmer–Heyrovsky and Volmer–Tafel pathways.

To demonstrate the practical feasibility of the synthesized material, a 5 cm^2 AEM water electrolyzer cell was assembled using the MoO_{3-x}/$NiMoO_4$ catalyst as cathode. The cell exhibited stable operation over 50 hours at 1 A cm^{-2}, with an energy consumption of 57.65 kWh per kg of H_2 produced. This result not only indicates high stability of the catalyst under working conditions but also confirms the compatibility of the powder-based approach with standard MEA fabrication techniques.

Further efforts were directed towards scaling up the technology. A large-area 78.5 cm^2 AEM electrolyzer cell was constructed to evaluate the performance of the catalyst in conditions closer to industrial relevance. When coupled with a PGM IrO_2 anode, the cell achieved 0.9 A cm^{-2} at 1.8 V, while the use of a non-PGM $NiCo_2O_4$ anode led to 1.0 A cm^{-2} at 2.0 V, demonstrating competitive performance even in a fully PGM-free configuration. The results emphasize the critical role of the anode in determining the overall polarization losses of the cell, especially under high current densities. Electrochemical impedance spectroscopy revealed significantly higher OER polarization resistances in the $NiCo_2O_4$-based cells, confirming that the anodic process remains the limiting factor in non-noble configurations and that further development is required to balance the performance of both electrodes.

In conclusion, this thesis demonstrates a scalable and effective synthetic pathway for preparing a non-PGM, powder-based MoO_{3-x}/$NiMoO_4$ catalyst that

can be successfully implemented in AEM electrolysis. The material exhibits high activity and good stability, and its particulate nature facilitates its integration into MEAs and up-scaled electrochemical systems. These findings not only contribute to the understanding of structure–activity relationships in mixed metal oxide systems but also provide a practical framework for transitioning from lab-scale catalyst development to device-level application. The modularity of the synthesis and the flexibility in electrode design offer a solid foundation for future work in the field of sustainable hydrogen production and the broader development of cost-effective, PGM-free electrochemical energy technologies.

6.6 References

1. Staffell, Iain, et al. "The role of hydrogen and fuel cells in the global energy system." *Energy & Environmental Science* 12.2 (2019): 463-491.

2. Eikeng, Erik, Ashkan Makhsoos, and Bruno G. Pollet. "Critical and strategic raw materials for electrolysers, fuel cells, metal hydrides and hydrogen separation technologies." *International Journal of Hydrogen Energy* 71 (2024): 433-464.

3. Miller, Hamish Andrew, et al. "Green hydrogen from anion exchange membrane water electrolysis: a review of recent developments in critical materials and operating conditions." *Sustainable Energy & Fuels* 4.5 (2020): 2114-2133.

4. Green hydrogen from anion exchange membrane water electrolysis
   H.A Miller

5. Yang, Yao, et al. "Electrocatalysis in alkaline media and alkaline membrane-based energy technologies." *Chemical reviews* 122.6 (2022): 6117-6321.

6. Du, Naiying, et al. "Anion-exchange membrane water electrolyzers." *Chemical reviews* 122.13 (2022): 11830-11895.

7. Schropp, Elke, et al. "Environmental and material criticality assessment of hydrogen production via anion exchange membrane electrolysis." *Applied Energy* 356 (2024): 122247.

8. Q.H. Li, A.M. Villarino, C.R. Peltier, A.J. Macbeth, Y. Yang, M.J. Kim, *et al.*

9. Anion exchange membrane water electrolysis: the future of green hydrogen
10. Chen, Nanjun, et al. "High-performance anion exchange membrane water electrolyzers with a current density of 7.68 A cm− 2 and a durability of 1000 hours." *Energy & environmental science* 14.12 (2021): 6338-6348.

11. Park, Sun Hwa, Dung T. To, and Nosang V. Myung. "A review of nickel-molybdenum based hydrogen evolution electrocatalysts from theory to experiment." *Applied Catalysis A: General* 651 (2023): 119013.

12. Wang, Miao, et al. "Alloying nickel with molybdenum significantly accelerates alkaline hydrogen electrocatalysis." *Angewandte Chemie* 133.11 (2021): 5835-5841.

13. Luo, Min, et al. "Insights into alloy/oxide or hydroxide interfaces in Ni–Mo-based electrocatalysts for hydrogen evolution under alkaline conditions." *Chemical Science* 14.13 (2023): 3400-3414.

14. Sadeghi, Ebrahim, et al. "In Situ Design of a Nanostructured Interface between NiMo and CuO Derived from Metal–Organic Framework for Enhanced Hydrogen Evolution in Alkaline Solutions." *ACS Applied Materials & Interfaces* 16.8 (2024): 10078-10092.

15. Bazan-Aguilar, Antony, et al. "Highly active NiMo foam-based electrocatalysts for the hydrogen evolution reaction in alkaline media." *Electrochimica Acta* 479 (2024): 143881.
16. Zhang, Si-xuan, and Jin-zhao Huang. "Recent progress in NiMo-based amorphous alloys for electrocatalytic hydrogen evolution reaction." *Transactions of Nonferrous Metals Society of China* 34.1 (2024): 26-49.

17. Schalenbach, Maximilian, et al. "Nickel-molybdenum alloy catalysts for the hydrogen evolution reaction: Activity and stability revised." *Electrochimica Acta* 259 (2018): 1154-1161.

18. Zhang, Jian, et al. "Efficient hydrogen production on MoNi4 electrocatalysts with fast water dissociation kinetics." *Nature communications* 8.1 (2017): 15437.

19. Chen, Yu-Yun, et al. "Self-templated fabrication of MoNi4/MoO3-x nanorod arrays with dual active components for highly efficient hydrogen evolution." *Advanced Materials* 29.39 (2017): 1703311.

20. Bartoli, Francesco, et al. "Probing the activity and stability of MoO 2 surface nanorod arrays for hydrogen evolution in an anion exchange membrane multi-cell water electrolysis stack." *Journal of Materials Chemistry A* 11.11 (2023): 5789-5800.

21. Scanlon, David O., et al. "Theoretical and experimental study of the electronic structures of MoO3 and MoO2." *The Journal of Physical Chemistry C* 114.10 (2010): 4636-4645.

22. McCrory, Charles CL, et al. "Benchmarking hydrogen evolving reaction and oxygen evolving reaction electrocatalysts for solar water splitting devices." *Journal of the American Chemical Society* 137.13 (2015): 4347-4357.

23. Hnát, Jaromír, et al. "Anion-selective materials with 1, 4-diazabicyclo [2.2. 2] octane functional groups for advanced alkaline water electrolysis." *Electrochimica Acta* 248 (2017): 547-555.

24. Aloui, T., et al. "Synthesis and characterization of nanosheet NiMoO4

powder as a highly efficient and reusable catalyst for environmental remediation." *Journal of Nanoparticle Research* 24.2 (2022): 35.

25. Basharat, F., et al. "Heat treatment of electrodeposited NiO films for improved catalytic water oxidation." *RSC Advances* 5.105 (2015): 86713-86722.

26. Chen, Yuping, et al. "Single-crystalline orthorhombic molybdenum oxide nanobelts: synthesis and photocatalytic properties." *CrystEngComm* 12.11 (2010): 3740-3747.

27. de Moura, Ana P., et al. "Structural, optical, and magnetic properties of NiMoO4 nanorods prepared by microwave sintering." *The Scientific World Journal* 2015.1 (2015): 315084.

28. Wen, Yuanbin, et al. "Roles of oxygen vacancies in NiMoO4: a first-principles study." *Frontiers in Energy Research* 9 (2021): 793032.

29. Baltrusaitis, Jonas, et al. "Generalized molybdenum oxide surface chemical state XPS determination via informed amorphous sample model." *Applied Surface Science* 326 (2015): 151-161.

30. Rodriguez, José A., et al. "Phase transformations and electronic properties in mixed-metal oxides: Experimental and theoretical studies on the behavior of NiMoO 4 and MgMoO 4." *The Journal of Chemical Physics* 112.2 (2000): 935-945.

31. Saleem, S. Sheik. "Infrared and Raman spectroscopic studies of the polymorphic forms of nickel, cobalt and ferric molybdates." *Infrared physics* 27.5 (1987): 309-315.

32. da Silva, Maíra V., et al. "Influence of temperature on the structural and

color properties of nickel molybdates." *Materials Research Bulletin* 122 (2020): 110665.

33. Popovych, Olha M., et al. "Raman spectroscopy of nickel molybdate and its modifications." *Fullerenes, Nanotubes and Carbon Nanostructures* 29.12 (2021): 1009-1015.

34. Xiao, Wei, et al. "Synthesis, characterization, and lithium storage capability of AMoO4 (A= Ni, Co) nanorods." *Chemistry of Materials* 22.3 (2010): 746-754.
35. Bankar, Prashant K., et al. "Enhanced field emission performance of NiMoO4 nanosheets by tuning the phase." *Applied Surface Science* 418 (2017): 270-274.

36. Sediva, Eva, et al. "In situ method correlating Raman vibrational characteristics to chemical expansion via oxygen nonstoichiometry of perovskite thin films." *Advanced Materials* 31.33 (2019): 1902493.

37. Rodriguez, José A., et al. "Reduction of CoMoO4 and NiMoO4: in situ time-resolved XRD studies." *Catalysis letters* 82.1 (2002): 103-109.

38. Abdel-Dayem, Hany M. "Dynamic phenomena during reduction of α-NiMoO4 in different atmospheres: in-situ thermo-Raman spectroscopy study." *Industrial & engineering chemistry research* 46.8 (2007): 2466-2472.

39. Camacho-López, M. A., et al. "Micro-Raman study of the m-MoO2 to α-MoO3 transformation induced by cw-laser irradiation." *Optical Materials* 33.3 (2011): 480-484.

40. Hawkins, Donald T., and Wayne L. Worrell. "Hydrogen reduction of MoO3 at temperatures between 300° and 450° C." *Metallurgical*

Transactions 1.1 (1970): 271-273.

41. Lalik, Erwin, et al. "Mechanisms of reduction of MoO3 to MoO2 reconciled?." *The Journal of Physical Chemistry B* 105.38 (2001): 9153-9156.

42. Dang, Jie, Guo-Hua Zhang, and Kuo-Chih Chou. "Phase transitions and morphology evolutions during hydrogen reduction of MoO3 to MoO2." *High Temperature Materials and Processes* 33.4 (2014): 305-312.

43. Gong, Ming, et al. "Nanoscale nickel oxide/nickel heterostructures for active hydrogen evolution electrocatalysis." *Nature communications* 5.1 (2014): 4695.

44. Hitz, C., and A. Lasia. "Experimental study and modeling of impedance on porous Ni electrodes." *Journal of Electroanalytical Chemistry* 500.1-2 (2001): 213-222.

45. Alemu, Hailemichael, and K. Jüttner. "Characterization of the electrocatalytic properties of amorphous metals for oxygen and hydrogen evolution by impedance measurements." *Electrochimica acta* 33.8 (1988): 1101-1109.

46. Shahgaldi, Samaneh, Ibrahim Alaefour, and Xianguo Li. "Impact of manufacturing processes on proton exchange membrane fuel cell performance." *Applied Energy* 225 (2018): 1022-1032.

47. Hwang, Doo Sung, et al. "Optimal catalyst layer structure of polymer electrolyte membrane fuel cell." *International journal of hydrogen energy* 36.16 (2011): 9876-9885.

7. Experimental Section

7.1 Electron Microscopy

Transmission electron microscopy (TEM) was used to investigate the morphology of the catalysts. TEM images allowed evaluation of particle size, distribution, and agglomeration. High-resolution TEM (HR-TEM) provided atomic-level information on small particles, while scanning transmission electron microscopy (STEM), coupled with energy-dispersive X-ray spectroscopy (EDX), was employed to determine elemental distribution in the nanoparticles.

7.1.1. Transmission Electron Microscopy

For TEM analysis, 1–2 mg of catalyst powder was dispersed in 1 mL of ethanol and sonicated for 10–15 minutes to form a homogeneous suspension. A drop of the suspension was deposited on a carbon-coated copper grid and left to dry under ambient conditions. TEM images were acquired using a Philips CM12 microscope operating at 100 kV and equipped with an EDAX EDX system to allow elemental analysis when necessary.

7.1.2. High-Resolution TEM and Scanning TEM

HR-TEM and STEM were performed on a Talos F200X G2 microscope (Thermo Scientific). Catalyst powders were prepared similarly to TEM samples, ensuring minimal particle aggregation. The SuperX four-detector EDX system allowed high-resolution elemental mapping and verification of alloy formation. Lattice fringes were analyzed to confirm interplanar spacing and crystal structure.

7.2 X-ray Powder Diffraction

For XRPD, 10–20 mg of catalyst was finely ground and evenly deposited on zero-background silicon holders. Measurements were carried out at room temperature using a PANalytical X'Pert PRO diffractometer with Cu Kα radiation (λ = 1.54187 Å) and a parabolic MPD mirror for beam focusing. Diffraction patterns were recorded over a 2θ range of 5–120° in continuous scan mode, with a step size of 0.0263° and 49.5 s counting time per step. Data were analyzed to determine crystallinity, phase composition, and crystallite size.

7.3 Half Cell Experiment

Electrochemical measurements were conducted using a Pine Instruments setup in a standard three-electrode configuration. A reversible hydrogen electrode (RHE) served as the reference, and a gold wire as the counter electrode. Both rotating disk electrode (RDE) and rotating ring-disk electrode (RRDE) techniques were used, with glassy carbon disks of 0.194 cm^2 (RDE) and 0.346 cm^2 (RRDE), the latter coupled with a platinum ring of 0.196 cm^2. Electrolytes were prepared with ultrapure water (≥18.2 MΩ·cm) and analytical-grade salts, degassed with N_2 for 60 minutes before each experiment. All data were corrected for ohmic drop (iR compensation).

7.3.1. Catalyst Ink Preparation and Electrode Coating

Catalyst inks were prepared by dispersing 5 mg of catalyst in 1 mL of water/isopropanol (1:1 v/v) with 50 µL of 5 wt% Nafion solution. The mixture was sonicated for 15 minutes to ensure homogeneity. A defined volume of ink was drop-cast onto the glassy carbon electrodes and left to dry at room temperature. This procedure was applied for both RDE and RRDE experiments.

7.3.2. Cyclic Voltammetries

Cyclic voltammetry (CV) was performed in 1 M KOH to study HOR, HER, and ORR catalysts, and in 2 M KOH + 1 M potassium formate for FAOR. Scans were performed at 50 mV/s within the relevant potential window to evaluate activity, stability, and CO tolerance. Electrodes were preconditioned with 20 CV cycles before measurements.

7.3.3. CO-Stripping

CO stripping voltammetry was used to evaluate catalyst tolerance to CO poisoning. Electrodes were exposed to CO at 0.1 V vs RHE for a few minutes, followed by N_2 purging to remove excess CO. Voltammograms were recorded at 50 mV/s to detect the oxidation peak of adsorbed CO, providing information on EASA and surface cleanliness.

7.3.4. Polarization Experiments

Polarization curves were recorded in 1 M KOH under H_2 or O_2 saturation for HOR, HER, and ORR catalysts, respectively, using RDE at 1600 rpm and a scan rate of 1 mV/s. Potential ranges covered the hydrogen adsorption/desorption and oxygen reduction/oxidation regions. Tafel plots were derived from the linear portions to evaluate reaction kinetics.

7.4 Complete Fuel Cell

Fuel cell testing was performed using a Scribner 850 Fuel Cell Test System, allowing precise control of voltage, current, temperature, and gas flows, with real-time data acquisition for performance and durability analysis.

7.4.1. Monoplanar Active Fuel Cell

The monoplanar fuel cell consisted of conductive support plates, gas diffusion

layers (GDLs), catalyst-coated electrodes, and a polymer electrolyte membrane (PEM). Platinum on carbon catalyzed HOR at the anode and ORR at the cathode. The PEM enabled selective proton transport, preventing electron and gas crossover. This layered structure ensured efficient electrochemical conversion and reproducible testing conditions.

7.4.2. Alkaline H_2/O_2 and Formate-Fed Fuel Cells

Anodes were prepared by coating nickel foam with catalyst ink (catalyst + PTFE binder) and drying at 60 °C. Membrane electrode assemblies (MEAs) were formed by pressing the anode, membrane, and cathode together. H_2 and O_2 were humidified to 80% RH and supplied at 0.1–0.2 L/min. Formate-fed cells received 1 M potassium formate + 1 M KOH via peristaltic pumps. Cells were activated at 500 mA for 1 h before measurements.

7.5 Electrolysis Complete Cell

Electrocatalyst performance was evaluated using an Arbin BT 2000-54 potentiostat/galvanostat. Polarization and chronopotentiometric tests were performed to assess activity and stability.

7.5.1. Electrolyzer

The NiMo/C anode was prepared by mixing 100 mg catalyst with a few drops of distilled water and 50 mg of 10 wt% PTFE dispersion to form a dense paste, which was uniformly applied onto a 4 cm² nickel foam (110 PPI) and air-dried. The Pt/C cathode was prepared by mixing 200 mg Pt/C (40 wt%) with 450 mg distilled water, 790 mg 1-propanol, and 1.56 g Nafion (5 wt% in 2-propanol), sonicated in a 5 mL HDPE vial (3 pulses, 20 W, 20 kHz), and coated onto carbon cloth using a Meyer rod (150 µm) to achieve 0.4 mg Pt/cm². Coated electrodes were air-dried and stored under inert conditions until use.

8. Conclusions

This doctoral research has demonstrated the design, synthesis, and implementation of advanced electrocatalysts for sustainable energy conversion, highlighting the interplay between structural features, composition, and electrochemical performance.

A novel $MoO_{3-x}/NiMoO_4$ powder catalyst was successfully developed as a self-supported, non-PGM material for alkaline hydrogen production. Thermal treatment under reductive conditions generated a heterogeneous, sub-stoichiometric Mo oxide surface with increased active site accessibility. The catalyst showed excellent HER activity, both in three-electrode configurations and in scaled AEM electrolyzer cells, confirming the feasibility of powder-based electrodes for practical hydrogen generation.

Hybrid silver-supported metal phthalocyanines (M-Pc@Ag/C) exhibited strong synergistic interactions between conductive Ag nanoparticles and active metal centers, resulting in high ORR activity and selectivity. Among the tested systems, FePc@Ag/C emerged as the most effective, demonstrating the potential of combining metallic and organic components to create cost-effective alternatives to platinum catalysts.

PdAu/C bimetallic nanoparticles synthesized via Matrix Isolation Synthesis revealed how nanoscale alloying can modulate electronic and structural properties, enhancing both catalytic activity and stability in direct formate fuel cells. Similarly, Pd@NiW/C catalysts displayed exceptional mass activity for HER and HOR, with reduced charge-transfer resistance and favorable kinetics, confirming the advantage of synergistic interactions between Pd and NiW supports.

Overall, this thesis establishes scalable and versatile synthetic strategies for producing high-performance electrocatalysts, elucidates critical structure–activity–stability relationships, and demonstrates successful translation from lab-scale materials to device-level applications. These findings provide a foundation for the continued development of sustainable, PGM-free, and cost-

effective energy conversion technologies, advancing the field toward practical implementation of hydrogen-based and electrocatalytic energy systems